RADIOSCIENCE LABORATORY

STANFORD ELECTRONICS LABORATORIES
DEPARTMENT OF ELECTRICAL ENGINEERING
STANFORD UNIVERSITY · STANFORD, CA 94305

THE COMBINED EFFECTS OF REFRACTION AND COHERENT SCATTERING BY COLUMNAR IONIZATION DENSITY IRREGULARITIES IN IONOSPHERIC RADIO PROPAGATION

By

David Michael Bubenik

March 1976

THE COMBINED EFFECTS OF REFRACTION AND COHERENT SCATTERING BY COLUMNAR IONIZATION DENSITY IRREGULARITIES IN IONOSPHERIC RADIO PROPAGATION

A DISSERTATION
SUBMITTED TO THE DEPARTMENT OF ELECTRICAL ENGINEERING
AND THE COMMITTEE ON GRADUATE STUDIES
OF STANFORD UNIVERSITY
IN PARTIAL FULFILLMENT OF THE REQUIREMENTS
FOR THE DEGREE OF
DOCTOR OF PHILOSOPHY

By
David Michael Bubenik

March 1976

UNCLASSIFIED

SECURITY CLASSIFICATION OF THIS PAGE (When Data Entered)

REPORT DOCUMENTATION PAGE

READ INSTRUCTIONS BEFORE COMPLETING FORM

1. REPORT NUMBER	2. GOVT ACCESSION NO.
3. RECIPIENT'S CATALOG NUMBER	
4. TITLE (and Subtitle) THE COMBINED EFFECTS OF REFRACTION AND COHERENT SCATTERING BY COLUMNAR IONIZATION DENSITY IRREGULARITIES IN IONOSPHERIC RADIO PROPAGATION	5. TYPE OF REPORT & PERIOD COVERED Ph.D. Dissertation September 1971 to December 1973
	6. PERFORMING ORG. REPORT NUMBER N/A
7. AUTHOR(s) David M. Bubenik	8. CONTRACT OR GRANT NUMBER(s) N00014-67-A-0112-0066
9. PERFORMING ORGANIZATION NAME AND ADDRESS Stanford Electronics Laboratories Stanford University Stanford, California 94305	10. PROGRAM ELEMENT, PROJECT, TASK AREA & WORK UNIT NUMBERS ARPA Order No. 1733
11. CONTROLLING OFFICE NAME AND ADDRESS Office of Naval Research (Code 465(K)) 800 North Quincy Street Arlington, Virginia 22217	12. REPORT DATE March 1976 / 13. NO. OF PAGES 170
	15. SECURITY CLASS. (of this report) UNCLASSIFIED
14. MONITORING AGENCY NAME & ADDRESS (if diff. from Controlling Office)	15a. DECLASSIFICATION/DOWNGRADING SCHEDULE N/A

16. DISTRIBUTION STATEMENT (of this raport)

Approved for public release; distribution unlimited.

17. DISTRIBUTION STATEMENT (of the abstract entered in Block 20, if differant from report)

18. SUPPLEMENTARY NOTES

19. KEY WORDS (Continue on reverse side if necessery and identify by block number)

Bistatic HF radar
Columnar electron density irregularities
Columnar scatterers
Computer raytracing
Ducted ionospheric propagation
HF/VHF radio wave propagation
Ionospheric modification
Ionospheric propagation
Long-distance radio propagation
Ray theory
Spread-F ionospheric disturbances

20. ABSTRACT (Continue on reverse side if necessary and identify by block number)

The disposition of HF and VHF signals scattered by columnar ionization density irregularities (e.g., meteor trails, geomagnetic field-aligned irregularities) embedded in a refracting ionospheric propagation medium is examined, using ray theory, from two viewpoints: 1) in very long distance propagation, as a means to couple a transmitted signal into the relatively low-loss ground-detached ("whispering gallery," ionosphere-ionosphere, chordal-hop) radio wave propagation mode, and 2) in the bistatic radar sounding of field-aligned irregularities.

DD FORM 1 JAN 73 1473

EDITION OF 1 NOV 65 IS OBSOLETE

UNCLASSIFIED

SECURITY CLASSIFICATION OF THIS PAGE (When Data Entered)

19. KEY WORDS (Continued)

20 ABSTRACT (Continued)

Considering first the mode-coupling aspect, it was indicated how to characterize the elevated ionospheric ducts guiding the ground-detached mode. A series of graphical overlays was then constructed to locate these ducts in $f_N(h)$ profiles. Other graphical displays were developed to determine when mode coupling into these ducts would occur from columnar reflectors. The efficiency of the coupling process was also examined. Efficiencies exceeding 50% of the scattered energy appear to be practical.

In the radar sounding phase, it was established analytically that bistatic radar echoes from reflecting columns would occur at a predictable, invariant aspect angle whenever the outgoing and returning signals travel paths of equal length through identical propagation media. This analysis was confirmed by a raytracing simulation of SFCW backscatter echoes received in central California from the Platteville, Colorado ionospheric modification program. Finally, a detailed analysis of the SFCW echo signature is presented.

I certify that I have read this thesis and that in my opinion it is fully adequate, in scope and quality, as a dissertation for the degree of Doctor of Philosophy.

Oswald G. Villard, Jr.
(Principal Adviser)

I certify that I have read this thesis and that in my opinion it is fully adequate, in scope and quality, as a dissertation for the degree of Doctor of Philosophy.

I certify that I have read this thesis and that in my opinion it is fully adequate, in scope and quality, as a dissertation for the degree of Doctor of Philosophy.

Thomas A Croft

Approved for the University Committee on Graduate Studies:

W B Cannon
Dean of Graduate Studies

ACKNOWLEDGMENTS

I wish to acknowledge my indebtedness and express my gratitude -

to O. G. Villard, Jr., principal advisor, who suggested the topic and provided indispensable advice and support throughout this work;

to A. C. Fraser-Smith, associate advisor, for his advice, support, and assistance;

to the technical staff of the Ionospheric Dynamics Laboratory of the Stanford Research Institute, for their assistance in obtaining the experimental data;

to various members of the staff of the Radioscience Laboratory, Stanford University, for many helpful discussions;

to Dolores Bennett for her expert typing;

and to Patricia Bubenik, my wife, for her special kind of support and encouragement.

CONTENTS

CONTENTS (cont'd)

CONTENTS (cont'd)

TABLES

ILLUSTRATIONS

APPENDIX ILLUSTRATIONS

1. INTRODUCTION

1.1 Purpose and Objectives

The purpose of this report is to present the results of a ray theory investigation into the disposition of radio signals in the frequency range 10-50 MHz which have been reflected from columnar electron density irregularities embedded in the refracting ionospheric propagation medium. Examples of such irregularities are meteor trails and the geomagnetic-field-aligned columnar structures associated with the radio aurora and certain spread-F type ionospheric disturbances. These reflectors act to scatter the radio signal energy from an incident ray into a cone coaxial with the column axis and of apex half-angle equal to the angle of ray incidence upon the column. The scope of this investigation was limited to the 10-50 MHz frequency band for two reasons: a) the propagation paths of radio waves in this range are significantly influenced by ionospheric refraction, but b) the influences of magnetoionic and collisional effects upon these paths are largely negligible, permitting a considerable simplification of the mathematical and conceptual developments.

In order to provide maximum internal continuity within each topic discussed in this report, introductory material which would otherwise have been collected into a large overall introductory chapter has instead been presented in the detailed introductory and literature review sections of each chapter. Therefore only a brief outline of the objectives of this investigation will be given in the following paragraphs.

The first objective was to study the ability of columnar scatterers to couple radio signals into the ground-detached propagation mode*, also known in the literature as the whispering-gallery, guided, chordal-hop, or tilt mode. As compared to the more common propagation mechanism in which the radio waves are reflected successively from the ionosphere and the ground (the so-called ground-hop mode), the ground-detached mode

---

* The term "mode" is used throughout this report to denote the characteristic form of the propagation path of a given radio signal. It should not be confused with the same term as used in the theory of waveguides, oscillatory systems, etc.

has been shown by others to offer a superior long-distance propagation channel, both because it avoids the absorption and scattering effects associated with ground reflections, and because it may also avoid the ionospheric D region and its absorptive effects. As a result, the strength and integrity of the signal are much better preserved. In addition, the maximum usable frequency over a given ionospheric radio link is greater for the ground-detached mode. However, since a signal propagating via this mode does not touch the ground, it is not directly accessible to ground-based radio terminals, and the signal energy must be coupled into and recovered from the ground-detached mode by some auxiliary means. It is the purpose of the first two chapters of this report to present a generalized study of the coupling properties of column scatterers and, in particular, to determine a) the necessary and sufficient conditions for such coupling to occur, and b) the circumstances under which the optimum mode coupling efficiency* will be achieved.

The first part of Chapter 2 contains a discussion of the role of the ground-detached mode in very-long-range HF/VHF radio wave propagation, based upon a review of the literature. The requisites for ground-detached propagation in a spherically-symmetric ionospheric medium are then developed using ray theory. In Chapter 3 these conditions are coupled with the geometry of the columnar scattering mechanism to study the mode-coupling properties of this process.

The second objective of this investigation was to study the propagation phenomena involved in the radar sounding of geomagnetic-field-aligned column scatterers, and thereby to determine how the effects of the refracting ionospheric propagation medium combine with the geometry of radio wave scattering by columnar irregularities to produce the radar echoes often received from such reflectors. The experimental data upon which this study was based consisted of a series of such echoes in the 9-27 MHz band, recorded in the signal amplitude vs. apparent range vs. radio frequency ionogram format. These echo signatures were obtained

---

* The coupling efficiency is defined for this purpose to be the fraction of the scattered signal energy which is coupled into the ground-detached mode.

using an HF band oblique sounder located in central California to sound an artificially-induced ionospheric disturbance over northern Colorado, which was thought to contain field-aligned reflecting columns. Unlike earlier studies of radar echoes from naturally-occurring field-aligned irregularities, in which both the location of the reflectors and the properties of the signal propagation paths were only roughly known, this experiment provided an opportunity to study the propagation effects under relatively well-defined conditions. The study was carried out by conducting a raytracing simulation of the observed echo signatures, assuming that the echoes were due to scattering by field-aligned columns in the man-made ionospheric irregularity, and using up-to-date computer raytracing techniques in a realistically modeled ionospheric propagation medium. This simulation, presented in Chapter 5, had two principal objectives: a) to determine how the particular reflection and propagation effects combined to produce the observed echo signature, and b) to establish that the artificial disturbance actually did contain field-aligned reflecting columns. An additional consideration in this work was the bistatic configuration of the central California sounder (i.e., the receiver was physically separated from the transmitter). The complications arising from this source are discussed in Chapter 4, where the reflection geometry is analyzed for the case of field-aligned columns being sounded by a bistatic radar. The result of this analysis, that the bistatic echoes from such scatterers will under certain circumstances occur at a predictable incident-ray-to-column-axis angle, is then confirmed by the raytracing simulation of Chapter 5, and then used to facilitate a later phase of that simulation.

1.2 History

The work reported herein evolved from the author's earlier investigations of the round-the-world (RTW) propagation of radio signals. Challenged to explain the extraordinarily great propagation ranges (up to 2×10^5 km) achieved by a 1 kW pulse signal transmitted over a transpolar path [Bubenik, 1971], and the apparent resolution of stable, discrete propagation mode traces on east-west RTW sweep-frequency oblique ionograms [Bubenik et al., 1971], the author was led to consider the

probable role of the ground-detached mode in these very long distance propagation events.

In the course of these studies, several attempts were made in late 1971 and early 1972 to launch an RTW signal into the ground-detached mode using the man-made ionospheric irregularity over Platteville, Colorado as the mode coupling agent for an HF signal transmitted from the oblique ionospheric sounding facility operated in central California by the Stanford Research Institute. It was hoped that the perturbation in the propagation medium presented by the disturbance would alter the propagation mode of the incident signal, deflecting a portion of it into the detached mode which would in turn presumably furnish a favorable RTW propagation channel.

The perturbed region interacted strongly with the radio signal, producing a strong direct backscatter echo. However, the hoped-for RTW signals were not observed. This was attributable, in large part, to the rather poor RTW propagation conditions which existed when the experiment was run. On the other hand, the Platteville modification experiment was itself a novel attempt, and the ionospheric phenomena which it produced were, at the time, largely unexpected and unexplained. In particular, it was not known how to characterize the interaction between the perturbed region and the radio signals, and fundamental questions therefore arose. It had been established that the irregularity was a good reflector; however it was also vital to know whether the radio signal energy was being scattered isotropically or directionally. If the latter, how was the reflected energy distributed in space? In either case, how would the hoped-for coupling into the ground-detached mode occur? It was especially important to determine the azimuthal directions into which the detached mode would be launched, so that the highly-directive receiving antenna could be steered accordingly.

Since an ionization density irregularity in the F region of the ionosphere, where the artificial perturbation was usually situated, will tend to become elongated along the lines of flux of the geomagnetic field, it was a reasonable working assumption that the scattering mechanism consisted, in part at least, of reflection from ionized columns.

Consequently, the author searched the literature for an analysis of the disposition of the radio energy thus reflected into the ionospheric refracting medium. None was found, and the analysis reported in this paper was therefore undertaken. The computer raytracing simulation of the observed backscatter echoes was initiated as a parallel effort to ascertain whether these returns were in fact due to scattering from geomagnetic-field-aligned columns in the Platteville disturbance, and the analysis of field-aligned radar echoes reported in Chapter 5 arose from this simulation.

2. THE GROUND-DETACHED MODE

2.1 The Two Principal Radio Ray Propagation Modes in the Ionosphere

2.1.1 The ground-hop mode

The most common mechanism of trans-horizon radio communication in the HF band (3-30 MHz) between two stations located on the surface of the earth is the ionospherically supported sky-wave mode, which is illustrated in Figure 2.1. There, the solid line TA_1R_1 represents the path of a signal which, after leaving the transmitter T, is refracted downward in the ionosphere so that it reaches an apogee at A_1 and is subsequently returned to earth at the receiver R_1. Useful communication via this single-hop mode is possible for transmitter-receiver separations of less than about 4000 km. For longer signal paths, a radio link may be established via a multi-hop mechanism, in which the signal energy executes several sky-wave hops with intervening more or less specular reflections from the earth. This latter mode is shown in Figure 2.1 by the extension $A_2R_2A_3R_3$ to the basic TA_1R_1 hop. In principle, this sequence may be extended indefinitely, permitting HF radio propagation links to be established between stations separated by very great distances.

However, the usefulness of this mechanism is limited by the large signal power losses incurred when a great number of sky-wave hops are involved. These losses occur via two principal mechanisms. In the first place, the signal energy must traverse the absorbing ionospheric region (stippled band on Figure 2.1) twice during each hop, losing up to several dB in each transit. The other losses occur at each earth reflection where some power is dissipated ohmically in the ground, and an additional fraction may be scattered astray by rough terrain.

These loss mechanisms have been studied intensively since the days of "wireless," and are now well understood [e.g., Davies, 1965; Kelso, 1964]. The magnitudes of the ionospheric and ground absorption losses are strongly dependent upon both the frequency of the radio wave and its elevation angle of propagation. The earth losses generally diminish as the signal trajectory approaches grazing incidence upon the ground. On

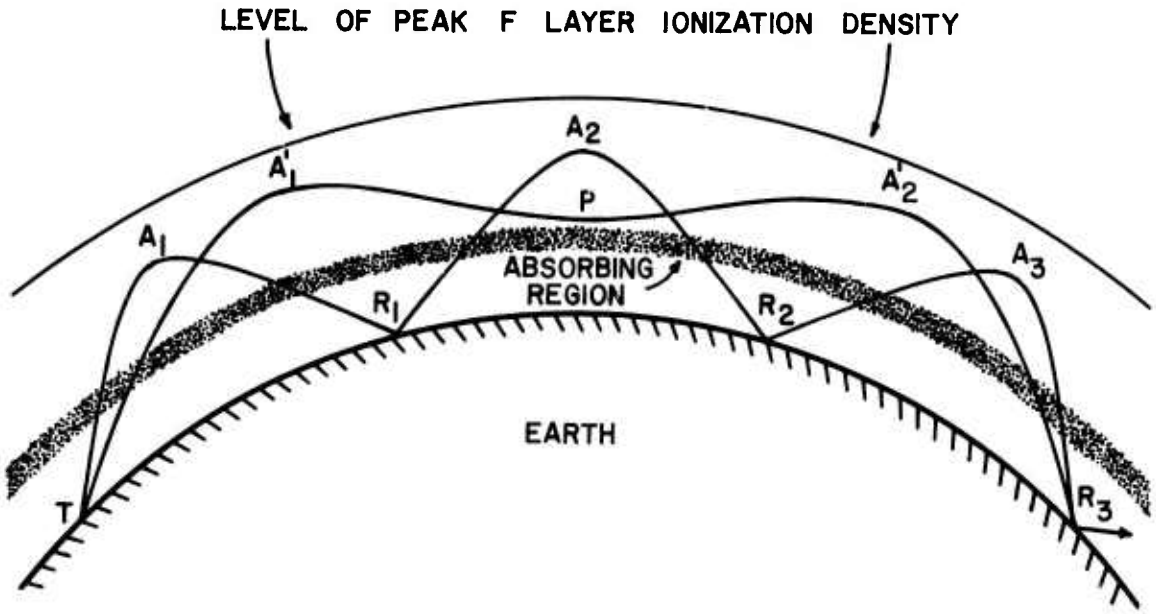

Fig. 2.1 A schematic representation of the principal modes of radio ray propagation in the ionosphere. The path $TA_1R_1A_2R_2A_3R_3$ represents the ground-hop mode; path $TA_1PA_1R_3$ represents the ground detached mode.

the other hand, the dissipation in the lower ionosphere at a given radio frequency becomes more severe under the same circumstances, since a greater portion of the signal path then lies within the absorbing region. Additionally, the ionospheric loss has a diurnal, seasonal, and solar activity dependence, being strongest at the geographical subsolar point in the presence of an active sun, and nearly absent at night. It diminishes rapidly as the radio frequency increases, varying generally as the inverse square of this quantity [Davies, 1965, p. 145]. In its turn, the ground absorption is a function of the nature of the reflecting surface, with greater losses occurring in regions of high resistivity such as the sea. In general, the ground losses initially increase as the frequency rises, leveling off at a plateau value which is determined primarily by the elevation angle of propagation [Davies, 1965, pp. 194-195].

These trends indicate that HF communications over great distances are best conducted using signals of the highest possible frequency, launched toward the transmitter horizon. The value of this maximum

usable frequency (MUF) over a given path is a function of the ionospheric ionization density and its distribution. It is the practice of radio operators to ascertain this frequency and to operate slightly below it. This procedure minimizes the effects of the absorptive loss mechanisms; however, the losses due to scattering from rough terrain along the path are mostly beyond the operator's control.

2.1.2 The ground-detached mode

Ground-contact losses may be reduced by minimizing the number of earth reflections which the signal must undergo. Such losses are absent entirely from the single-hop path TA_1R_1 on Figure 2.1 and likewise from the path $TA_1'A_2'R_3$ which, owing to its highly oblique incidence upon the ionosphere over the segment $A_1'A_2'$, executes a perigee at P instead of undergoing a ground reflection. Although the attenuation of this latter mode in the D region is somewhat greater, due to its more oblique incidence upon that layer, this obliquity increases the path MUF supportable by the F layer and thus, given the inverse-square dependence of this absorption upon frequency, may largely compensate for that initial disadvantage. Moreover, if the perigee altitude is great enough, the D region and its losses may be avoided completely. As before, propagation to great distances via a ground-detached mode such as $A_1'A_2'$ is possible by extending the apogee-perigee sequence.

The ground-detached mode represents the most general form of wave propagation near the inner boundary of the cavity formed by the ionosphere. In the idealized case, where this cavity is spherical with a sharp, perfectly reflecting boundary enclosing a vacuum, the path of a ray traveling about the circumference is a series of chords, as shown in Figure 2.2. If the bow PC of these chords is not too great, a concentric spherical reflector C' (representing the earth) placed inside the cavity will not affect the raypath. If, however, PC exceeds the difference between the radii of the two spheres, the chordal raypath will be intercepted by the inner sphere and reflected from its surface into a new chordal path. Repeating this sequence, the ray is seen to travel via a series of hops between the spheres, in a path essentially like the ground-hop ionospheric propagation mode discussed earlier. It

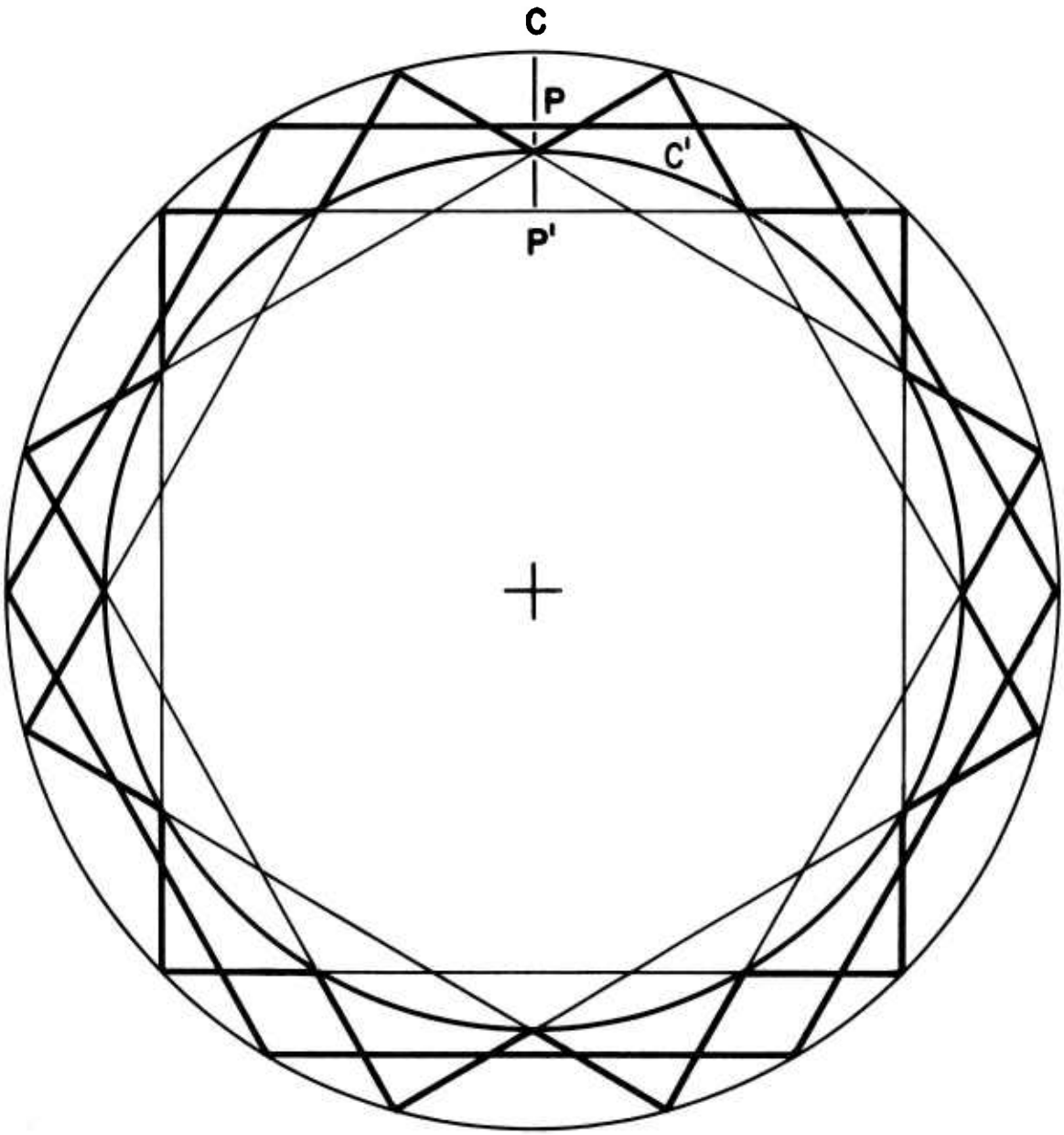

Fig. 2.2 Idealized raypaths in the earth-ionosphere cavity

is thus apparent that the ground-detached mode is the general mode of ionospheric propagation, while the ground-hop mode is a variant case.

The very nature of the ground-detached mode prohibits direct access to it by ground-based radio terminals, and some means of coupling must therefore be provided between the detached mode and a ground-hop path which can reach the earthbound stations. As will be shown later, this coupling is accomplished by appropriately altering the direction of travel of the ray. This may be done by several types of ionospheric irregularities, such as tilts, meteor trails, small regions of enhanced or depleted ionization density, and the irregularities responsible for the radio aurora phenomenon. Such couplers must be present at both ends of any radio link established using this mode, which in turn requires a high degree of cooperation on the part of nature. Consequently, most practical ionospheric radio circuits are thought to involve the ground-hop mode.

2.2 The Ground-Detached Mode in Long-Distance HF/VHF Propagation

2.2.1 Experimental evidence

Nevertheless, because of its expected low-loss, extended-MUF characteristics, the ground-detached mode is believed to play an important role in the propagation of radio signals to very great distances, such as to the antipode of the transmitter or completely around the world. An early effort to explain the round-the-world (RTW) propagation phenomenon, which has been noted since the mid-1920's [Quäck, 1927a,b; Eckersley, 1927], in terms of other than the ground-hop mechanism, was the sliding-wave theory advanced by von Schmidt [1936]. Considering an established seismic wave-guidance mechanism, von Schmidt proposed that an electromagnetic wave might be guided in a leaky channel along the ionosphere-outer space boundary if the refractivity discontinuity there were sufficiently sharp.

In a test of this hypothesis, Hess [1948, 1949, 1952] monitored the direct-path and RTW circulating signals received in Denmark from HF transmitters in Madagascar, Brazil, Japan, and the United States. Although he was able to dismiss the sliding-wave mechanism, he did note the curious fact that the signals received via the long paths and RTW

routes were often less distorted than those arriving via the shorter, direct paths. He observed that "The longer the distance, the sharper the signal seems to be...." This circumstance has also been reported by Humby et al. [1955], Bailey [1958], and Isted [1958].

Measurements of the attenuation of multiply-circulating RTW signals have revealed a parallel incongruity. In an analysis of 18.7 MHz RTW echoes received in England from a transmitter in South Africa, Humby et al. [1955] noted that, while the first RTW transit was attenuated an average 26 dB relative to the direct signal, the successive echoes exhibited mean losses of only 13 dB and 3 dB relative to their predecessors. These measurements agree with those of Hess [1948, 1952], who had reported relative attenuations of 10-15 dB for successive RTW circulations and also with those of Isted [1958], who noted that, although the first RTW transit was "heavily" attenuated, the higher-order circulations had losses of only 5-10 dB.

These observations of the high quality and strength of signals propagated over extreme distances are in sharp conflict with expectations based upon the group-hop model. The existence of the destructive phase interference effects due to multipath propagation and the various losses entailed in this propagation mode have been well established by experiment on shorter paths. Since these effects are cumulative, one would expect a progressive degradation of signals traveling longer distance. Instead, signal quality on the longer, reverse great circle path has sometimes been observed to be superior to that on the shorter, direct route; and the incremental attenuation of successive RTW signals, rather than being uniform as would be expected for signals repeatedly traveling the same ground-hop path, may actually diminish between the higher-order transits.

Other anomalous propagation events have been reported. Albrecht [1960] has noted an instance in which similar apparent losses were exhibited by signals traversing long paths of nearly equal length but differing greatly in ground characteristics. Monitoring transmissions from eastern Australia, he observed that the signals received via the transcontinental path to western Europe were no more attenuated than those arriving in North America over a presumably less lossy transoceanic

route. A similar lack of differential attenuation for satellite signals propagated over long paths overlying water and land was reported by Mullen et al. [1966].

Several investigators have reported strong signals propagating at frequencies greatly exceeding the MUF predicted for the path. Isted [1958] found RTW echoes at 37 MHz although the MUF for ground-hop propagation was not supposed to exceed 20 MHz, and radio propagation at frequencies greater than the MUF along an antipodal path was observed by Gerson [1963] and Banks [1965].

The foregoing observations indicate that radio signals traveling to great distances via the ionosphere may show a signal quality considerably surpassing expectations based upon the assumption of the usual ground-hop propagation mode. Also, such observations have been recorded at times when propagation via the ground-hop mode is theoretically forbidden . An alternative mechanism of radio wave propagation is therefore suggested. Several of the cited authors invoked the ground-detached mode, with ionospheric tilts providing the coupling agent, to explain their results. However, they lacked the specific data to determine whether the required tilts were actually present.

More definite are the conclusions drawn by Villard et al. [1957], Stein [1958], and Yeh and Villard [1960], who monitored ground backscatter echoes originating in the 5000-10,000 km range interval and propagated over transequatorial and transpolar paths. Noting the frequent absence of these echoes at intermediate ranges, plus such anomalies as propagation at frequencies exceeding the conventional MUF and curiously little path disruption during polar ionospheric disturbances, they inferred the presence of an elevated propagation mode launched and recovered by the favorable ionospheric tilts believed to exist in these regions, and they substantiated their case with vertical-incidence ionosonde data showing that the required tilts were present. In particular, Stein derived the expected range-intensity characteristics for such tilt-supported transequatorial echoes, and showed that his predictions agreed with the experimental data.

Applying this concept of tilt-coupled ground-detached modes to the RTW propagation phenomenon, Fenwick and Villard [1963] proposed that RTW

signals might travel over an east-west path via multiple ground hops in the daylit hemisphere, and by the ground-detached mechanism, launched and recovered by the twilight-zone tilts, in the night region. In an experimental test of their hypothesis, they monitored westward-directed transmissions from Okinawa at sites along the great circle path in Guam and the Mediterranean and noted that, while strong RTW echoes were observed when both the transmitter and the receiver were in or near the daylight hemisphere, no signals were received simultaneously at the stations which were then in deep night. Since the signal was believed to be traveling the great-circle route, it had presumably passed over these latter stations in a ground-detached mode. The observed presence of the circulating signal correlated well with predictions based upon the presumed mode-coupling action of the twilight-zone tilts, providing concrete evidence for the existence of a naturally-occurring ground-detached propagation mode at HF.

2.2.2 Experiments using satellites in the ionosphere

The foregoing experimental evidence for the ground-detached mode was obtained using ground-based radio terminals, which are located outside the region where such propagation occurs. Consequently, this evidence is largely inferential, as it presumes the existence of suitable coupling agents and is therefore "colored" by their characteristics. To avoid this complication, Barker and Grossi [1966, 1970] conducted an experiment to measure the properties of HF/VHF radio propagation between satellites situated within the duct itself. A pair of satellites, one transmitting and the other receiving, were placed in similar orbits just below the F layer ionization peak, and their relative velocities were set so that they achieved mutually antipodal positions three times in the course of their 5 November to 24 December 1966 useful life. It was found that a satellite-to-satellite propagation path existed at least 50% of the time at 34.3 MHz, and that the signal reception probability increased as the satellite orbits decayed to lower altitudes, in accord with their predictions based upon ray-tracing studies of the ground-detached mode. They further confirmed the presence of this mode by showing that, while the receiver satellite was recording strong signals from its companion, these signals were

often inaudible at a ground station directly below the receiver satellite. The losses measured along the elevated paths were often less than the free-space losses, implying a degree of focusing. Time spreading of the signal due to multipath propagation was always less than 500 μsec, indicating a propagation mode with very little multipath spreading.

A review of experiments involving satellite-to-ground propagation over great distances is given by Carrara et al. [1970].

2.2.3 Theoretical studies

Accompanying the foregoing experimental evidence for the existence and advantages of the ground-detached mode, and in part prompted by it, is a body of theoretical studies. This propagation mechanism appears under a variety of names in literature, the most common being "whispering-gallery" (after its resemblence to the acoustical phenomenon encountered in properly constructed chambers), "tilt-mode," "chordal-hop," "ducted propagation," and "guided propagation."

The pioneering sliding-wave hypothesis of von Schmidt [1936] has already been mentioned. Another early effort was that of Woyk [1959] who, extending the geometrical-optics investigations of Bremmer [1949], established the general characteristics of the radio ray propagation modes which circulate below the ionospheric peak. The whispering-gallery nature of the lower ionosphere at VLF has been examined by Wait [1962, 1967] and by Budden and Martin [1962].

Of more immediate interest are several recent investigations of ground-detached propagation at HF and VHF. It is well-known [e.g., Woyk, 1959] that propagation via this mechanism is theoretically always possible when the radio energy is properly launched in an ionosphere whose refractive index possesses perfect spherical symmetry. In a pair of studies conducted using computer raytracing techniques, Wong [1966] and Grossi and Langworthy [1966] have shown that the detached mode, once established, can survive the potentially disruptive effects of twilight-zone tilts and other ionospheric irregularities, and it thus offers a mechanism for repeated RTW circulations. Wong traced such rays through 5 complete RTW orbits. In a parallel simulation study, Barker and Grossi [1966] included collisional absorption effects and reported that signals propagated via the detached mode may be as much as 30 dB stronger than

their counterparts traveling by the ground-hop route. (However, they do not specify the transmitter-receiver separation at which this figure was calculated, nor do they indicate the nature of the underlying ground.) They also determined that the MUF for the detached mode was approximately twice that for the ground-hop propagation mechanism.

More recently, Chang [1971a,b] considered the leakage of HF radio energy through the ionosphere via a mechanism analogous to the "tunneling" effect of quantum mechanics, and determined that the least attenuated ground-detached mode in a Chapman model F layer should weaken by 10.8 dB in a complete RTW transit. This figure agrees with the experimentally-measured attenuations of multiply-circulating RTW signals. Chang estimated a MUF value of 6.1 times the F layer critical frequency for ground-detached propagation, which is in agreement with the Barker and Grossi [1966] value of this parameter. While ground-detached propagation beneath the E layer is theoretically possible at a MUF 14.9 times the layer critical frequency, according to Chang, these signals are greatly attenuated by collisional processes and propagation to large distances via this mode is not feasible.

Related theoretical calculations have been published by Gurevich and Tsedilina [1973]. Treating the ionosphere as a barrier of potential trapping the radio wave field, they developed methods for establishing the existence of the elevated ducts and explored the conditions under which radio energy could be injected into the earth-detached mode. In a corollary study, Tushentsova et al. [1974] combined these results with worldwide maps of the ionospheric ionization distribution characteristics to obtain global charts of the parameters of the elevated ducts guiding the ground-detached mode.

2.3 The Motivation for the Work Reported Here

The studies cited above show that HF and VHF radio signals can travel to very great distances via an ionospherically-supported propagation mode which exhibits anomalously low signal losses and distortions, and allows propagation at frequencies considerably greater than those permitted by the usual ground-hop mechanism. The most likely candidate is the ground-detached mode which, owing to its ability to avoid ground

contact and also to remain above the absorbing region in the lower ionosphere, is freed of the associated losses and, moreover, is spared the multipath distortion effects arising from non-specular reflection from rough ground. Direct experimental evidence for the existence of this mode has been obtained. Theoretical analyses have shown that it is a possible means of propagation for distances up to several RTW transits, and have also confirmed its expected low-loss character.

It would be useful to be able to utilize the ground-detached mode on a routine basis. However, some means of coupling the signal energy into the elevated mode must be provided. In the naturally-occurring instances of this type of propagation, this function, together with the inverse process of recovery, is thought to be performed chiefly by ionospheric tilts favorably located relative to the transmitter and receiver. This need for geophysical cooperation, however, greatly restricts the paths and time intervals over which this mode may be used.

Alternative coupling processes exist and have been examined in the literature. Among these mechanisms are quasi-spherical ionization irregularities which refract or scatter the radio energy so that it enters or exits the elevated duct. These irregularities are usually assumed to occur naturally, but recently Gurevich [1971] has proposed that a very strong highly directed beam of radio energy might, by modifying the physical parameters of the ionospheric region it traverses, create its own injecting coupler.

Another class of coupling agents consists of long, thin radio wave reflectors, such as the ionized trails left by meteors, and the columnar ionization irregularities aligned with the geomagnetic field which are thought to accompany the aurora and certain of the spread-F type ionospheric disturbances. These structures reflect an incident radio signal into a cone, coaxial with the reflecter, whose apex half-angle is equal to the angle that the incident ray makes with the column axis. Some of this reflected energy may enter the ground-detached mode or, in the reciprocal process, a signal may be deflected from this mode to a ground station.

While it is well known that this mechanism does exist [e.g., Davies, 1969, p. 339], the author has found little treatment of it in the

literature. There has been published an extensive body of work treating trans-horizon propagation via reflection from meteor trails and columnar auroral structures; however, the investigators have almost invariably neglected the refractive effects of the ionospheric medium containing the scatterers. Invoked chiefly to simplify the geometrical aspect of the investigations, and usually justified for the VHF/UHF frequencies considered, this approximation nevertheless excludes all consideration of ionospherically-supported propagation modes which might be generated in the process. Perhaps owing to the difficulty of combining the geometry of reflection of these columnar scatterers with the non-homogeneous ionospheric refracting medium, a general study of the mode-conversion capabilities of these scatterers does not appear to have been made.

It is therefore the purpose of this chapter and the one following to present the details and results of such a study establishing the necessary geometrical conditions for, and indicating the efficiency of, this mode-conversion mechanism.

2.4 Radio Ray Propagation in a Spherically-Symmetric Medium

2.4.1 Basic concepts

It is the purpose of this section to determine the physical constraints which the detached mode must satisfy, and thereby to lay the foundation of an analysis of the mode-coupling properties of columnar reflectors embedded in the ionosphere. This investigation will be based upon ray theory. To make the problem tractable, the ionosphere will be modeled as a spherically symmetric geoconcentric refracting medium. Since only radio frequencies in the high HF and low VHF bands are to be considered, geomagnetic and collisional effects will be neglected, so that the ionospheric refractive index μ is real, isotropic, and a function only of the radial distance r from the center of the earth.

Ray propagation in a spherically-symmetric medium is governed by Bouguer's rule, which states that [Born and Wolf, 1970, p. 123]

$$\mu r \cos \beta = K_B \tag{2.1}$$

where β is the local elevation of the ray, measured upward from the

local horizontal (see Figure 2.3), and K_B is a constant which is characteristic of each ray. In regions where μ is constant, (2.1) represents a straight line in polar coordinates. Setting $\mu = 1$ and $\beta = 0$ gives $K_B = r_p'$ which, as Figure 2.3 illustrates, represents the equivalent free-space periapsis distance of the ray trajectory.

2.4.2 Constraints upon rays propagating in the ground-detached mode

This inquiry must answer two principal questions: 1) What are the altitude boundaries of the elevated duct guiding the ground-detached mode? 2) What attitude must the ray assume in order to be confined within the duct? We begin by examining the reflection process to determine which rays execute perigees above the ground, and are therefore propagating in the detached mode.

Reflection can occur only at a point where the ray becomes horizontal, which happens at the values of r satisfying

$$\mu r = K_B = r_p' \tag{2.2}$$

The subsequent course of the ray depends upon its curvature at this point. According to Kelso [1968], the radius of curvature ρ of the raypath at its horizontal point is given by

$$\frac{1}{\rho} = \frac{1}{\mu r}\left|\mu - \frac{d}{dr}(\mu r)\right| \tag{2.3}$$

For $d(\mu r)/dr < 0$, $\rho < r$, and an apogee occurs; while for $d(\mu r)/dr > 0$, $\rho > r$ or $\rho < 0$, and the ray executes a perigee. The case of $d(\mu r)/dr = 0$ is of some specialized interest, for then $\rho = r$, and the ray orbits forever at the altitude r. This propagation mode has been investigated by Woyk [1959], and by Lipa and Croft [1975].

The product μr and its first derivative are thus seen to be of fundamental importance in the study of ray propagation in a spherically-symmetric medium. It is possible to determine the principal characteristics of these ray propagation modes, i.e. apogee and perigee altitudes and whether a given ray is in the ground-hop or the ground-detached mode, using the μr vs. r profile for the medium. This approach has been employed by Bremmer [1949], Woyk [1959], and Danilin [1967], and has

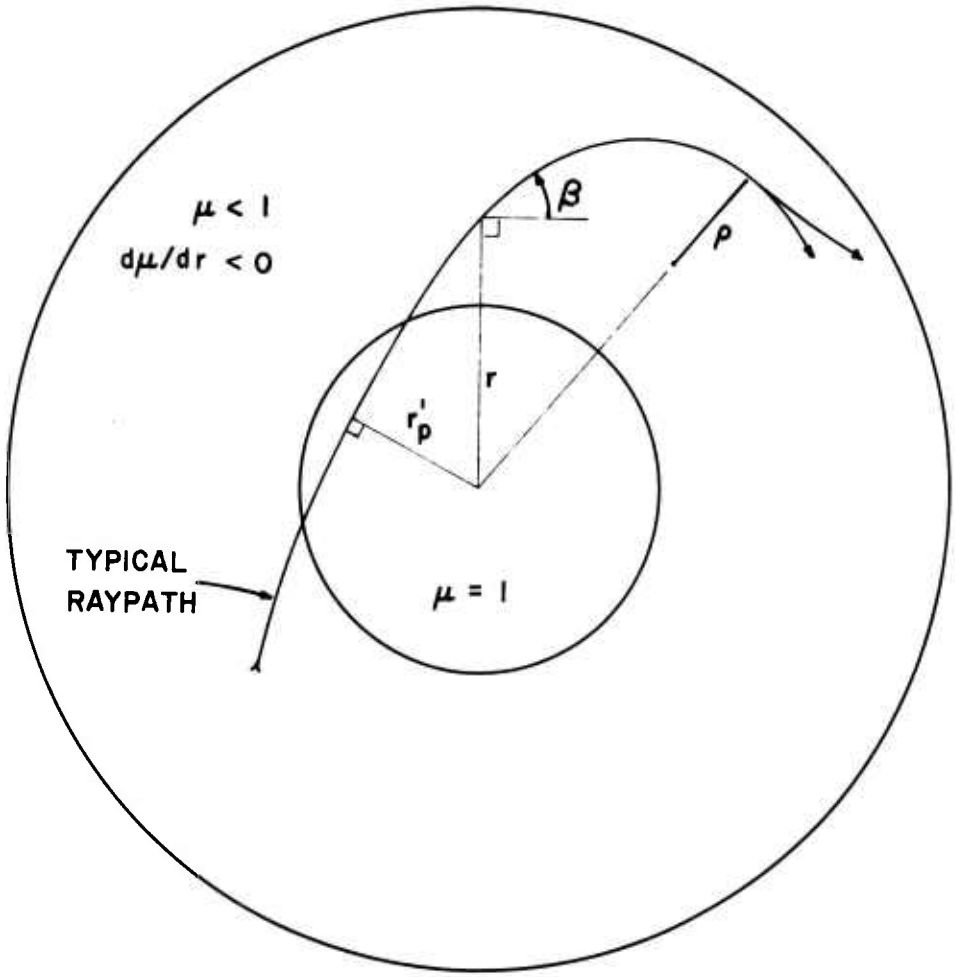

Fig. 2.3 The parameters describing ray propagation in a spherically-symmetric refracting medium.

been developed to a particularly high degree by Kelso [1963, 1968]. In the following text, this technique will be utilized to illustrate the progression of ionospheric ray propagation modes from those rays which are not reflected by the ionosphere, through the ground-hop mode, to the ground-detached mode. This process leads to the formulation of the relevant ground-detached ray duct parameters in terms of the altitude excursions and local elevation angle of a "marginal ray" appropriately chose to define the particular duct. The former discussion is essentially an adaptation of that of Kelso [1963], while the author believes the "marginal ray" concept to be original as developed herein.

A μr vs. r profile depicting representative ionospheric refractive conditions is shown in Figure 2.4. This diagram is based upon the double-layered model ionospheric ionization density profile IID 166 [Croft, 1966], which consists of two Chapman layers combined according to

$$f_N^2(h) = \text{MAXIMUM } (f_{NE}^2, f_{NF}^2) \tag{2.4}$$

where $f_N(h)$ is the plasma frequency at the height h above the earth's surface, and

$$f_{NE}^2 = f_{cE}^2 \exp (1 - z - \exp [-z]) \tag{2.5}$$

$$z = (h - h_{mE})/H_{sE} \tag{2.6}$$

The quantity f_{NF}^2 is given by a similar pair of expressions. The numerical values of the parameters are listed in Table 2.1, and the actual f_N vs. h profile is shown as the broken line in Figure 2.5.

TABLE 2.1. Values of the Parameters Defining Model Profile IID 166

	E	F
f_c	3 MHz	9 MHZ
h_m	120 km	300 km
H_s	15 km	90 km

Since geomagnetic and collisional effects are disregarded, the refractive index is given by the simplified Appleton-Hartree formula [Budden, 1966]

$$\mu^2 = 1 - (f_N/f)^2 \tag{2.7}$$

A radio wave frequency f of $3\ f_{cF}$ was used in computing the μr vs. r profile of Figure 2.4. This profile-frequency combination realistically illustrates the radio ray propagation mode characteristics of interest.

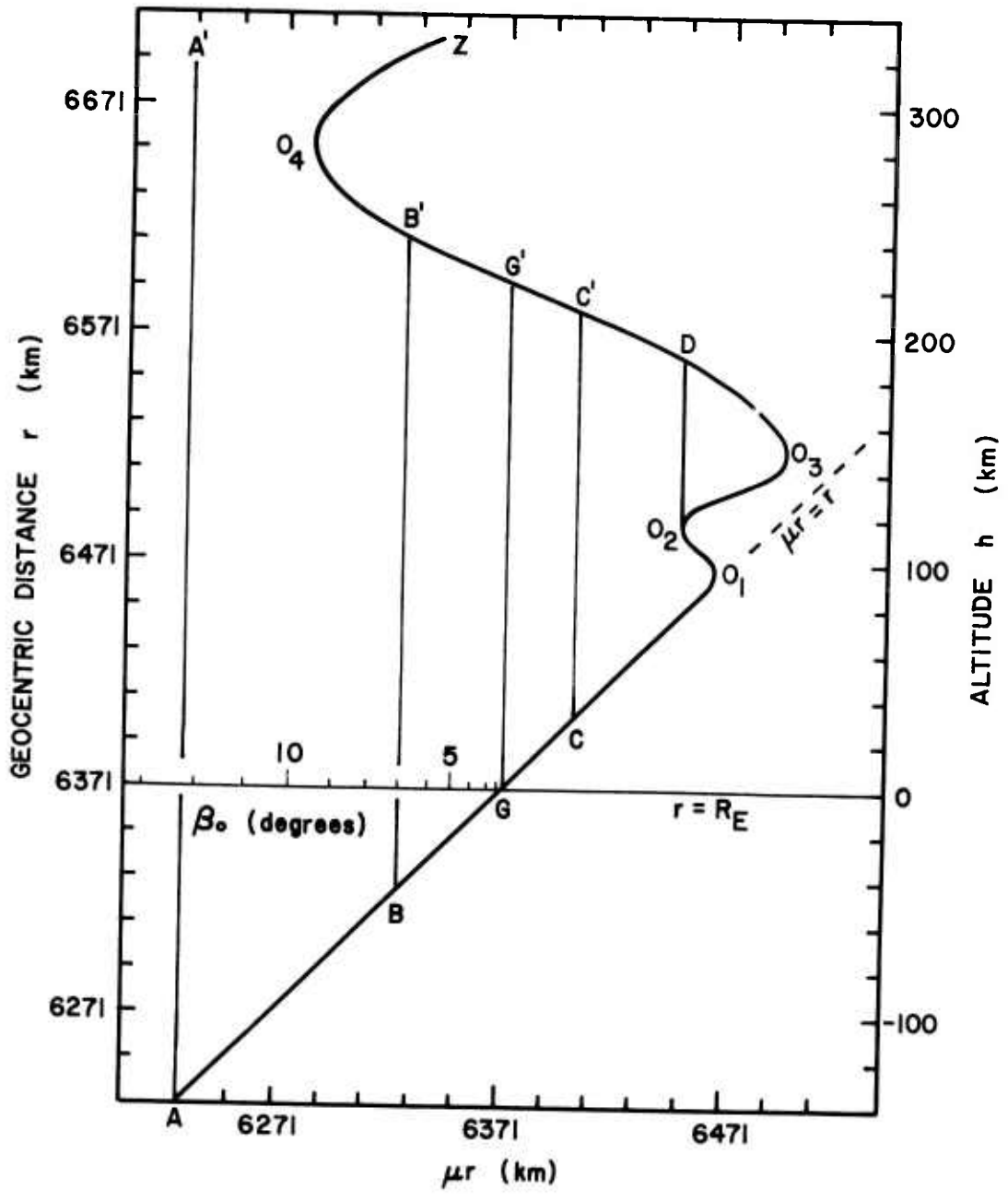

Fig. 2.4 The μr diagram for the 2-layer Chapman ionospheric model profile IID 166, for a radio frequency of 3 times the F layer critical frequency.

Figure 2.4 is labeled in terms of both the geocentric radial distance r and the corresponding altitude h above the earth's surface, which in turn is represented by the horizontal line labeled $r = R_E$. The μr curve reflects the principal structural features of the two layered ionospheric profile. At the lower altitudes, where the ionization density is negligible, it follows the straight line $\mu r = r$. As the free electron concentration becomes significant, the locus departs from the linear form and passes through a local minimum associated with the E layer ionization peak, then through a maximum corresponding to the interlayer ionization trough, and subsequently executes a deep minimum in the F region. Lastly, since the ionization density decreases essentially monotonically with increasing altitude above the F layer peak, the final portion (not shown) of the μr curve consists of a gradual return to the $\mu r = r$ line.

On this diagram, Bouguer's rule $\mu r \cos \beta = K_B$ defines a family of straight vertical lines, each of which corresponds to a particular value of K_B, and thus represents a particular ray. The intersections of these verticals with the μr locus denote the horizontal points of the associated rays since, at these intersections, $\mu r \cos \beta = \mu r$. The region to the right of the μr curve is a forbidden zone because, to propagate here, a ray would have to satisfy $\mu r \cos \beta > \mu r$.

The μr curve defines uniquely the altitude limits between which any given ray is confined. Applying the derivative conditions stated earlier, it is seen that the segments AO_1, O_2O_3, and O_4Z are perigee regions, while O_1O_2 and O_3O_4 constitute apogee regions. Every ray whose associated vertical lies to the right of O_4 is thus confined within a duct bounded above by an apogee region and below by a perigee zone.

The nature of the ionospheric duct guiding a given ray may therefore be determined by locating the vertical line corresponding to its characteristic value of K_B. Employing the concept of the equivalent periapsis distance r_p', the K_B associated with each vertical is equal to the value of r at which the line (extended, if necessary) meets the $\mu r = r$ locus. Thus, the verticals corresponding to progressively larger values of $r_p' = K_B$ are positioned successively to the right of one another.

Inspection of Figure 2.4 reveals that four principal types of radio ray propagation exist in the ionosphere. The first of these, corresponding to the lowest K_B values, is represented by the vertical AA', for which $K_B = r_p' = 6250$ km. Because this periapsis distance is less than the radius of the earth, the ray strikes the ground at an elevation angle given by

$$\cos \beta_0 = \frac{K_B}{R_E} = \frac{r_p'}{R_E} \tag{2.8}$$

This angle is indicated by the scale marked on the $r = R_E$ line for all rays having a subterranean periapsis. Since the AA' locus does not meet the μr curve in the ionospheric region, such rays do not reflect, but instead penetrate the ionosphere. Rays of this class are not ducted, but represent signals transmitted into or received from outer space.

The second group is represented by BB'. Like their type 1 counterparts, these rays have $r_p' < R_E$, and thus strike the ground. However, their loci intersect the μr curve within an apogee segment, so that these rays are returned to earth, where they are again reflected from the ground. These type 2 rays therefore comprise the ground-hop mode.

Like the preceding group, the rays of the third type, represented by CC', are reflected downward from the ionosphere. However, their associated verticals meet the μr curve at $r_p' > R_E$. These rays therefore do not reach the ground; instead, the sub-ionospheric portions of their trajectories are straight-line tangents to the spheres defined by the associated values of r_p'. These are chordal raypaths, such as those depicted in Figure 2.2, and this ground-detached mode comprises the "whispering-gallery" propagation mechanism.

To the right of O_2D are the rays of the fourth type of propagation mode, which are confined within a duct formed by the lower F and upper E ionospheric layers. Several such interlayer ducts may exist in the natural ionosphere, due to the multiple ionization peaks often found in actual $f_N(h)$ profiles. For the present purposes, the ground-detached modes represented by types 3 and 4 are equivalent.

Inspection of Figure 2.4 reveals that, given the vertical corresponding to any ray propagating in the detached mode, all rays whose verticals lie to the right of it are also in this mode. Since K_B increases to the right, a necessary and sufficient condition for a ray to belong to such a ducted group is that $K_B > K_{Bm}$, where K_{Bm} is the Bouguer's constant of the chosen ray. This ray may therefore be taken as the boundary, or marginal, ray defining the particular elevated duct. A natural candidate for this marginal ray is the ray which just grazes the earth's surface, represented by GG'. Other choices are possible; for example, it might be desired to specify a duct whose lower boundary is above the absorbing D region.

For the sake of illustration, let CC' represent the marginal ray, with $K_B = K_{Bm}$. The trend of the μr locus then shows that all rays within the elevated channel thus defined execute their apogees at successively lower altitudes, and their perigees at successively higher altitudes, as K_B increases from K_{Bm}. Hence, the ducted rays are confined within an altitude zone bounded by the apogee and perigee altitudes of the marginal ray. Conversely, any ray whose path crosses these boundaries does not belong to the ducted group, as its vertical must therefore be to the left of the marginal ray locus.

At any geocentric altitude r_0 within the duct, the elevation $\beta_m(r_0)$ of the marginal ray is given by

$$\frac{\mu r_0 \cos \beta_d(r_0)}{\mu r_0 \cos \beta_m(r_0)} = \frac{K_{Bd}}{K_{Bm}} \tag{2.9}$$

Since $K_{Bd} > K_{Bm}$

$$|\beta_d(r_0)| < |\beta_m(r_0)| \tag{2.10}$$

Conversely, any ray for which $|\beta(r_0)| > |\beta_m(r_0)|$ cannot belong to the ducted group since, by (2.9), this requires that $K_B < K_{Bm}$, which violates the condition for such membership as established in the preceding paragraph. We may therefore define at any given altitude within an elevated duct a quantity called the angular width of the duct, which

expresses the range of elevation angles which the trapped rays must assume. The foregoing development shows that this angular width is equal to $|\beta_m(r_0)|$.

These are general results. They are based solely upon the properties of the ray channels formed by the confluence of the monotonically increasing lower section and the monotonically decreasing upper section of the μr vs. r curve. Since $\mu \approx 1$ in the lower atmosphere, the former condition, corresponding to the $\mu r = r$ segment, will always be met. The monotonically increasing upper section will be present if the refractive power of the ionosphere is sufficient to create an apogee region at the particular radio frequency, otherwise no ionospherically-supported radio propagation is possible.

A ground-hop to ground-detached mode coupler must therefore satisfy two criteria: 1) it must be physically located within the duct, between the perigee and the apogee altitudes of the marginal ray, and 2) it must be able to flatten the incident ray trajectory sufficiently to satisfy the inequality (2.10) in order to launch the detached mode, and to perform the inverse transformation to recover energy from the duct.

2.4.3 Determining the altitude boundaries and angular widths of elevated ducts directly from $f_N(h)$ profiles

Having demonstrated how the parameters of an elevated duct may be expressed in terms of the parameters of the marginal ray, we wish to be able to ascertain these quantities in a given ionospheric $f_N(h)$ profile. It is the purpose of this section to develop a graphical overlay technique which finds the altitude boundaries and angular widths of such ducts at any given radio frequency.

Several methods of determining the duct parameters have appeared in the literature. All of these utilize the refractive index of the medium in conjunction with either a) the μr diagram [Woyk, 1959; Kelso, 1968], or b) the modified refractive index (rectification to a flat earth) [Danilin, 1967; Chang, 1971a,b], or c) computer raytracing [Barker and Grossi, 1970]. The need for the $\mu(h)$ profile introduces an additional labor step into the process and also severely limits its

versatility, since the refractivity profile must be recomputed whenever the frequency is changed. The technique developed below bypasses this requirement, and yields results of accuracy comparable to the other non-raytracing methods.

The basis of this technique is the graphical solution of the simultaneous equations

$$h = h(\log f_N) \tag{2.11}$$

which is the ionospheric plasma frequency profile plotted in the usual logarithmic-frequency format, and

$$h = g(\beta, K_B, \mu(f, f_N)) \tag{2.12}$$

which is an appropriate formulation of Bouguer's rule. Since μ is a function of the ratio f_N/f, it is also a function of the quantity $\log f_N - \log f$. Therefore, when (2.11) can be put in the form

$$\log f_N = g_1(\beta, K_B, h) + \log f \tag{2.13}$$

any value of the operating frequency f can be accounted for by shifting the curve family representing g_1 along the $\log f_N$ axis of the ionospheric profile plot. A suitable family of $g_1(h, K_B, \beta)$ curves need therefore be constructed only once for each duct parameter to make an overlay which, when appropriately placed upon the $\log f_N(h)$ profile, yields the desired information.

Consider first the problem of finding the altitude boundaries of the duct defined by the marginal ray with $K_B = r'_{pm}$. Each boundary is represented by the geocentric altitude r of an apsis of this ray, where Bouguer's rule requires that

$$\mu r = r'_{pm} \tag{2.14}$$

Applying (2.7) and rearranging gives

$$1 - \left[f_N/f\right]^2 = (r'_{pm}/r)^2 \tag{2.15}$$

$$f_N^2 = f^2 \left[1 - (r'_{pm}/r)^2\right] \tag{2.16}$$

$$\log f_N = \frac{1}{2} \log \left| 1 - (r'_{pm}/r)^2 \right| + \log f \qquad (2.17)$$

This expression has the required form (2.13). The corresponding overlay is constructed by setting $\log f = 0$ and plotting a family of curves parametric in r'_{pm}. It is convenient to present this overlay in terms of the geographic altitudes $h = r - R_E$ and $h'_{pm} = r'_{pm} - R_E$. The resultant overlay is shown in Figure 2.5 (solid lines). The rightmost boundary of the frame corresponds to $r'_{pm} = 0$; since it therefore represents $\log f$, it forms a cursor to establish the placement of the overlay on the $\log f_N$ axis. For convenience, auxiliary cursors are provided at $\log(f/10)$ and $\log(f/100)$.

To locate the duct boundaries in an ionospheric profile, the overlay is positioned on the profile plot with the respective altitude scales in register, and with the frequency cursors aligned with the values of f_N representing the corresponding multiples of the radio operating frequency. For illustration, the curve family of Figure 2.5 is shown superimposed on the IID 166 profile for a radio frequency of 27 MHz, which is 3 times the F layer critical frequency.*

The boundaries of a duct defined by the marginal ray corresponding to a specified h'_{pm} are the altitudes at which the corresponding locus meets the $f_N(h)$ curve. Since, as the μr diagram shows, such channels can exist only beneath or between ionospheric layers, only those portions of the overlay curves to the right of the $f_N(h)$ profile represent actual ducts. Thus, referring to Figure 2.5, the marginal ray for which $h'_{pm} = 100$ km defines a type 4 duct bounded by $h = 132$ km and $h = 172$ km, while the segment of the $h'_{pm} = 0$ locus between profile intersections at $h = 222$ km and $h = 344$ km does not correspond to any duct. Instead, the 222 km intersection is the upper limit of the channel whose lower boundary is at the earth's surface. Since this curve has no lower intersection with the $f_N(h)$ profile, the equivalent perigee height h'_p is equal to the actual perigee height h_p.

---

* This combination of ionization density profile and radio frequency is the same as was used to construct the μr diagram of Figure 2.4. This duplication permits the results the results obtained using the present technique to be checked against that established method.

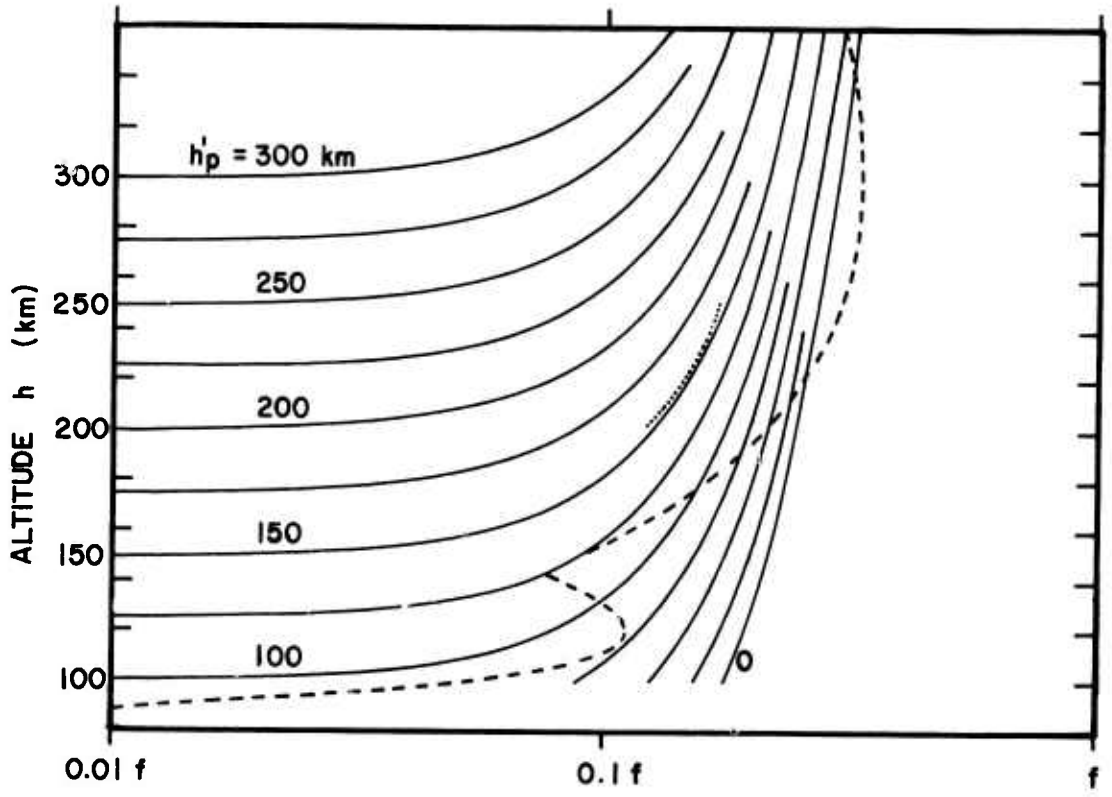

Fig. 2.5 The sliding overlay for finding the altitude boundaries of the elevated ducts defined by the marginal rays of equivalent periapsis altitudes h'_p. It is shown in use with the IID 166 model ionospheric profile (broken line) at a radio frequency of 3 times the F layer critical frequency.

In essence, this procedure finds the altitudes at which a given ray becomes horizontal. It has been tacitly assumed that the upper member of a pair of profile-overlay intersections corresponds to a ray apogee, and the lower to a perigee. But whether an apogee or a perigee occurs depends upon the sign of $d(\mu r)/dr$, and thus upon that of df_N/dr, at the ray horizontal point. The matter can be resolved by comparison of the slopes of the overlay and $f_N(h)$ curves at their intersections. Since the overlay curves are plots of the function $\mu r = K_B$, their slope is given by $d(\mu r)/dr = dK_B/dr = 0$. As was indicated previously, this defines the critical gradient of μr (and thus of f_N) dividing the apogee and perigee regions. Consequently, if the profile slope df_N/dr exceeds the slope of the intersecting overlay curve, an apogee occurs, if the inverse happens, there must be a perigee. This latter interpretation is the basis for an overlay curve set devised

by Croft [1967a] for the purpose of identifying apogee and perigee regions within a given $f_N(h)$ profile.

It remains to determine the angular width $|\beta_m|$ of a specified duct at a given altitude and frequency. Equivalently, we must find the absolute value of the elevation of the marginal ray. Bouguer's rule gives

$$\mu r \cos \beta_m = r'_{pm} \tag{2.18}$$

from which

$$1 - \left|f_N(r)/f\right|^2 = \left(r'_{pm}/r \cos \beta_m\right)^2 \tag{2.19}$$

and

$$\log f_N = \frac{1}{2} \log \left|1 - \left(r'_{pm}/r \cos \beta_m\right)^2\right| + \log f \tag{2.20}$$

where μ and β_m are functions of r.

In this case there are two parameters, r'_{pm} and $|\beta_m|$, so that several families of overlay curves must be plotted. Since, in practice, many values of $|\beta_m|$ may need to be determined within a given duct, it is logical to make a separate overlay for each of several representative r'_{pm} values. These curves are shown in Figure 2.6 for $h'_{pm} = r'_{pm} - R_E = 0$ and 100 km.

To illustrate their use, these overlays are shown superimposed on the IID 116 profile for an operating frequency of 27 Mlz. At any given height within the duct corresponding to the particular overlay, $|\beta_m|$ is given by the parameter of the curve intersecting the $f_N(h)$ profile. For example, the upper panel of Figure 2.6 shows that all rays propagating at $h = 214$ km with absolute elevations less than 5° belong to the $h_{pm} = 0$ ducted group. At 178 km, these angular limits have doubled; and the maximum $|\beta_m|$ of 11.2° for this duct occurs at the bottom of the E-F interlayer valley at 144 km. Comparison of the upper and lower panels of Figure 2.6 shows that, as the duct beomes physically smaller (h'_{pm} increasing), the angular width at a given height decreases.

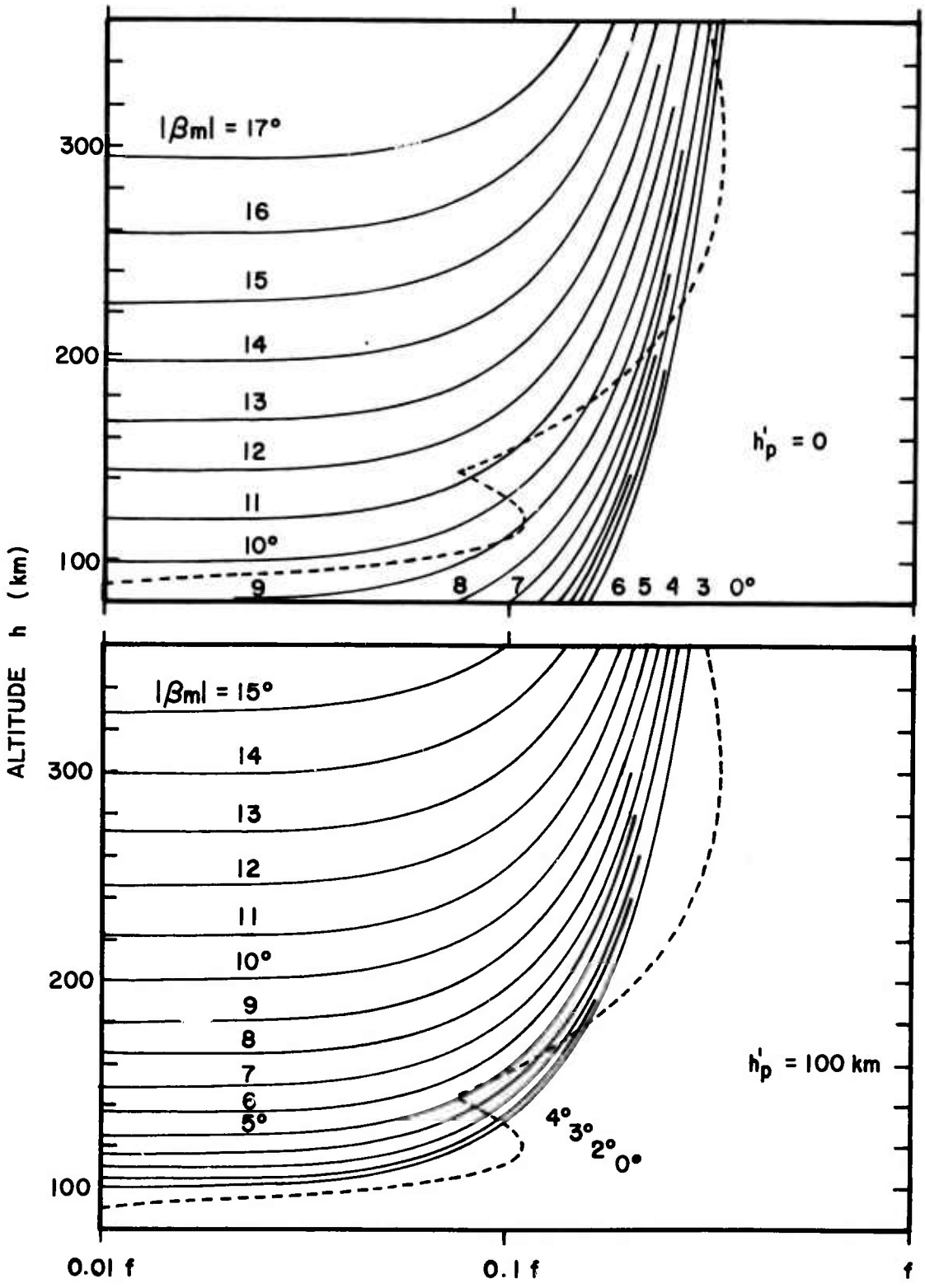

Fig. 2.6 The sliding overlays for finding the angular width as a function of height for the ducts corresponding to the marginal rays of the specified equivalent periapsis altitudes h'_p. Both overlays are shown in use with the profile IID 166 (broken line) at a radio frequency of 3 times the F layer critical frequency.

It is worthwhile to note that the $\beta_m = 0°$ contours on the upper and lower panels of Figure 2.6 are identical, respectively, to the $h'_{pm} = 0$ and $h'_{pm} = 100$ km loci on Figure 2.5, and can therefore be used to locate the duct limits. This follows from the fact that (2.17) is identical to (2.20) with $\beta_m = 0$.

This correspondence between the two expressions might be exploited by defining a new parameter r''_{pm} according to

$$r''_{pm} = r'_{pm}/\cos \beta_m \tag{2.21}$$

and expressing (2.17) and (2.18) in the common form

$$\log f_N = \frac{1}{2} \log \left| 1 - \left(r''_{pm}/r\right)^2 \right| + \log f \tag{2.22}$$

This expression defines a curve family parametric in r''_{pm} which performs the combined functions of the overlays for the angular width and boundaries, provided some auxiliary means is furnished to indicate the various paired values of $|\beta_m|$ and r'_{pm} to be associated with each r''_{pm}. While this device avoids the necessity for a set of overlays, it is somewhat more difficult to use.

Owing to the sliding-scale method of accounting for the radio operating frequency, this overlay technique permits the ready exploration of the effects of frequency changes. For example, if one imagines the overlay curves of Figure 2.5 slid rightward, it is seen that the associated rise in frequency increases the upper boundary altitude of a given duct. Likewise, Figure 2.6 shows that the duct angular width at a given altitude increases as the frequency rises, and so does the maximum $|\beta_m|$ in the duct. An important problem, to find the maximum frequency at which a signal may be captured beneath the ionization peak of a given profile, may be solved by using the overlay of Figure 2.5 to determine the frequency at which the last possible duct vanishes. This occurs at the frequency beyond which no overlay curves may be made tangent to the profile, as illustrated by the near tangency of the dotted profile segment and the $h'_{pm} = 150$ km locus on the Figure. The absolute maximum usable frequency thus determined is 49 MHz.

The related question of the highest frequency at which ground-hop propagation may occur is solved by determining the frequency at which the $h'_{pm} = 0$ curve loses contact with the profile. This occurs at 31 MHz in the IID 166 profile. Likewise, the penetration frequencies of rays launched from the ground at various elevation angles β_0 might be found by applying this same procedure using overlay curves plotted for selected values of the parameter $r'_{pm} = R_E \cos \beta_0$

2.5 Summary

Many investigators have reported that the quality of radio signals propagated via the ionosphere over very great distances, including antipodal and RTW paths, is often remarkably good. In particular, it has been noted that, when a signal is received from both the short (direct) and the long (indirect) arcs of a great-circle path, the long-path component is frequently stronger and less distorted than its complement. In addition, such extreme distance propagation has occurred at frequencies significantly greater than the classical MUF for the path. These apparently anomalous events have generally been attributed to the presence of a ground-detached propagation mode which avoids the signal degradations due to ground contact and traverses of the absorbing D region. Further experiments have confirmed the importance and advantages of this mode in long distance ionospheric radio propagation.

However, some mode-coupling mechanism must be provided to make the ground-detached mode available to ground-based radio terminals. In most instances, this coupling has been effected by favorably placed ionospheric tilts; however, a less fortuituous coupling mechanism would be generally required in order to exploit practically the superior propagation characteristics of this mode. One possible mechanism is the reflection of radio waves from ionospheric ionization irregularities such as meteor trails and field-aligned columns. Since no general analysis of the mode coupling properties of these objects has been done, this analysis was undertaken.

To lay the groundwork for this analysis, the requisites for electromagnetic wave propagation in a ground-detached ionospheric duct were established using ray theory. It was shown that any particular duct in

a spherically symmetric, geoconcentric, lossless isotropic ionosphere may be completely characterized by an appropriately chosen marginal ray. The apogee and perigee altitudes of this ray define the altitude boundaries of the duct, and the absolute value of its elevation angle at any altitude defines the duct angular width at that altitude. To propagate within this duct, a ray must therefore be launched a) from a source (an active source or a reflector) physically located within the duct, b) at an elevation angle whose absolute value does not exceed that of the marginal ray at the source altitude.

Finally, a set of overlay curves were developed which, when placed over a log f_N vs. height profile, indicate the altitude boundaries and angular widths of the elevated ducts in the profile. This method differs from previous techniques in that it uses the $f_N(h)$ profile directly, and accounts for varying radio frequencies by means of a sliding scale mechanism. Thus, the required properties of the ground-detached ducts may be determined from a commonly available ionospheric data form, at any desired frequency, without the need to raytrace or to compute at each frequency the actual or plane-earth rectified refractive index.

3. COLUMNAR SCATTERERS AS A COUPLING MECHANISM BETWEEN THE GROUND-HOP AND THE GROUND-DETACHED MODE

3.1 Introduction

It is the task of this chapter to analyze the geometrical properties of the process of coherent scattering of electromagnetic waves by long, thin ionization density irregularities embedded in the ionosphere, and to evaluate the utility of such reflectors as coupling agents between the ground-hop mode and the ground-detached mode.

This analysis comprises two phases. In the first stage, the geometrical distribution of the reflected radio energy will be compared against the geometrical constraints which the ducted rays must satisfy to establish the conditions under which this scattering mechanism will provide the desired coupling. In the second phase, the efficiency of this process will be considered.

3.2 The Scattering of Radio Waves by Columnar Reflectors

The scatterers to be treated here are long, thin cylindrical volumes within which the ionization density, and hence the dielectric constant, differs from that of the surrounding ionospheric medium. Examples include meteor trails and the geomagnetically-aligned irregularities associated with the radio aurora and certain spread-F type disturbances. The theory of electromagnetic wave scattering by these columns is well developed and documented [e.g., Booker, 1956; Wait, 1959; Sato and Maeda, 1968]. To establish the groundwork for the mode coupling analysis to follow, a brief summary of this theory will be presented in the following paragraphs.

Only scattering by underdense ionized columns will be treated explicitly. Such irregularities, in which the plasma frequency is less than the radio frequency, comprise the majority of scatterers of interest here. They scatter only a fraction of the incident signal energy. Overdense irregularities, within which the plasma frequency exceeds the radio frequency, are represented at the frequencies of interest by certain meteor trails immediately after their formation. These reflect radio waves in much the same way as do metallic cylinders, and the geometric

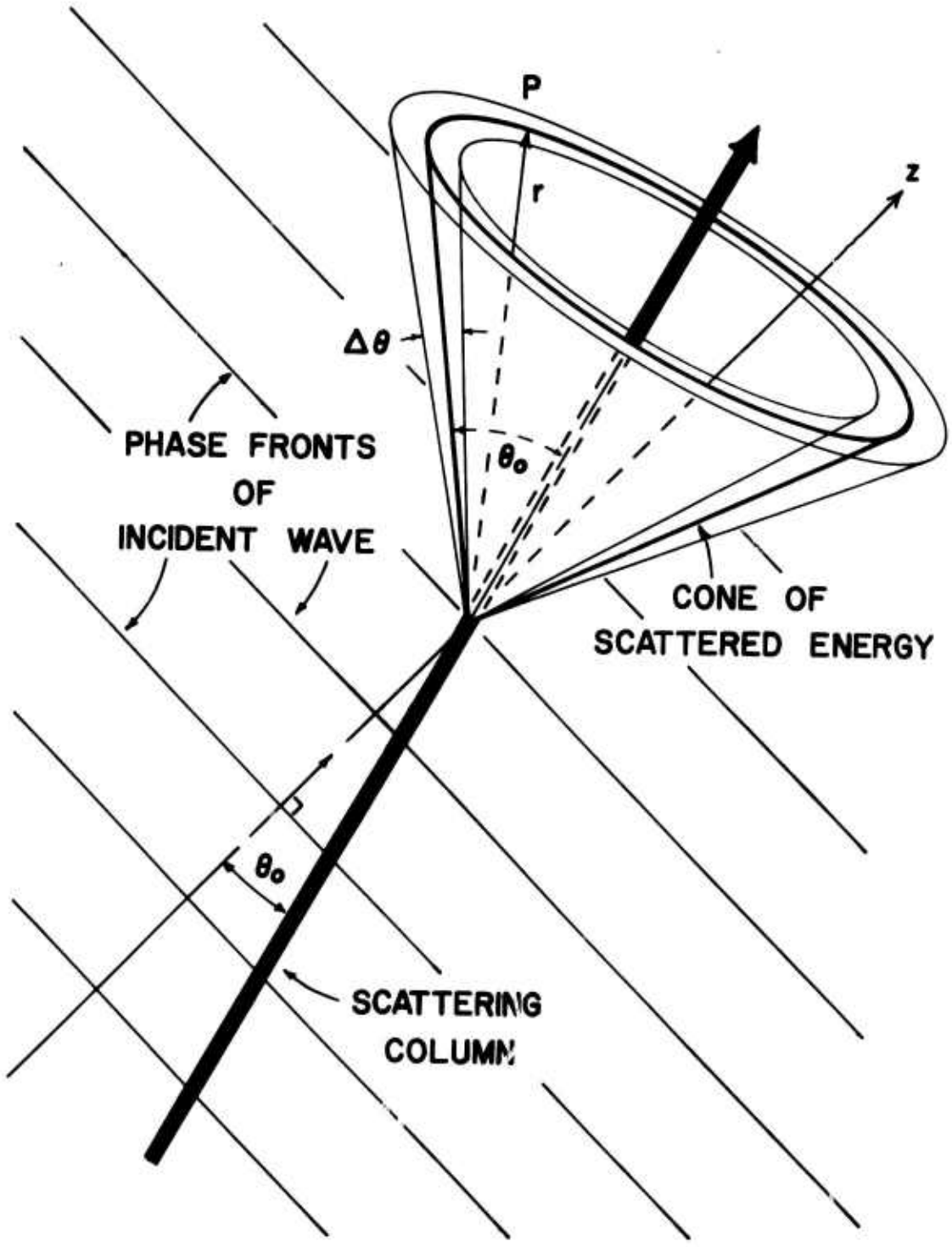

Fig. 3.1 A schematic representation of the geometrical aspects of the scattering of a radio wave by a long, thin column. The wave is incident from the lower left, with its wavenormal directed in the z direction. The reflected energy is concentrated primarily within a conical shell of width $\Delta\theta$ and of apex semi-angle θ_0.

distribution of the scattered energy is qualitatively similar to that of the underdense scattering process, except that total reflection occurs.

As a high-frequency electromagnetic wave travels through a homogeneous, ionized medium, its electric field vector $\underset{\sim}{E}$ causes the free electrons to oscillate in antiphase with $\underset{\sim}{E}$, while the much heavier positive ions remain essentially stationary. The volume polarization $\underset{\sim}{P}$ thereby induced gives the medium a dielectric character, altering the wavelength and propagation velocity, but not changing the direction of travel, of a radio wave [Budden, 1966]. If, however, a localized volume of depleted or enhanced ionization density is introduced, the incident radiation field produces a local inhomogeniety $\Delta\underset{\sim}{P}$ in the polarization density, which in turn gives rise to a re-radiated (scattered) field characteristic of the spatial and phase distribution of $\Delta\underset{\sim}{P}$ [Booker, 1956].

Therefore, referring to Figure 3.1, consider such a volume having the form of a linear cylinder of very large length/diameter (ℓ/d) ratio, illuminated by a plane wave with the phase factor $\exp\,[i2\pi\,(ft - z/\lambda)]$, where λ is the wavelength. The phase of $\underset{\sim}{E}$, and therefore of ΔP, varies along the cylinder as $\exp\,\{i2\pi\,[ft - z/(\lambda\cos\theta_0)]\}$. Thus, provided $d<<\lambda$, the irregularity is analogous to a line antenna excited by a linear phase distribution, and the far-field pattern R of the time averaged re-radiated power has the form [Kraus, 1950, p. 126; Booker, 1956]

$$R \sim \left(\sin\chi\,\frac{\sin\Psi}{\Psi}\right)^2 \tag{3.1}$$

where

$$\Psi = \frac{\pi\ell}{2\lambda}\,(\cos\theta - \cos\theta_0) \tag{3.2}$$

and χ is the angle between $\underset{\sim}{E}$ and the vector $\underset{\sim}{r}$ representing any direction of scattered energy propagation (see Figure 3.1). For θ_0 near 90°, the half-power width $\Delta\theta$ of the main lobe of R is given by [Kraus, 1950, p. 114]

$$\Delta\theta \approx 0.45\,\lambda/\pi\ell \text{ radians} \tag{3.3}$$

For $\ell \gg \lambda$, the expression (3.2) approaches the limiting form

$$\lim_{\lambda/\ell \to 0} R = \sin^2 \chi \, \delta(\theta - \theta_0) \tag{3.4}$$

which defines a cone of apex half-angle θ_0, coaxial with the cylindrical irregularity. This expresses the well-known fact that the underdense scattering mechanism is qualitatively equivalent to a partial specular reflection (see, for example, Booker [1956]).

The purely geometrical formulation of the scattering process represented by (3.4) greatly simplifies the analysis of the propagation paths of the reflected energy, since only the direction corresponding to $\theta = \theta_0$ need be considered. Thus, it is usually invoked immediately in such investigations [e.g, Chapman, 1952; Millman, 1959, 1969, 1974; Leadabrand and Yabroff, 1958; Stathacopoulos and Barry, 1974]. For the same reason, it will be employed here also.

It should be noted that, since the scattering process depends upon the phase of ΔP, which in turn is established by the phase fronts of the incident wave, the aspect angle θ_0* must be measured relative to the direction of incident phase propagation, i.e., relative to the wavenormal vector. Because magneto-ionic effects are neglected in this study, the ionosphere is an isotropic medium, and the wavenormal and ray directions coincide. Thus, in the following text, the terms "ray," "raypath," and "wavenormal direction" are equivalent and denote the local direction of both phase and energy propagation.

3.3 The Geometrical Formulation of the Scattered Energy Distribution

It is now necessary to express the geometry of the cone of energy reflected from cylindrical irregularities in terms of the geographic alt-azimuth parameters. Referring to Figure 3.2, let the reflecting column be represented by the directed line segment OC. Following the measurement conventions of geomagnetism, the orientation of this line is denoted by its dip angle I, measured downward from the local horizon plane, and by its declination angle D, reckoned positive from

* Hereafter, the subscript "0" will de dropped.

geographic north. Let the incident ray, represented by the directed line segment OR, meet the column at the common vertex O of the angles I and D. The sense of OR is the same as the ray propagation direction, which is in turn given by its azimuth α, measured in the same way as D, and by its elevation β.

In practice, α and β will be known, perhaps as the result of a raytracing computation, and the corresponding values of I and D will be specified independently. Given this data, it is necessary to determine the aspect angle θ subtended by the ray and the column. The cone of reflected radio signal energy is then described by the locus of all ordered pairs of (α, β) which correspond to this value of θ.

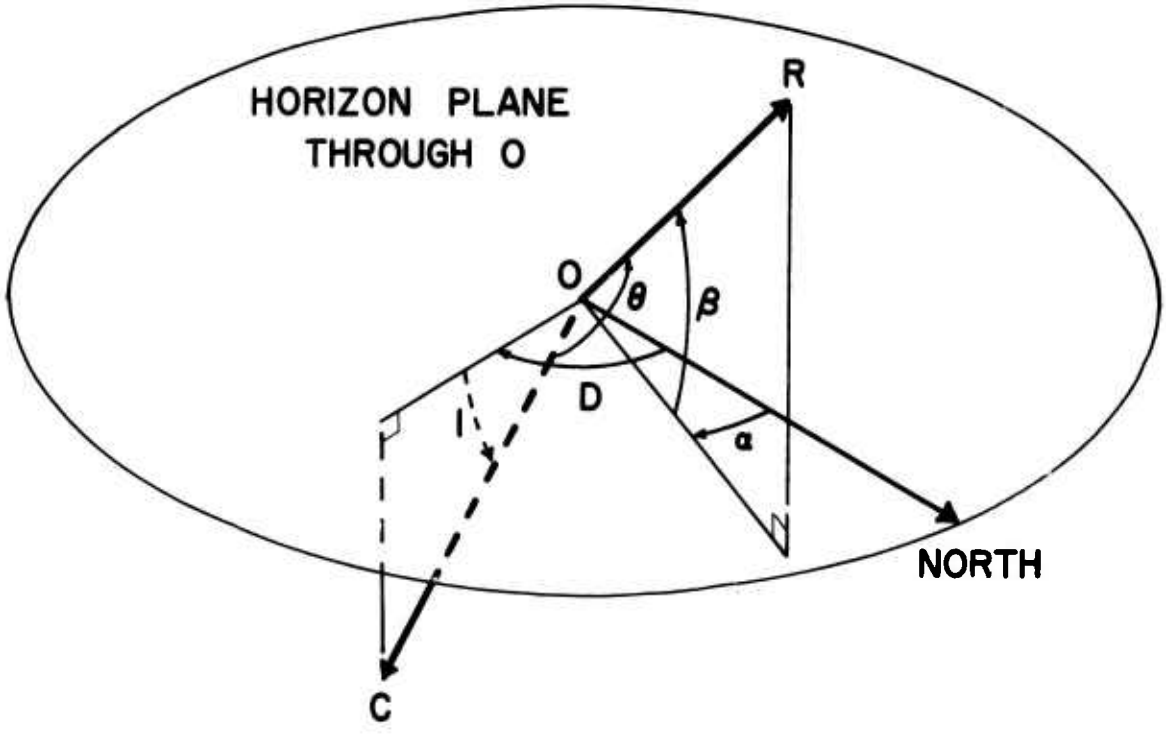

Fig. 3.2 The parameters defining the orientations of the scattering column C and the ray R.

For this purpose we shall adopt the versatile spherical-trigonometric formulation commonly used in the treatment of antenna radiation patterns. This formulation is illustrated in Figure 3.3, where the column and ray elevations have been redefined in terms of the respective angles I' and β', measured downward from the local vertical OV. These new parameters are related to the old by

$$I' = 90° + I \tag{3.5a}$$

$$\beta' = 90° - \beta \tag{3.5b}$$

Since I', β', and θ are central angles with common vertex O, the planes containing them are great-circle planes of the unit sphere O' centered upon O, and these angles may therefore be represented

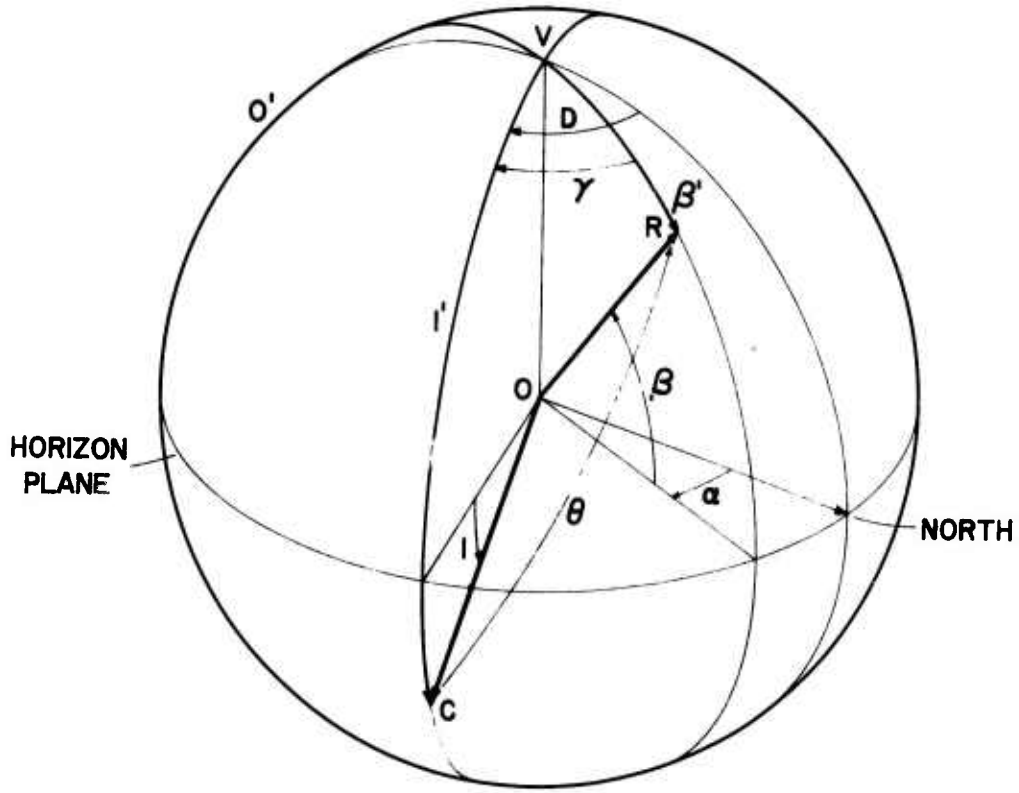

Fig. 3.3 The column and ray orientation parameters in the spherical coordinate formulation.

as great-circle arcs on the surface of O' in the geographic meridian plane through O. Geographic azimuth is analogus to co-longitude in the O' system, and elevation corresponds to latitude.

The aspect angle θ may be found by applying the law of cosines to the spherical triangle RVC; this yields immediately

$$\cos \theta = \cos \beta' \cos I' + \sin \beta' \sin I' \cos (D - \alpha) \qquad (3.6)$$

Substituting (3.5a) and (3.5b) and rearranging gives

$$\cos \theta = \cos \beta \cos I \cos \gamma - \sin \beta \sin I \qquad (3.7)$$

where the azimuth difference $D - \alpha$ has been replaced by γ, the azimuth relative to the meridian CV defined by the plane containing the axis of the scatterer and the center of the earth. This meridian is a natural prime meridian for the O' coordinate system, and it will be employed in all of the following developments. In the frequent case that OC represents a column aligned with the geomagnetic field, CV lies in the geomagnetic meridian plane through O, and γ thus corresponds to geomagnetic azimuth.

The set of (β,γ) combinations satisfying (3.7) for a specified (I,θ) pair uniquely describe the orientations of the rays forming the cone of scattered radio energy. For a given combination of I and θ, equation (3.7) defines a small circle on the surface of O', with its pole at C and of radius θ, thus giving a convenient pictorial representation of the spatial distribution of the reflected energy. This representation will be utilized later to facilitate the analyses of the directionality and efficiency of the mode coupling mechanism.

3.4 The Mode-Coupling Properties of Coherently Scattering Cylinders

The mode-coupling properties of this reflection mechanism will be studied explicitly from the viewpoint of launching the ground-detached mode from a ground-based transmitter, primarily because this process is conceptually more tractable than the inverse process of recovery, but also because this approach deals directly with the important practical problem of establishing the elevated mode as soon as possible after

transmission. The recovery process can in principle be treated by reversing the launching mechanism, since all of the raypaths considered here are self-reciprocal. Alternatively, the recovery may be left to occur naturally through leakage from the elevated duct caused by various irregularities always present in the natural ionosphere.

Therefore, let a reflecting column of dip I be situated in a spherically-concentric ionosphere, and let the point O on this reflector lie within a duct defined by a given marginal ray which passes through O with the elevation $|\beta_m|$. As was shown in Section 2.4.2, all rays passing through O with elevations satisfying $|\beta| \leq |\beta_m|$ will be confined within the duct. In the O' coordinate system, this inequality defines an equatorial zone which contains only and all such rays. Consequently, the given ducted mode will be launched by reflection from the column at O if and only if a portion of the small circle with pole at C and containing the incident ray lies within this zone. An analytic method of determining whether this occurs, for a given combination of column and ray orientations, will be presented later in this section. First, however, an instructive overview of this mode conversion process will be developed via a graphical technique.

3.4.1 Graphical formulation

Figure 3.4 shows the aspect angle θ plotted as a function of β and γ for $I = 45°$. Each curve is parametric in both γ and $\gamma - 360°$, and the rectangle bounded by the $\gamma = 0°$ and $\gamma = 180°$ loci is the domain of all possible combinations of γ, β, and θ for the given value of I. The elevated duct corresponds to the region between the vertical lines $\beta = \pm |\beta_m|$, and the reflection cone is represented by the horizontal line of constant θ passing through the (β,γ) point corresponding to the illuminating ray. Hence, a mode-coupling event is indicated by the extension of such a line into $|\beta| \leq |\beta_m|$ zone. The azimuth sectors into which the ducted mode is launched are given by the γ parameters of the aspect-elevation loci which this line crosses within the zone. For example, the horizontal line AB on Figure 3.4 indicates that a ray incident upon the $I = 45°$ column at $\beta = 63°$, $\gamma = 60°$ or $300°$ (point R) will reflect energy

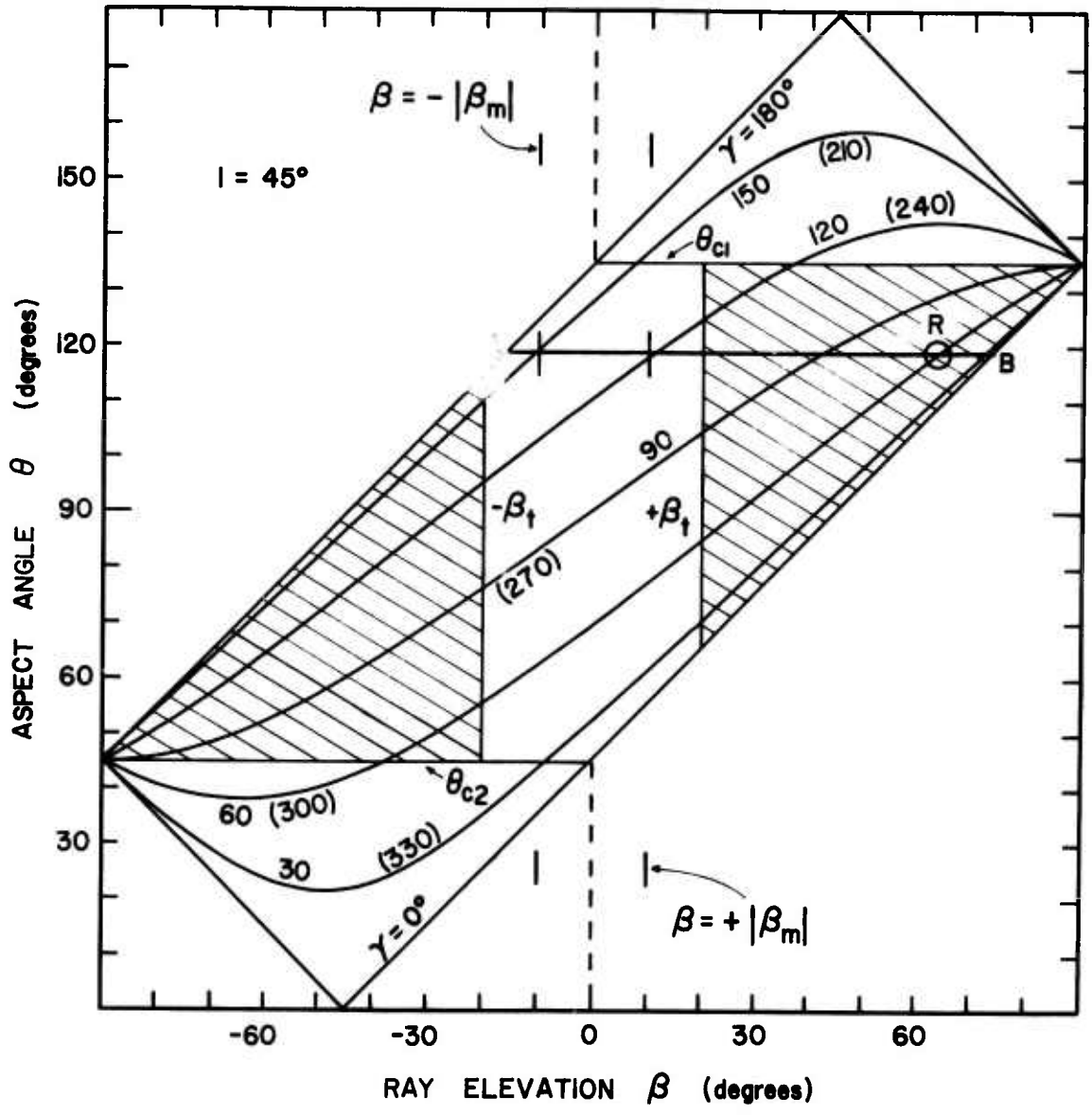

Fig. 3.4 The aspect-elevation diagram for a column of dip $I = 45°$. The ground-detached mode will always be launched from incident rays whose (β,γ) points lie within the hatched regions

into the $\theta = 119°$ cone, which in turn launches the $|\beta_m| = 10°$ ducted mode into the two azimuth sectors $121° \leq \gamma \leq 149°$ and $211° \leq \gamma \leq 239°$.

It is possible to delimit the regions within which the illuminating ray (represented by the point R) must lie in order to generate <u>any</u> ducted mode. This limiting case is defined by letting $|\beta_m| \to 0$, and the associated θ boundaries (labeled θ_{c1} and θ_{c2} on Figure 3.4)

are defined by the intersections of the $\gamma = 0, 180°$ loci with the $\beta = 0$ line. Additional boundaries result from the fact that rays from a ground-based transmitter must at any height satisfy $|\beta_R| \geq |\beta_t|$, where β_t is the elevation of the ray launched tangent to the earth's surface. Since all elevated ducts must lie below the reflection point (if any) of this tangential ray, it follows from the above inequality and Bouguer's rule that $|\beta_R| \geq |\beta_t| \geq |\beta_m|$. A realistic absolute upper limit for $|\beta_t|$ is 19.8°, which is the elevation of a straight tangential ray at the 400 km altitude (a reasonable maximum height for the F layer peak). The vertical lines representing this limit are labeled "$+\beta_t$" and "$-\beta_t$" on Figure 3.4. The hatched regions lying within the aspect-elevation loci rectangles and bounded by $\theta = \theta_{c1}$, $\beta = +\beta_t$; and $\theta = \theta_{c2}$, $\beta = -\beta_t$ therefore represent the domain of the combinations (β,γ) for incident rays from which the ducted mode can be launched via scattering from the column of dip angle I.

Conversely, the ducted mode may be launched whenever such regions exist on the diagram for the given value of I. Figure 3.5 shows the aspect-elevation diagrams for the limiting cases of $I = 0°$ and $I = 90°$. It is seen that these regions can occupy nearly the entirety of the $I = 0°$ plot, while none exist in the $I = 90°$ locus. Thus a horizontal column will always afford a mode-conversion mechanism, but a vertical one never can. Such regions can be found on all diagrams for which $0° \leq I < 90°$, given sufficiently small $|\beta_m|$ and $|\beta_t|$. Consequently, nearly all reflector orientations offer a ground-hop to ducted mode conversion mechanism.

3.4.2 Analytical formulation

Aspect-elevation diagram shows that the detached mode is launched into two azimuth sectors symmetrically placed about $\gamma = 0$. Figure 3.6 shows this event in the $0'$ spherical coordinate system, where the small circle corresponding to the incident ray R_1 crosses the duct zone boundaries at R_a, R_b, R_c, and R_d. It is desired to find the boundaries of these azimuth sectors.

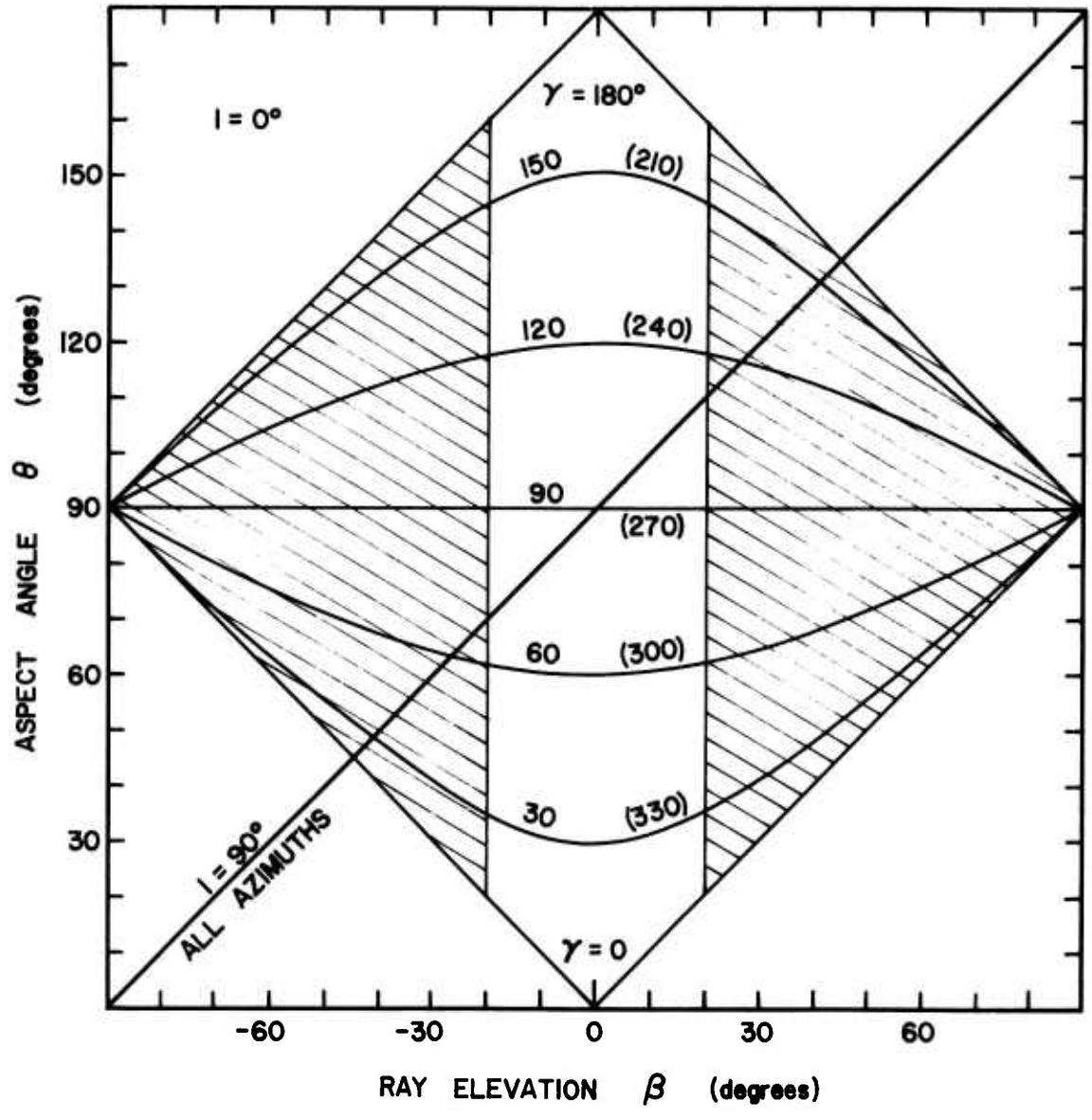

Fig. 3.5 The aspect-elevation diagrams for the limiting cases of $I = 0°$ and $I = 90°$.

Applying the law of cosines to the triangle VCR_a gives

$$\cos \theta = \cos \beta_m \cos I \cos \gamma_a - \sin \beta_m \sin I \qquad (3.8)$$

Substituting θ as given by (3.7) and rearranging yields

$$\cos \gamma_a = \frac{\cos \beta \cos I \cos \gamma + (\sin \beta - \sin |\beta_m|) \sin I}{\cos \beta_m \cos I} \qquad (3.9)$$

or, since $I = 90°$ is of no interest and therefore $\cos I \neq 0$,

$$\cos \gamma_a = \frac{\cos \beta \cos \gamma - \tan I \, (\sin \beta - \sin |\beta_m|)}{\cos \beta_m} \tag{3.10}$$

Applying this same development to the triangle VCR_b gives

$$\cos \gamma_b = \frac{\cos \beta \cos \gamma - \tan I \, (\sin \beta + \sin |\beta_m|)}{\cos \beta_m} \tag{3.11}$$

Identical expressions are obtained for γ_c and γ_d, respectively, showing that $\gamma_c = -\gamma_a$ and $\gamma_d = -\gamma_b$, thus establishing analytically the symmetry of the launching process about the geocentric plane containing the reflecting column.

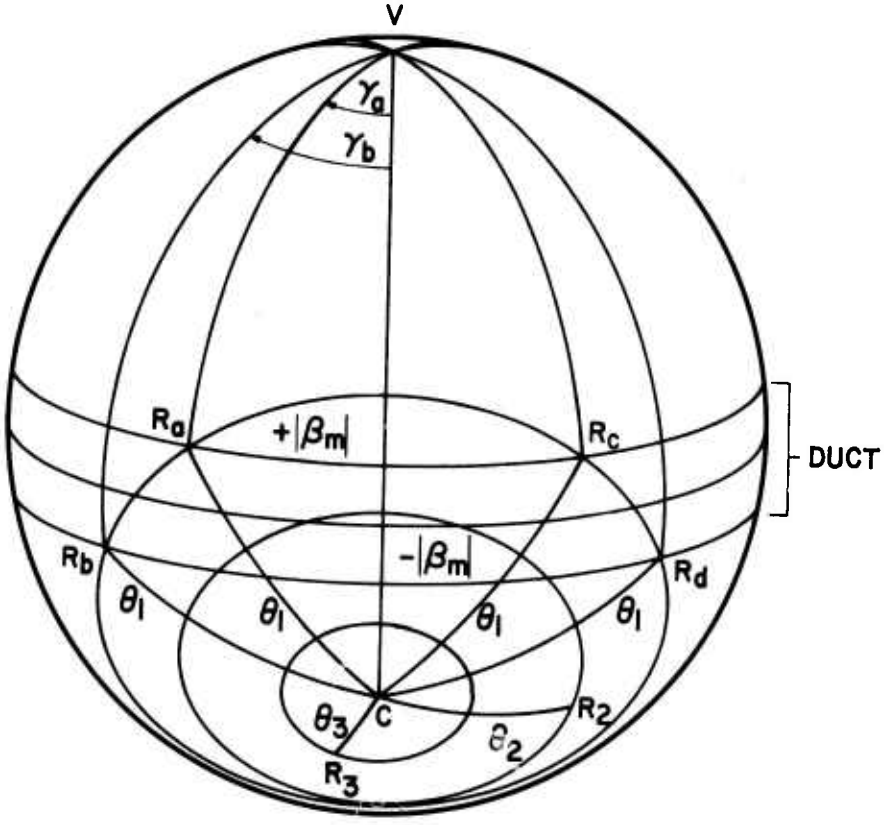

Fig. 3.6 The geometrical formulation used to determine the limits of azimuthal sectors into which the ground-detached mode is launched. Cones of scattered radio energy are represented by the small circles with the common pole C.

The two sectors merge into a single one, centered about this plane, when $|\cos \gamma_a| \geq 1$. In this case, the reflection cone does not fill the total angular width of the duct, as illustrated by the circle of radius θ_2 on Figure 3.6. Continuing this progression leads to the small circle of radius θ_3, which represents a reflection event which performs no mode conversion. In this case, (3.11) gives $|\cos \gamma_b| > 1$. Thus, the expressions (3.10) and (3.11) may also be used to indicate whether the ray described by (β,γ) incident upon a column of dip angle I will couple energy into the detached mode in a given duct.

3.5 The Mode-Coupling Efficiency

The central question of this section is: given that an incident ray meets a reflecting column of dip I at the aspect θ, what fraction of the reflected energy is contained within a duct specified by $|\beta| \leq |\beta_m|$.

3.5.1 Formulation

Figure 3.7 shows the geometrical formulation of this problem in the $0'$ coordinate system. It is necessary for this purpose to introduce the angle ϕ, measured as shown, to provide a coordinate scale about the circumference of the small circle representing the reflection cone. Thus, letting $P(\phi)$ represent the distribution of the time-averaged reflected power about the circumference of the reflection cone, the conversion efficiency η is defined by

$$\eta = \frac{\int_{R_a}^{R_a'} P(\phi)d\phi + \int_{R_b'}^{R_b} P(\phi)d\phi}{\int_0^{2\pi} P(\phi)d\phi} \qquad (3.12)$$

where the integrals in the numerator are evaluated over the portions of the small circle for which $|\beta| \leq |\beta_m|$.

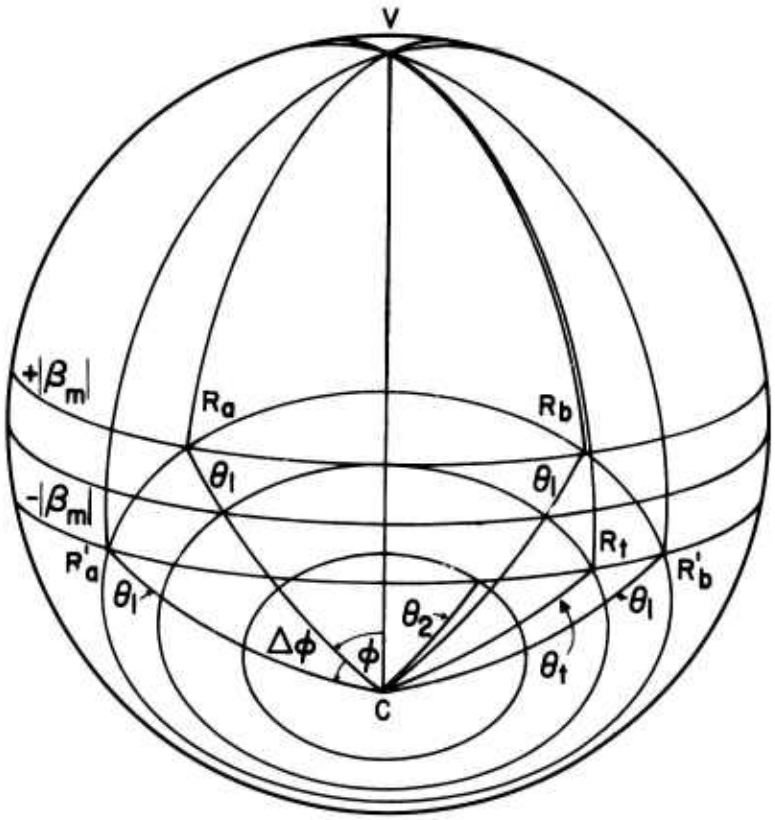

Fig. 3.7 The geometrical formulation of the mode-conversion efficiency computations.

The form of $P(\phi)$ is determined by the $\sin^2 \chi$ term in the reflected power distribution expression (3.4) where χ is the angle between the $\underset{\sim}{E}$ vector of the illuminating radiation field and the given direction of reflected energy propagation. However, since $\underset{\sim}{E}$ may in general have any orientation in the plane normal to the incident ray direction, χ and $P(\phi)$ can vary over a wide domain. A useful assumption is that the incident wave is circularly or randomly polarized in the normal plane, so that $P(\phi)$ represents an average over a definable range of χ. The author has attempted this approach, but the expressions obtained were very complex and (3.12) becomes prohibitively difficult to evaluate.

$\int_0^{2\pi}$ Consequently, a reasonable "priming" choice is $P(\phi) = 1$, so that $P(\phi)\, d\phi = 2\pi$. Equation (3.12) thus becomes

$$\eta = \frac{2\Delta\phi}{2\pi} = \frac{\Delta\phi}{\pi} \tag{3.13}$$

and the coupling efficiency is therefore equal to the fraction of the small circle circumference contained within the 0° equatorial zone defined by $|\beta| \leq |\beta_m|$ on Figure 3.7.

After experimentation with various formats, the most useful display of the efficiency data was determined to be a plot of the loci of constant η in θ, $|\beta_m|$ coordinates. Such diagrams are presented for representative values of I in Figure 3.8. To interpret these charts it is necessary to have an understanding of their underlying physical principles; hence, their discussion will be prefaced by a presentation of their physical and mathematical formulation.

The mode-coupling events fall into two categories requiring separate treatment. In the first of these, illustrated by the circle of radius θ_1 in Figure 3.7, the portion of the reflection cone circumference represented by a given $\Delta\phi$ (where $\Delta\phi = \pi\eta$) completely fills a symmetrical (about $\beta = 0$) equatorial zone. The second case occurs at a smaller value of θ, where the circumferential segment defined by the same $\Delta\phi$ cannot fill a symmetric duct zone. This condition is illustrated by the small circle of radius θ_2.

Case I is analyzed using the triangles VCR_a and VCR_a'. Given I and θ_1, it is desired to find the boundaries $\pm|\beta_m|$ of the symmetrical zone containing the small circle arc $\Delta\phi$. Applying the law of cosines to VCR_a and VCR_a' yields, respectively

$$\sin |\beta_m| = \sin \theta_1 \cos I \cos \phi - \cos \theta_1 \sin I \tag{3.14}$$

$$-\sin |\beta_m| = \sin \theta_1 \cos I \cos (\phi+\Delta\phi) - \cos \theta_1 \sin I \tag{3.15}$$

Summing the above expressions gives

$$\sin \theta_1 \cos I \,[\cos \phi + \cos (\phi+\Delta\phi)] = 2 \cos \theta_1 \sin I \tag{3.16}$$

The sole unknown quantity in (3.16) is ϕ. Hence, after solving this equation for $\cos \phi$, the required $|\beta_m|$ can be obtained from (3.14). Therefore, expanding the $\cos (\phi + \Delta\phi)$ term in (3.16) and rearranging gives

$$([1 + \cos \Delta\phi] \cos \phi - \sin \Delta\phi \sin \phi) \tan \theta_1 = 2 \tan I \qquad (3.17)$$

provided that $\theta_1 \neq 90°$, $I \neq 90°$.* This may be put in the form

$$A \cos \phi + B \sin \phi - C = 0 \qquad (3.18)$$

Since, for the triangles considered, $0 \leq \phi \leq 180°$, $\sin \phi \geq 0$, and

$$A \cos \phi + B (1 - \cos^2 \phi)^{\frac{1}{2}} - C = 0 \qquad (3.19)$$

This equation may be solved by two methods. In the first, (3.19) is rearranged, squared, and the quadratic formula applied to yield

$$\cos \phi = \frac{AC \pm [B^2 \cdot (A^2 + B^2 - C^2)]^{\frac{1}{2}}}{A^2 + B^2} \qquad (3.20)$$

However, this procedure always yields one extraneous root, which must be eliminated by testing both solutions in (3.19). An alternative scheme, more suitable for a computer, is to solve numerically the fundamental expression (3.19), using the Newton-Raphson iteration method [Henrici, 1964, p. 78]. This technique approximates the solution x to the function $f(x) = 0$ by applying recursively the relations

$$y = x - \frac{f(x)}{f'(x)} \qquad (3.21a)$$

$$x = y \qquad (3.21b)$$

until the absolute value of the difference between two successive approximations is less than some specified error bound. Therefore, letting $x = \cos \phi$, the Newton-Raphson formulation of (3.19) is

---

* These conditions are not unduly restrictive in practice, since $I = 90°$ provides no mode coupling, and the case $\theta_1 = 90°$ can be approached as a limit.

$$y = \frac{C\,(I - x^2)^{\frac{1}{2}} - B}{A\,(1 - x^2)^{\frac{1}{2}} - Bx} \tag{3.22a}$$

$$x = y \tag{3.22b}$$

This latter method was used to compute the "symmetric duct" portions of the loci of constant η on Figure 3.8. The error bound was fixed at 10^{-6}.

The above analysis applies also to the triangles VCR_b and VCR_b' which are the mirror images about the arc VC of the triangles considered above. The final value of $|\beta_m|$ is therefore unchanged when $-\phi$ and $-\Delta\phi$ are substituted for ϕ and $\Delta\phi$ in equations (3.14) through (3.19).

Case II is analyzed using the triangle VCR_b. In this instance, $\phi = \Delta\phi$, and the law of cosines gives

$$\sin |\beta_m| = \sin I \cos \phi_2 - \cos I \sin \phi_2 \cos \Delta\phi \tag{3.23}$$

which contains only known quantities on the right hand side, and therefore yields the desired $|\beta_m|$ immediately.

The transition between the two regimes occurs at $\theta = \theta_t = I + |\beta_m|$, as shown in Figure 3.7. The value of θ_t corresponding to given values of I and $\Delta\phi$ may be determined by applying the law of cosines to the triangle VCR_t, which gives

$$\sin |\beta_m| = \sin I \cos \theta_t - \cos I \sin \theta_t \cos \Delta\phi \tag{3.24}$$

Substituting $\theta_t = I + |\beta_m|$ and rearranging yields

$$\tan |\beta_m| = \frac{\sin I \cos I\,(1 - \cos \Delta\theta)}{2 - \cos^2 I\,(1 - \cos \Delta\theta)} \tag{3.25}$$

from which θ_t follows immediately.

It may be shown, by applying the foregoing development to the "hidden" side of the unit sphere in Figure 3.7, that the geometric conditions treated above are symmetric about $\theta = 90°$. Therefore, the contours on Figure 3.8 are also symmetric about this value.

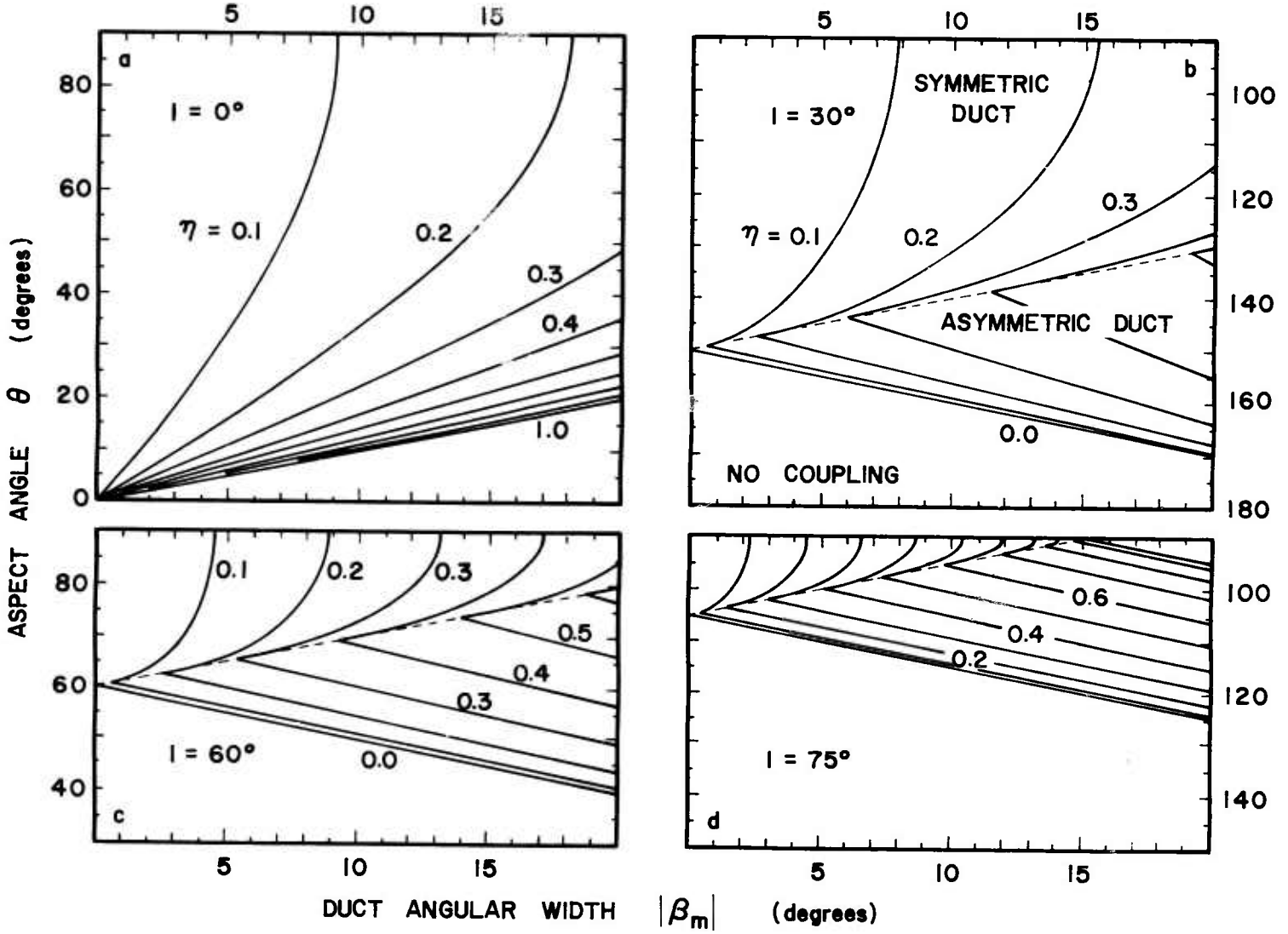

Fig. 3.8. The mode-conversion efficiency as a function of the angular duct width $|\beta_m|$ for the indicated values of column dip orientation I.

3.5.2 Results and discussion

The coupling efficiency diagrams in Figure 3.8 may be viewed as contour maps of the "efficiency terrain" for each value of I represented. Following a vertical line of constant $|\beta_m|$ through increasing θ, η is seen to rise abruptly from the "no-coupling" zone as the $\eta = 0$ line is crossed and increases to a maximum at the ridge whose peak (broken line) corresponds to the line $\theta = \theta_t = I + |\beta_m|$. This ridge defines the transition from the case II "asymmetric coupling" regime to the "symmetric duct" (case I) region. (In the $I = 0°$ case (Figure 3.8a), this rise forms a cliff since, for a column reflector in the equatorial plane of the unit sphere, the small circle of scattered energy is entirely symmetric in elevation, and therefore case II does not exist.) As θ increases beyond θ_t into the "symmetric duct" region, a shallow valley is encountered with its floor at $\theta = 90°$. The symmetry of the terrain about this floor is indicated by the auxiliary scale for $90° \leq \theta \leq 180°$.

The coupling efficiency increases as the angular width of the duct increases. The rate of this increase is not uniform, and diminishes at the higher values of $|\beta_m|$. In general, greater coupling efficiencies are attainable at the larger values of the dip angle I. However, the very highest coupling efficiencies are obtained from incident rays which are almost propagating within the duct to begin with; and $\eta = 1.0$ is meaningless, as it represents no actual mode conversion. Reasonably large values of η are realistically attainable, nevertheless; Figure 3.8d indicates that 50% of the scattered signal enters the $|\beta_m| = 10°$ duct when $I = 75°$, $\theta = 85°$.

For a given angular duct width $|\beta_m|$, the optimum coupling efficiency occurs at the transitional aspect values $\theta_t = I + |\beta_m|$ and $\theta'_t = 180° - (I + |\beta_m|)$. As indicated by the contour spacing, this maximum of η is quite sharp, and small departures of θ from this optimum value reduce the coupling efficiency considerably.

Consequently, to maintain optimum coupling efficiency, the aspect angle must be tightly controlled. The potentially highly variable effects of ionospheric refraction upon the propagation direction of the illuminating signal must therefore be minimized, which may be done by

locating the transmitter nearly beneath the intended cylindrical reflector and operating near the highest possible ducted frequency. It is likewise desirable to use a reflector of predictable and stable orientation. Field-aligned ionization irregularities are thus preferable to meteor trails and, as will be demonstrated in Chapter 5, they may be created artificially so that their positioning is also controllable. On the other hand, the optimum value of aspect depends strongly upon $|\beta_m|$ which, being a function of the ionospheric ionization profile, is time-variant and essentially unpredictable. (It is measurable, however, using a vertical-incidence sounder in conjunction with the overlay techniques of the previous chapter.)

It is therefore impractical to operate at maximum mode-coupling efficiency. The best one can hope for is to operate at a reasonably high η which is relatively invariant with $|\beta_m|$. Figure 3.8 shows that this desideratum is best approximated in the symmetric duct region near normal aspect ($\theta = 90°$). Thus, the optimum mode conversion scheme is to illuminate a nearly vertical column at an aspect approximately normal to its axis. This is incompatible with the desire to maintain a nearly invariant aspect, however, since to achieve the former conditions requires an obliquely propagating illuminating ray, which is vulnerable to refractive effects. (On the other hand, there is some flexibility here, as η is nearly independent of aspect near $\theta = 90°$.)

Thus, the following compromise options are indicated: a) To obtain a moderate but relatively stable mode conversion efficiency using geomagnetically-aligned reflectors, place the ground terminal in the middle geomagnetic dip latitudes; b) Operate in the higher latitudes for greater maximum efficiency if some variation of the coupling efficiency is acceptable. Considering the marked increase in η in the vicinity of $|\beta_m| = 5°$ near normal aspect as I increases from 60° to 75°, and the near invariance of η with θ in this neighborhood, the latter course seems preferable.

3.6 Summary

Using a ray-theory approach to the scattering of radio signals by cylindrical ionization irregularities in the ionosphere, the scattering geometry was formulated in a spherical trigonometric coordinate

system to provide a basis for analyzing the ground-hop to ground-detached propagation mode coupling properties of these irregularities. It was shown that, provided the scatterer was located within a duct of sufficient angular width, mode coupling was possible with all reflector orientations except the vertical. This was done via a graphical analysis technique, which also served to indicate which incident ray and reflector orientations could produce the desired coupling. An analytic method was also developed to ascertain both whether mode coupling would occur for given ray and reflector orientations, and, if so, the boundaries of the azimuthal sectors into which the detached mode was launched. It was indicated that these sectors are symmetric about the plane containing the scattering column and the center of the earth.

The mode-coupling efficiency was examined and found to be reasonable, with 50% of the scattered energy being injected into the elevated duct under certain realizable conditions. It was determined that the requisites for optimum coupling efficiency were very strict and practically impossible to maintain under actual operating conditions; the best compromise was found to consist of transmitting at the highest possible ionospherically propagating frequency from a location in the high geomagnetic dip latitudes, using field-aligned irregularities to effect the mode conversion.

4. BISTATIC RADAR ECHOES AT PREDICTABLE ASPECT ANGLE FROM COLUMNAR SCATTERERS IN THE REFRACTING IONOSPHERE

4.1 The Nature of the Bistatic Radar Problem

Numerous radar sounding studies of the geomagnetic-field-aligned columnar ionization density irregularities associated with auroral activity and certain spread-F ionospheric disturbances have been carried out in the past three decades [e.g., Herlofson, 1947; Chapman, 1952; Booker et al., 1955; Peterson et al., 1955; Dyce, 1955; Booker, 1956; Bates, 1959, 1960, 1961, 1971; Leadabrand and Peterson, 1958; Calvert and Cohen, 1961; Dearden, 1962, 1969a,b; Weaver, 1965; Unwin, 1966; Bates and Albee, 1969, 1970; Au and Hower, 1970; Millman, 1974; Basu et al., 1974]. Mainly for reasons of economy, most of these studies have employed monostatic radar configurations; that is, the transmitter and the receiver were situated at the same location. However, this radar geometry has an important additional property. As is well known, echo signals in a monostatic radar system usually travel to the target and return along the same propagation path, so that an echo will originate only from reflecting surfaces oriented normal to the direction of the incident ray. If the target is a reflecting column, monostatic radar echoes will thus occur only if the incident raypath meets the column axis at normal aspect, i.e., $\theta = 90°$.

This property has been exploited in the studies cited above, both to predict the directions from which monostatic radar echoes from field-aligned columns might be detected at a given sounding location and, conversely, to assess the field-aligned nature of observed echoes. The existence of a predetermined echo aspect angle greatly facilitates the echo location process when the effects of ionospheric refraction upon the propagation paths of the radar signals must be accounted for, since it is then necessary only to trace these raypaths and to determine if and where they meet the postulated field-aligned columns at normal aspect.

However, owing to the recent development of the high resolution, high signal-to-noise, sweep frequency continuous wave (SFCW) sounding technique, whose continuously-operating transmitter requires that the

receiver be physically separated from the transmitter, the bistatic radar configuration has gained new prominence. On the other hand, the task of locating bistatic radar echoes from field-aligned columns is generally quite formidable. The aspect conditions for a bistatic echo are very general; an echo will occur whenever the reflection cone from an incident transmitter ray contains a raypath to the receiver. The aspect angle at which the echo occurs may therefore range from 0° to 180°. In the simplest case of straight-line raypaths, the value of this angle is a function of the relative positions of the sounder terminals and the target, as well as of the orientation of the reflecting column. To determine this value and locate the echo origin points is extremely difficult. When ionospheric refraction effects must be considered, the echo origin points and the associated echo aspect angle values depend also upon the radar frequency and the time-varying state of the ionosphere. While useful approximate treatments of the no-refraction case have been devised [Fricker et al., 1957; Collins and Forsyth, 1959], no generalized echo-location study including the refractive effects has been done. In general, to locate the origin points of bistatic echoes requires that a detailed search be conducted to locate the points at which the raypaths from both the transmitter and receiver sites meet upon a reflecting column at equal aspect angles. This is a very laborious process.

4.2 Bistatic Radar Echoes at Predictable Aspect Angle

It is the purpose of this section to show that, under certain conditions, bistatic radar echoes may originate from columnar scatterers at a predetermined aspect angle, thereby permitting the direct location of these echoes in the same manner as in the monostatic radar geometry.

4.2.1 Formulation

It is necessary to examine the geometry of the general bistatic reflection process. A convenient formulation is obtained by representing both the illuminating (t) and the "received" (r) radiation fields by rays incident upon the reflector, as shown in the inset of Figure 4.1. In this case, the condition for a specular echo is

$$\theta_r = 180° - \theta_t \tag{4.1}$$

or, equivalently

$$\cos \theta_r = - \cos \theta_t \tag{4.2}$$

Using equation (3.6), this may be expressed

$$\cos \beta_r \cos \gamma_r \cos I - \sin \beta_r \sin I = \sin \beta_t \sin I - \cos \beta_t \cos \gamma_t \cos I \tag{4.3}$$

It is instructive to treat the problem graphically, plotting θ_r and θ_t as a function of β_r and β_t for representative values of the parameters γ_r and γ_t. Figure 4.1 shows this graph constructed for $I = 45°$, with β_r and β_t plotted on the same scale, but with the θ_r scale folded about $\theta = 90°$ with respect to the θ_t scale. This diagram is used in much the same manner as those in the previous chapter, except that, having entered the t curve family at β_t, γ_t, the horizontal line corresponding to the resulting θ_t is followed to the r curve group, where its intersections with these loci define the cone of reflected rays. For example, if the transmitter ray arrives at the reflector at $\gamma_t = 120°$, $\beta_t = 40°$, the line $R_t R_r$ shows that a specular echo will be received at, among others, a station from which a ray would arrive at $\gamma_r = 30°$, $\beta_r = -9°$.

4.2.2 Analysis and discussion

Of particular interest are the intersections of the curves of one group with those of the other, which signify that the associated reflections occur at a common echo ray elevation. Examining such diagrams drawn for representative values of I in the interval $0° < I \leq 90°$ establishes that the loci representing a given γ_r, γ_t azimuth pair intersect only once,* so that this common elevation is unique for any combination of γ_r, γ_t, and I. Likewise, associated with this echo ray elevation β_e is a unique echo aspect θ_e. We shall adopt the convention that β_e and θ_e will refer to the ray from the transmitter.

---

* For $I = 0°$, the loci representing supplementary values of γ_t and γ_r coincide. This special case is therefore excluded from the following development.

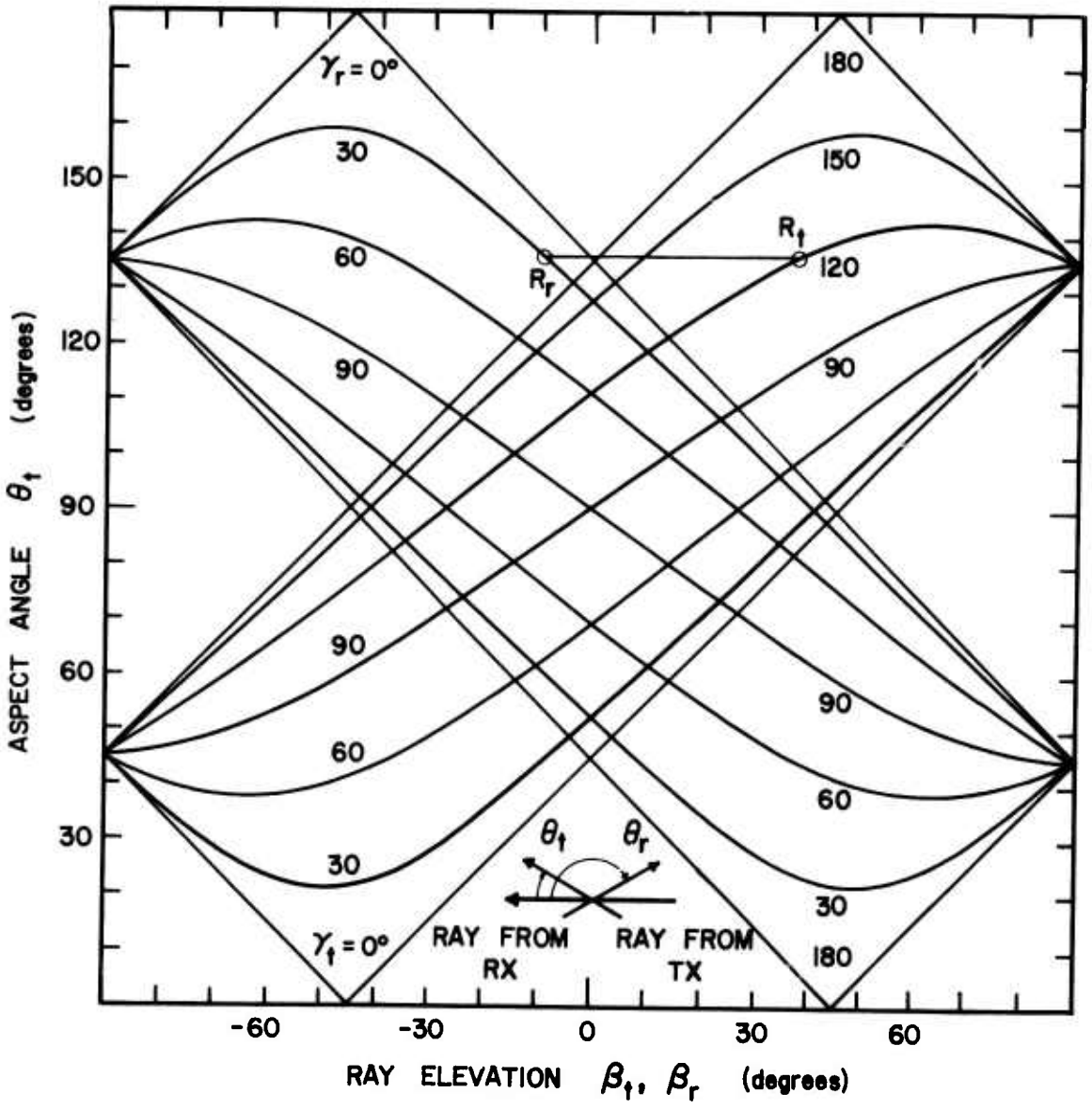

Fig. 4.1 The aspect-elevation diagram for solving the geometry of bistatic radar echoes from a reflecting column of orientation I = 45°. Both the illuminating (t) and the reflected (r) rays are represented as arriving at the point of reflection. θ_r and θ_t are defined as indicated in the inset.

Thus, whenever the rays from the transmitter and receiver sites meet upon a reflecting column from fixed azimuths and at equal elevations, specular echoes will occur between those, and only those, raypath pairs for which $\beta_r = \beta_t = \beta_e$; or equivalently, for which $\theta_r = \theta_t = \theta_e$. It is clear that rays reaching the same point via identically-shaped

trajectories (twin paths) must share a common elevation there. It therefore follows that, if a pair of radar terminals are located at the same ground range from the target, and if the propagation media along both terminal-to-target links are alike, the t, r raypath pairs launched at the same elevation angle will follow identical trajectories and arrive with the same elevations. Thus, under these conditions, the specular echoes will originate at an aspect which depends only upon the values of γ_r, γ_t, and I at the target. As indicated below, these values are often predeterminable, so that β_e and θ_e may then be predicted.

The identical propagation media condition is completely satisfied in a spherically symmetric, geoconcentric ionosphere, and approximately so in the presence of gentle tilts. Hence, the raypaths follow essentially great-circle routes. The equal-range constraint implies that the target should be located within the great-circle plane whose ground trace (the "line of targets") bisects the line joining the sounder terminals, as shown in Figure 4.2. When the scatterers are aligned with the geomagnetic field, I will be known within this plane, and the associated geomagnetic azimuths γ_t and γ_r may be readily computed. The echo ray elevation is then found by setting $\beta_r = \beta_t = \beta_e$ in equation (4.3) and solving. Thus

$$\tan \beta_e = \frac{1}{2} (\cos \gamma_t + \cos \gamma_r) \operatorname{ctn} I \qquad (4.4)$$

and

$$\cos \theta_e = \cos I \cos \beta_e \cos \gamma_t - \sin I \sin \beta_e \qquad (4.5)$$

Since the geomagnetic orientation changes slowly with height in the ionosphere (see Figure 5.3), γ_t, γ_r, and therefore β_e, θ_e, will be practically independent of altitude. As a result the echo aspect will also be nearly invariant with altitude along a given vertical line under twin-path conditions. It may therefore be computed once and for all as a function of range along the line of targets in certain bistatic radar configurations.

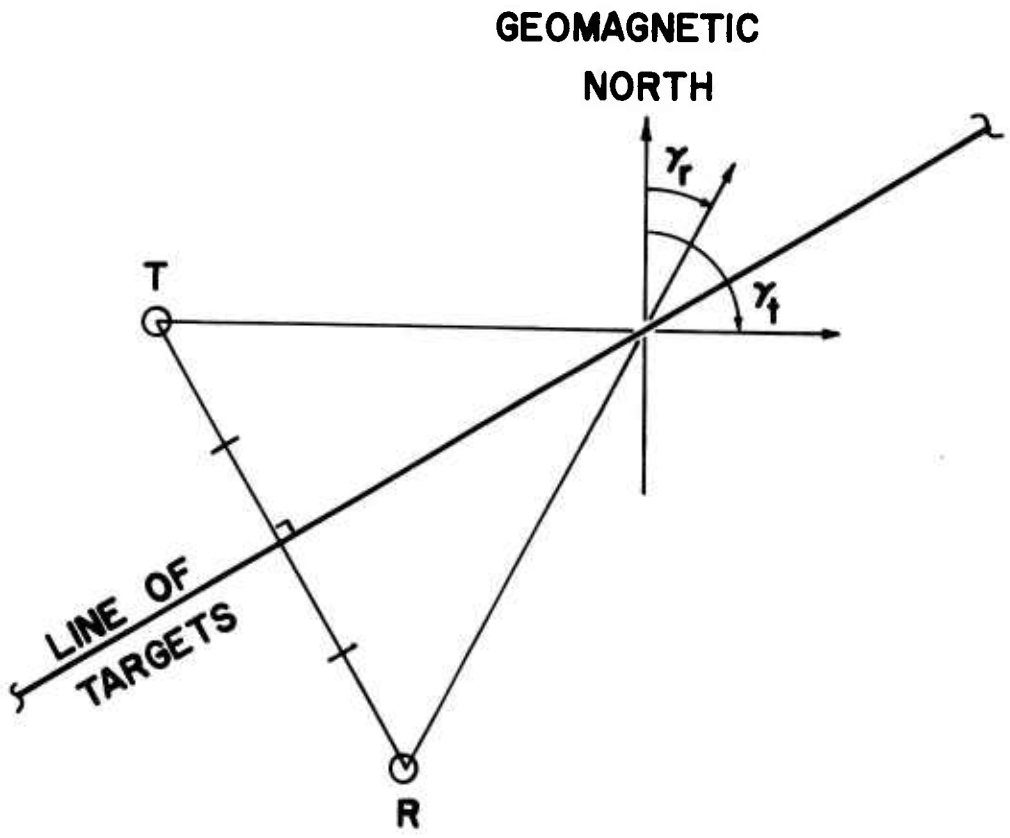

Fig. 4.2 The ground trace ("line of targets") of the great-circle plane which contains the origin points of twin-path echoes. The plane is the perpendicular bisector of the great circle joining the transmitter (t) and receiver (r) sites.

There is a caveat which must be observed when ionospheric refraction is significant. Since the ionosphere supports radio wave propagation via the upper and lower ray modes, rays from a given terminal may reach the same point via different paths. This can occur on both the t and the r segments of a bistatic radar configuration which satisfies the requisites given above. It is important to note that echoes can occur at predictable aspect only between t, r raypath pairs of the same mode, since only these fulfill the twin path requirement. Additional echoes may arise, however, between raypaths of different modes which happen to achieve specular incidence. Figure 4.3 illustrates how these cross-mode echoes may coexist with echoes of the same mode.

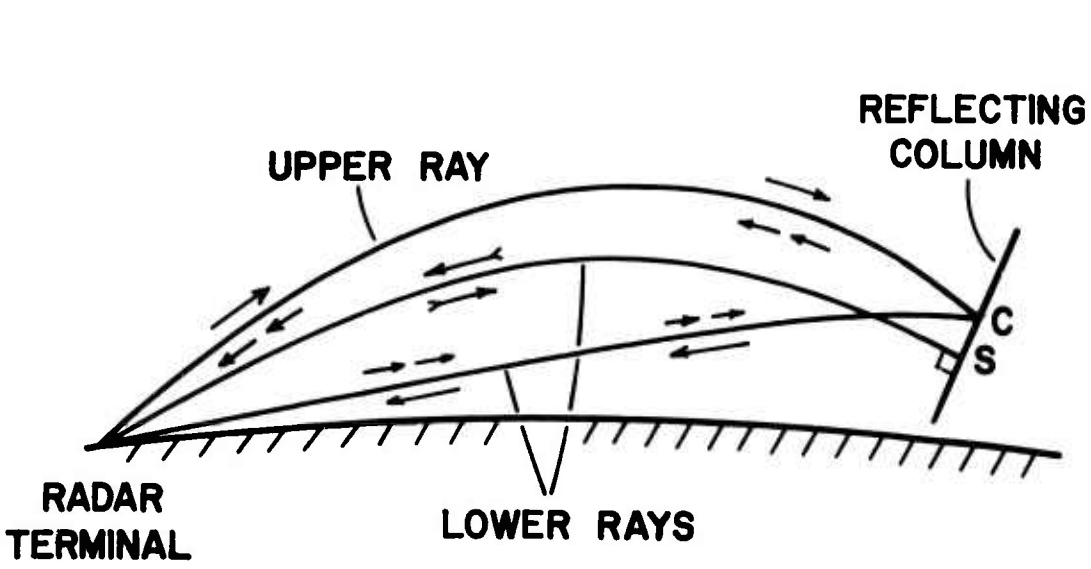

Fig. 4.3 Same-mode and cross-mode echoes coexisting in a monostatic radar configuration. Cross-mode echoes originate at C; same-mode echoes originate at S. The corresponding bistatic phenomenon is essentially similar.

Figure 4.1 shows that the possible twin-path values of β_e and θ_e are found within the "diamond" formed by the intersection of the t and r curve families. The ranges of β_e and θ_e may therefore be determined using (4.3) with the values of γ, β, and θ corresponding to the corners of this region. It thus follows that $0° \leq |\beta_e| \leq (90° - I)$ and $I \leq \theta_e \leq (180° - I)$.

It may be readily demonstrated that the twin-path mechanism includes the normal-aspect monostatic echo mechanism as a special case. Setting $\gamma_t = \gamma_r = \gamma$ into (4.4) gives

$$\tan \beta_e = \cos \gamma \tan I \tag{4.6}$$

and substituting this into (4.5) yields

$$\begin{aligned} \cos \theta_e &= \cos \beta_e (\cos I \cos \gamma - \sin I \cos \gamma \operatorname{ctn} I) \\ &\equiv 0 \end{aligned} \tag{4.7}$$

The aspect-elevation diagram of Figure 4.1 shows that the loci corresponding to equal values of γ_t, γ_r do indeed intersect at $\theta_e = 90°$.

A potentially useful effect in the sounding of field-aligned scattering columns arises from the refractive deviation of the radar raypaths. First, assume that the horizontal extent of the target region is very small in comparison to the range between the target and a radar terminal. (This might be achieved in practice through a combination of range gating and highly directive antennas.) A fan of raypaths launched in the vertical plane at a given radio frequency from this terminal will therefore arrive at the target with a continuous distribution of elevations $\beta(h)$ which is a function of altitude h only. (Owing to the dual-mode propagation phenomenon discussed above, this function may be double valued.)

If, now, the radar configuration satisfies the twin-path conditions, and if the $\beta(h)$ distribution contains the particular β_e, a specular echo will originate at the corresponding altitude. Changing the radar frequency will then, by altering the refractive influence of the ionospheric medium, shift the altitude at which $\beta = \beta_e$, and therefore permit the sounding of the field-aligned columns at different heights. In the absence of refraction, such an exploration requires the use of several radar terminals at appropriate geographic locations. The near-invariance of β_e and θ_e under twin-path conditions guarantees that the echoes will originate at a known, constant aspect, thus eliminating the variations in the target reflection coefficient due to aspect variations, and consequently simplifying the echo data analysis. These features have hitherto been available in the normal-aspect monostatic radar case; they have now been extended to certain bistatic configurations. As a result, useful radar techniques not readily implemented in a monostatic sounder, such as the SFCW waveform, may be used in the probing of geomagnetically-aligned columns.

Although it is necessary under these conditions to consider such complicating refraction-induced effects as focusing, Faraday rotation, possible cross-mode echoes, and a degree of uncertainty in the actual echo origin point, these factors arise in the medium, rather than in the target, and may be accounted for by modern computer raytracing and simulation techniques. Suitably placed vertical-incidence ionosondes might supply the required ionospheric data. An example of this is given in the following chapter.

5. A RAYTRACING SIMULATION AND INTERPRETATION OF SWEEP-FREQUENCY HF RADAR ECHOES FROM AN ARTIFICIALLY-INDUCED IONOSPHERIC DISTURBANCE

5.1 Introduction

The purpose of this chapter is to present a detailed raytracing simulation and interpretation of sweep-frequency HF backscatter ionogram signatures obtained from an artificially-generated ionospheric perturbation which was created by a special high-powered transmitting facility located near Platteville, Colorado. A further discussion of this modification experiment is given later in this chapter. The backscatter ionograms were recorded using an HF sweep-frequency sounder operated in central California by the Ionospheric Dynamics Laboratory of the Stanford Research Institute. This system is described later in the text, and the geographic locations of the sounder terminals and the Platteville irregularity are shown in Figure 5.1.

The radar signatures of interest were recorded during the California-Platteville round-the-world (RTW) propagation experiments which were discussed in Chapter 1. Initially, these echoes were monitored for diagnostic purposes, to verify that the transmitted signal was actually illuminating the perturbed region. It was expected (and subsequently confirmed) that the relatively dense midday ionosphere would refract the transmitted signal energy downward so that the bulk of it would pass beneath the irregularity, which was expected to be just below the F layer peak. The reception of the direct echo signature, which usually happened in the late afternoon, served to alert the experimenter to watch especially keenly for unusual RTW propagation events.

There were expectations that the perturbed region might contain individual ionization density irregularities elongated along the geomagnetic field lines. The backscatter signatures recorded in California became of primary interest when it was realized that their characteristic structure might be explained by a model which combined specular reflections from such field-aligned columns and the effects of the refracting ionospheric propagation medium. After a preliminary analysis supported this hypothesis, a full simulation of the sweep-frequency backscatter

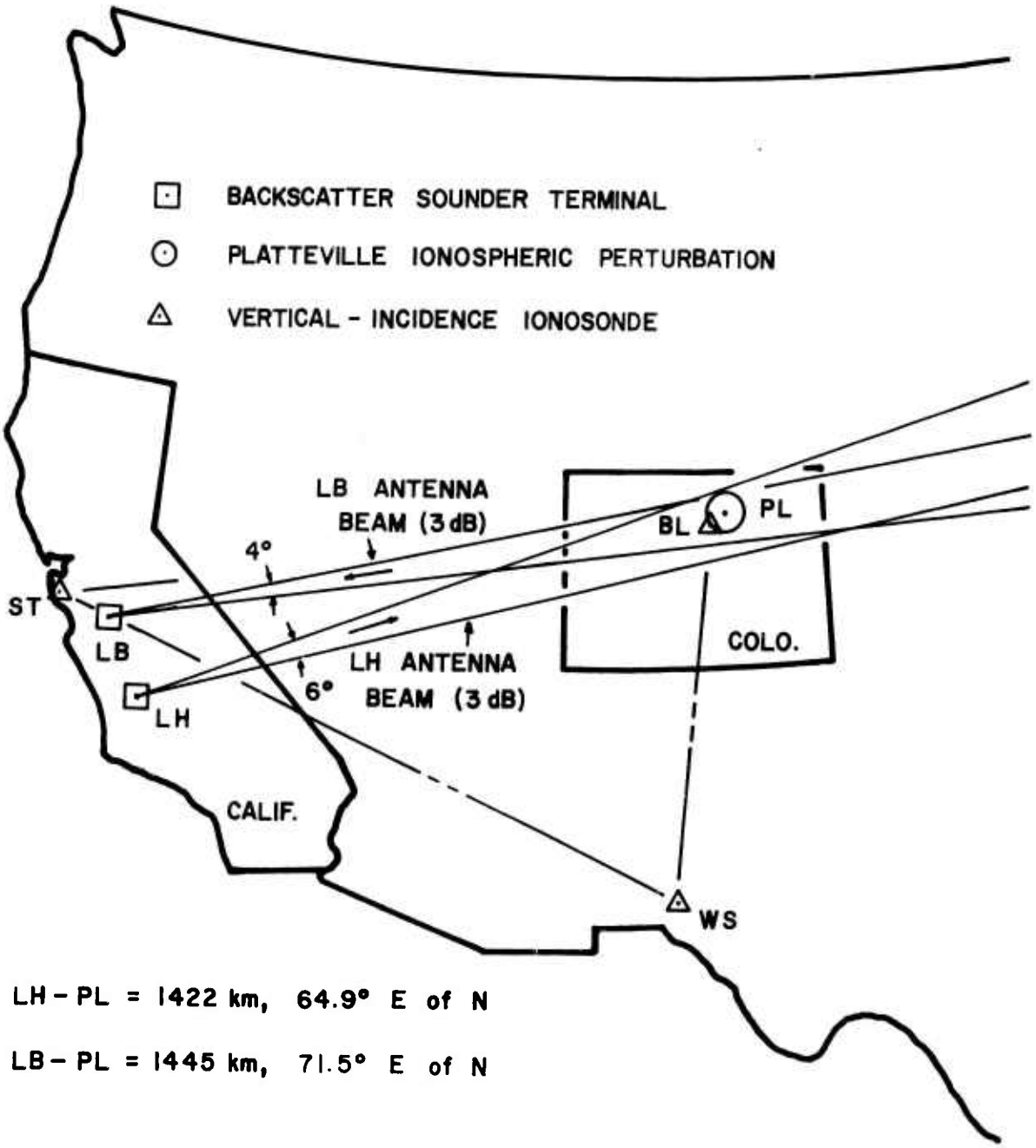

Fig. 5.1 The relative locations of the Platteville ionospheric irregularity (PL) and the central California HF SFCW sounder terminals. The transmitter is near Lost Hills (LH) and the receiver is near Los Banos (LB). Also shown are the vertical-incidence ionosonde stations at Stanford (ST), Boulder (BL) and White Sands (WS).

ionogram traces, using computer raytracing techniques, was undertaken to determine precisely how the propagation and reflection mechanisms interacted to produce the observed signature.

Once under way, it became apparent that this project offered a unique opportunity to examine, under relatively controlled conditions, the effects of the refracting ionospheric medium upon radar echoes received from field-aligned columnar reflectors such as those associated with the radio aurora. This topic will be discussed further in Section 5.4.2. A further motivation for the simulation was to establish the field-aligned nature of the reflection mechanism operating within the Platteville disturbance, as this had not been done at that time. In addition to its intrinsic scientific interest, this demonstration had an immediate practical interest in connection with the RTW ground-hop to ground-detached mode conversion experiment, since the application of the analysis developed in Chapter 3 to the California-Platteville radar geometry showed that an RTW signal launched into the ground-detached mode via a field-aligned reflecting column would propagate along paths considerably removed from the great circle joining the transmitter with the irregularity, and the highly-directive receiving antenna would have had to be steered accordingly.

In a more general application, a demonstration that field-aligned ionization columns could be generated and maintained on purpose, using ground-based facilities, would establish the potential to create a window to the ground-detached mode and thereby aid the practical exploitation of this propagation mode. This concept of coupling to the ground-detached mode via man-made ionospheric disturbances had been previously explored by Grossi [1970], who proposed using a high-powered transmitter to heat a small ionospheric region to induce a refractive inhomogeniety, which could then deflect the signal from a communications transmitter into the elevated duct. In a variation on this scheme, Gurevich [1971] proposed that a well-collimated beam from a sufficiently high powered communications transmitter might create its own refractive perturbation, producing an auto-coupling effect. However, since these theoretical studies were conducted before a large-scale experimental

effort was undertaken to modify the ionospheric parameters with intense radio signals, they did not include the largely-unexpected phenomena which were actually observed.

Among the possible kinds of columnar scatterers which may exist in the ionosphere and which might be used in mode-coupling applications, the artificially-induced type appears to offer an optimum combination of availability and directional stability. Stability is especially desirable, since the coupling process is quite directive in azimuth, and its efficiency is very sensitive to the aspect angle.

Meteor trails meet these criteria rather poorly. In the first place, the presence of a meteor in a given region of space at a given time is essentially a random event. Also, except for meteor showers having well-defined radiants, the orientation of a given trail is unpredictable; and the orientation of the shower meteor trails varies in a diurnal fashion. Finally, the initially straight trail is often rapidly distorted by wind shears, and its scattering ability quickly diminishes as its ionization is dispersed through diffusion.

The orientation of a field-aligned column is, on the other hand, intrinsically stable and predictable; radar scattering experiments have shown that it is the same as the local direction of the geomagnetic field [e.g., Watkins, 1970]. These columns are formed because, when a plasma is permeated by a magnetic field, the mobility of the ionized particles is restricted in directions normal to the magnetic flux lines by Lorentz forces. As a result, plasma density inhomogenieties in the ionosphere tend to become elongated in the direction of the local geomagnetic field. This tendency becomes more pronounced at the higher altitudes, where lower particle densities permit greater freedom of motion along the field lines. Such irregularities will behave as coherent line scatterers if their length greatly exceeds their width, which must in turn be small relative to the wavelength of the incident radiation [Booker, 1956]. The exact mechanism by which such individual columns, or collections of them develop is not yet completely understood; reviews of the various theories are given by Herman [1966]; Farley et al., [1970]; and Farley [1974]; further references are given by Perkins [1975].

Naturally-occurring field-aligned radio scatterers are not, however, consistently available worldwide. Radar soundings have established their presence in the auroral zone, where they often accompany visible auroral displays. There is similar evidence that they may exist in patches of the spread-F ionospheric disturbance, which occurs sporadically anywhere in the world [Herman, 1966].

5.2 The Experiment

5.2.1 The Platteville ionosphere modification experiment

The Platteville ionosphere modification facility, located at 40.18° N, 104.74° W, near Platteville, Colorado, consists basically of a means to radiate an intense (about 2 MW) radio signal into the overhead ionosphere. The radio frequency is chosen to be at or below the ionospheric critical frequency, so that the incident wave eventually encounters a zero of the refractive index, at which height it is reflected. At this happens the free ionospheric electrons are oscillating strongly in resonance with the incident signal, and a portion of their coherent motion is thermalized by collisions with the neutral particles comprising the bulk of the atmospheric gas. This effect, combined with a very intense incident radiation flux, can raise the local electron temperature significantly. These hot electrons then diffuse away from the heated volume along the lines of the geomagnetic field, producing a region of relative ionization depletion.

This simplified discussion provides useful qualitative insight into the ionospheric modification process. A more comprehensive analysis is beyond the scope of this work, and the actual mechanism is not yet completely understood. An historical overview of the artificial ionospheric modification effort is given by Utlaut and Cohen [1971], and the current state of theoretical understanding is discussed, and references given, by Meltz and Perkins [1974] and Perkins [1975].

The Platteville facility consists of ten 200 kW transmitters, each feeding an individual element of a large ring-array antenna, which in turn forms a vertically-directed beam of 16° nominal half-power width. The relative phases of the transmitter outputs can be adjusted to produce a right-circular or left-circular polarization to excite substantially either the O or the X magneto-ionic mode, respectively.

A prominent event associated with the operation of the modification facility is the appearance of a spread-F condition on the vertical-incidence sweep-frequency ionograms recorded in the vicinity of Platteville [Utlaut and Violette, 1973]. "Spread-F" is a generic term used to describe a diffuse or spread appearance of the F layer traces on such ionograms. In general, these events are classified either as range spreading, in which the horizontal portion of the trace is spread in the range dimension, or as frequency spreading, where the cusp of the trace is diffused and spread in the frequency dimension. The occurrences associated with the Platteville modification experiment are predominantly of the latter type; representative examples are shown in Figures 5.2 and 5.3.

Naturally-occurring spread-F is observed sporadically worldwide, with maxima of occurrence frequency in the auroral regions and in the vicinity of the geomagnetic equator. Evidence indicates that it results from the presence of ionization density irregularities of relatively small scale size (see a review of the subject by Herman [1966]). That these irregularities may include field-aligned columns has been demonstrated by Calvert and Cohen [1961] in the equatorial zone, and by Bates [1971] in the auroral region.

5.2.2 Sweep-frequency HF backscatter radar sounding of the perturbed ionospheric region

The radar sounding of the ionospheric disturbance was carried out using the HF sweep-frequency continuous-wave (SFCW) backscatter sounding facility operated in central California by the Ionospheric Dynamics Laboratory of the Stanford Research Institute. The locations of the sounder terminals and the Platteville target irregularity are shown on Figure 5.1.

This particular propagation geometry offered advantages in this experiment, facilitating both the identification of the echo signatures of interest on the backscatter ionograms and the process of simulating them. Since the mean ground distance of 1433 km from the sounder terminals to Platteville is about one-half of an F layer propagation hop, there was a distinct range separation between the echo from the elevated irregularity and the ground backscatter returns. Also, the vertical-

incidence ionograms required to construct the ionospheric model for the raytracing simulation were available from ionosondes at Boulder (BL), Stanford (ST), and White Sands (WS), which are denoted by the open triangles on Figure 5.1.

To prevent overloading the receiver by the direct signal from the transmitter, the sounding radar was bistatic, with an interstation spacing of 186 km. In combination with the overall propagation geometry, this configuration provided an opportunity to apply and to test the practical value of the twin-path echo concept developed in Chapter 4. The twin-path prerequisites were satisfied very closely by the central California-Platteville path, as the outgoing and returning propagation paths differed by only 23 km in ground range (relative difference = 1.6%), and were in sufficient proximity that the signals traversed essentially identical ionospheric media along each.

The transmitting facility was located near Lost Hills, California (LH), and consisted of a wide-aperture linear antenna array of vertical elements, which was fed by two 10 kW transmitters in tandem. This array formed a beam of nominal 6° half-power width at midband (18 MHz); this beam was phase-steerable in 4° steps between 58° and 122° true azimuth. The SFCW signal was generated by a linear frequency-sweep synthesizer which was in turn driven by an ultra-stable cesium frequency standard. This cesium standard also provided the accurate local clock necessary to coordinate operations with the receiving site.

The receiving terminal was located near Los Banos, California (LB). It employed a linear array of 2.55 km aperture aligned along the geographic meridian and comprised of 256 vertical elements spaced at 10 m intervals. This antenna formed a beam of half-power width of 0.73° at 10 MHz and 0.24° at 30 MHz, which could be phase-steered in 0.25° steps from 74° through 106° true azimuth. The array was subdivided into 8 subarrays of 32 elements, each of which could function as an independent array of beam-width 8 times that of the entire array. The present experiment employed one of these subarrays, with its steering circuits modified to direct its beam along the 72° bearing from Los Banos to Platteville. The receiving and processing system included a specially designed SFCW receiver, a 500 channel variable-bandwidth spectrum

analyzer, and a facsimile video unit to display the backscatter data as it was received. The receiver local oscillator frequencies, as well as all timing signals, were derived from a cesium standard synchronized with its counterpart at the transmitter.

The backscatter ionograms chosen for the simulation attempt were recorded on 5 and 6 January, 1972, and are presented in Figures 5.2 and 5.3, together with the simultaneous Boulder vertical ionograms showing the frequency-type spread-F condition characteristic of the presence of the Platteville irregularity. The signatures originating from this disturbance are labeled "PL echo". These records were selected from a set of similar data from experiments conducted in late 1971 and early 1972, both because they furnish a time sequence illustrating the typical evolution of the echo trace, and because they represent echo specimens under markedly different propagation conditions. The 5 January signatures typify the echo traces obtained under good propagation conditions; The 6 January signature is a unique example of an echo received under poor conditions.

The backscatter ionograms were generated using a frequency sweep rate of 250 kHz/sec, and were spectrum analyzed at a 10 Hz frequency resolution to give a propagation time (range) resolution of 40 μsec (6 km). Owing to the technical impossibility of maintaining perfect synchronism between the cesium clocks controlling the transmitter and receiver units, the absolute propagation times (ranges) noted in the figures may contain a common systematic error not exceeding 1 msec (150 km). Differential times (ranges) scaled from the records, however, are accurate to the characteristic 40 μsec (6 km) resolution limit.

Following the standard procedure in this sounding method, the receiver was operated in the automatic gain control mode to accommodate a wide range of backscatter return amplitudes and to prevent spurious responses due to overloading by strong returns. Consequently, much of the amplitude information in the Platteville echo was lost. However, tests of the facsimile video system have established that an approximately 15 dB rise in the signal amplitude will span the range of the recording paper from its response threshold to its fully darkened saturated condition Washburn, [1971]. Since certain of the echoes do

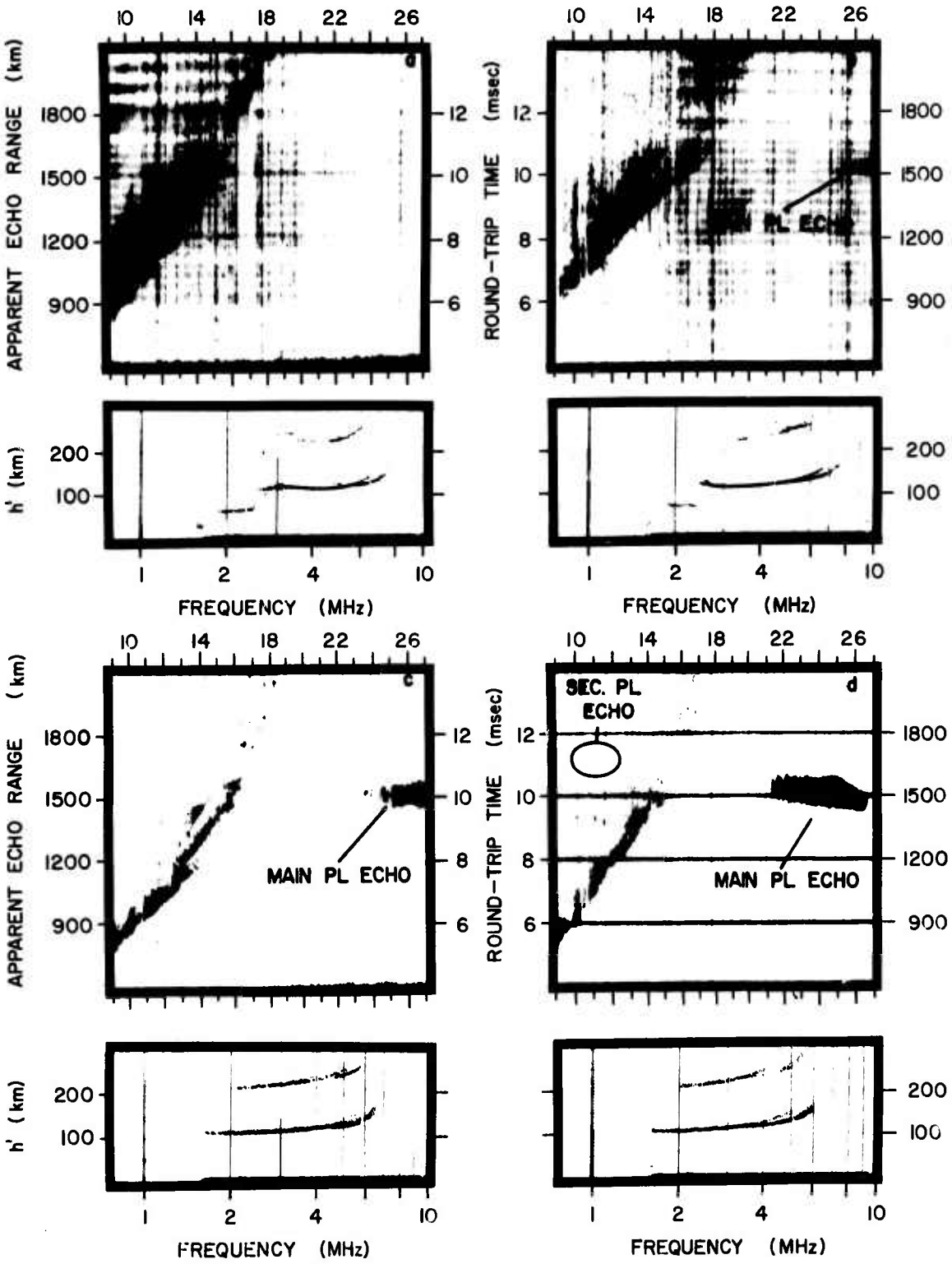

Fig. 5.2 The upper panel of each pair shows the backscatter ionogram recorded at LB; the lower panel shows the simultaneous BL vertical-incidence ionogram (h′ denotes virtual height of reflection). The times are (a) 1500 MST (Mountain Standard Time), (b) 1600 MST, (c) 1630 MST, (d) 1715 MST. All were recorded on 5 January 1972.

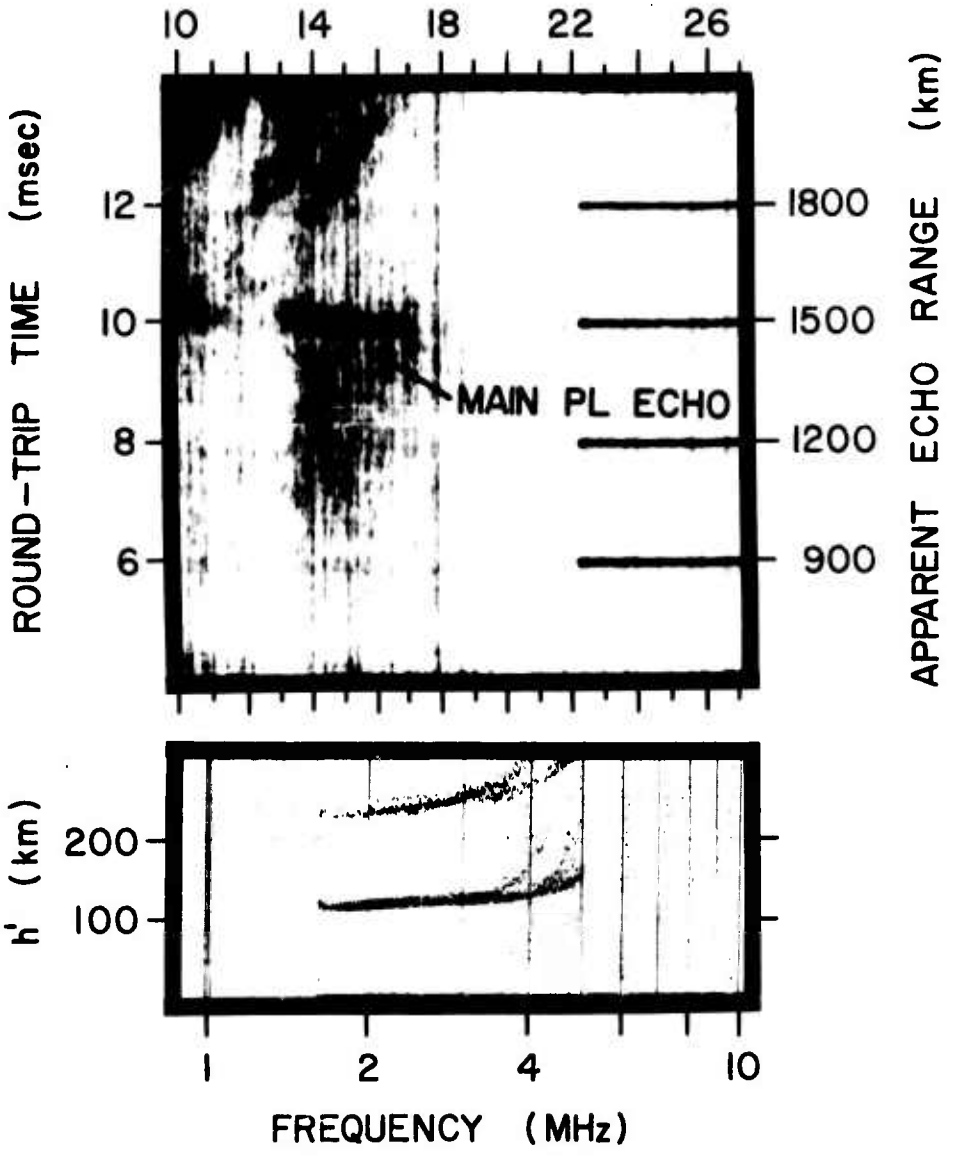

Fig. 5.3 The upper panel shows the backscatter ionogram recorded at LB; the lower panel shows the simultaneous BL vertical-incidence ionogram. 1845 MST, 6 January 1972.

saturate the display, their visibility (ratio of desired signal intensity to the background level) must be at least 15 dB.

The traces appearing in the backscatter ionograms of Figure 5.2 and 5.3 are interpreted as follows. The broad, irregular trace curving diagonally across each panel represents signal energy which has executed one hop through the ionosphere, backscattered from the earth, and returned to the receiver via the ionosphere. Additional echoes of this sort are represented by the blotches to the left of this band. The right edge of the diagonal trace defines the minimum propagation time characteristic of the ground backscattered signal at a given frequency, so that any echo whose apparent range is less than this must originate from a target located above the ground. Accordingly, the signatures labeled "main PL echo" represent reflections from an elevated target. Their nominal round-trip propagation time of 10 msec places this target at the general range of 1500 km from the sounder, which is acceptably near the 1433 km mean ground range to Platteville. The origin of these traces is confirmed by the fact that their presence correlates with the operation of the Platteville transmitter. The signature labeled "sec PL echo" on Figure 5.2d was also identified in this manner. This interesting trace is discussed further in Section 5.6.3.

A notable characteristic of these echoes is that they appear only within a limited range of radar frequencies. This feature is most clearly evident in the records of Figures 5.2d and 5.3. The signatures in Figure 5.2b,c are cut off at the 27 MHz upper limit of the frequency sweep. However, consideration of the time evolution of the echo, as represented by the upper panels in Figure 5.2, indicates that the frequency band occupied by the signature moves progressively downward as a whole at successively later times, so that an intrinsic extinction of the echo eventually appears at a frequency less than 27 MHz. Thus it is reasonable to believe that the signatures of Figure 5.2b,c would exhibit an intrinsic band-limited character had it been possible to extend the upper limit of the SFCW frequency sweep. The temporal evolution of the echo trace likewise suggests that an echo might have appeared had the upper frequency limit been extended in recording the backscatter ionogram of Figure 5.2a, which shows no PL echo signature, although the

associated BL vertical ionogram has a definite spread-F condition. As will be shown later, the temporal behavior of the signature is due to the diurnal variation of the ionospheric structure, while the existence of the intrinsic upper cutoff is a consequence of specular reflection from field-aligned ionized columns in the man-made irregularity.

5.3 The Nature of the Reflection Mechanism

A detailed scattering model of the irregularities responsible for the echoes shown in Figures 5.2 and 5.3 cannot be developed using only the information contained in the backscatter ionograms. Since the effective aperture of the receiving system was not calibrated when these records were obtained, the absolute strength of the echo signal could not be measured, and thus the scattering cross-section cannot be determined. It is possible, however, to determine the general nature of the scattering structures from the available data.

The probable scattering models are of two kinds: isotropic scattering and specular reflection from field-aligned columns. Reflection by large structures in the ionosphere, such as "steps" (see King [1970]) is included in the former category here since there is no a priori reason to assign any particular orientation to these structures. It will be shown in the following development that, while an isotropic scattering process can account for certain echo characteristics, a model invoking specular reflections from field-aligned ionized columns explains completely the observed echo structure.

The phenomena arising from ionospheric refraction effects may be explored using Figure 5.4, in which some representative raypaths have been plotted through a spherically-symmetric Chapman model ionospheric layer at selected multiples of the critical frequency. This model approximates the propagation characteristics of the actual F layer. The ray trajectories were computed using the "Mark 3" raytracing procedure of Croft [1969], as adapted by the author to an HP 9810 programmable calculator. Since the great-circle routes joining Platteville and the sounder terminals are close together and of nearly equal length, a single rayplot will serve for both the outgoing and the returning signals. The Platteville irregularity is presumed to be located near

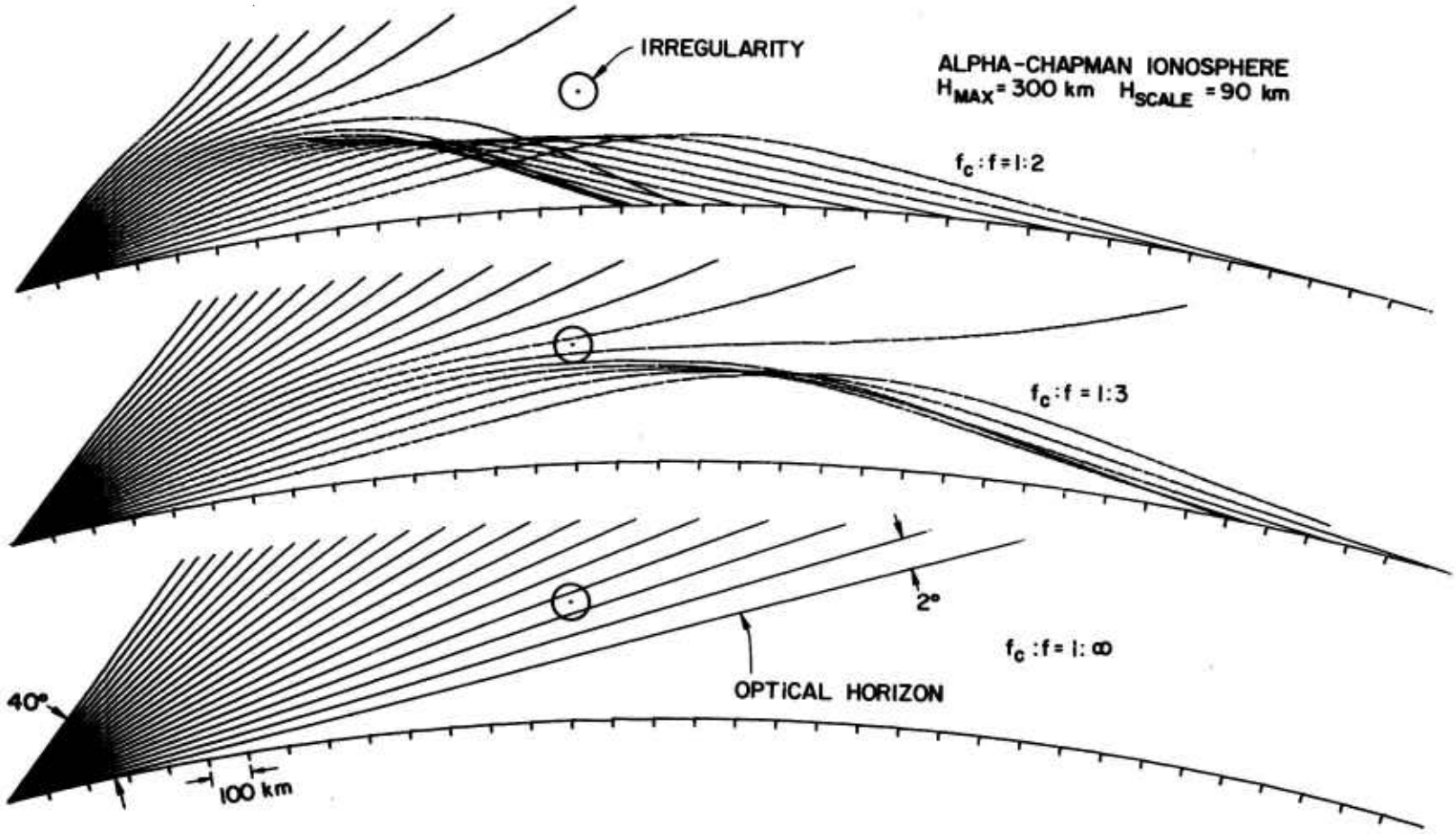

Fig. 5.4 The illumination of the Platteville irregularity by rays propagating from LH through a Chapman model ionosphere at multiples of 2, 3, and ∞ of the layer critical frequency.

the F layer peak (about 250 km altitude) directly above the heater transmitter, as signified by the open circles.

Each panel of Figure 5.4 shows the paths of a set of rays transmitted from a point at the lower left at 2° increments in elevation over the range 0°-40°. This uniform spacing allows an estimate of the relative power flux at any point in the medium. Following standard ray theory [Born and Wolf, 1970], each pair of raypaths form the boundaries of a flux tube channeling a certain fraction of the transmitted power. For the immediate purposes, it is assumed that each flux tube formed by adjacent raypaths leaving the transmitter carries the same power flux. Hence, wherever the raypaths do not touch each other, the local power density is in approximate inverse proportion to the raypath separation.

As a first approach, the target is supposed to contain a group of ionization density irregularities which scatter electromagnetic energy uniformly in all direction (isotropic scattering model). The upper panel in Figure 5.4 shows the irregularity to be weakly illuminated by a very defocused ray bundle at the lowest radar frequencies, while the center panel indicates a somewhat more intense illumination at medium frequencies. Extrapolating this trend indicates that the power flux illuminating the target, and hence the echo, becomes progressively weaker as the frequency decreases. Thus, the isotropic scattering model reproduces the low-frequency weakening and disappearance of the echo signal observed on the experimental records. However, this mechanism cannot account for the upper-frequency extinction of the echo, as the lower panel of Figure 5.4 indicates that the target remains well illuminated even in the limit of "infinite" radar frequency.

This cutoff is, however, the natural result of a scattering model based upon reflecting columns aligned with the geomagnetic field. In this case. the disturbance is assumed to contain a field of such columns of orientation $I = 68.09°$, $D = 12.83°$, as computed at the 250 km altitude over Platteville using the Jensen and Cain [1962] model of the geomagnetic field. Assuming, for the reasons indicated earlier, that the twin-path echo criteria are satisfied by the experimental geometry, the application of (4.4) and (4.5) yields an echo aspect angle of 88.8°, together with an echo ray elevation of 9.5°.

A twin-path specular field-aligned echo must originate from a transmitter ray which encounters the target at this echo ray elevation. However, an undeviated ray cannot arrive at the target with an elevation less than that of the straight-line ray launched tangent to the transmitter horizon. Since the elevation at Platteville of the Lost Hills optical horizon is 12.8°, to generate such an echo in this particular configuration it is necessary that the raypaths be deflected downward by ionospheric refraction. Because these refractive effects diminish as the radio frequency increases, there must exist an upper frequency limit beyond which the necessary ray orientation cannot be maintained, and a specular echo from field-aligned columns in the Platteville disturbance must therefore extinguish at some upper frequency limit.

Although the field-aligned scatter model does not of itself predict the echo dropout at the lowest sounding frequencies, this would still result from the defocusing effects discussed earlier. Thus, when displayed on the sweep-frequency backscatter ionogram format, a field-aligned echo signature would be expected to arise from the background as the frequency increases, persist over a band of frequencies, and then cease rather abruptly. This behavior matches that of the "main PL echo" signatures on Figures 5.2 and 5.3, and it is therefore proposed that these echoes are the result of a field-aligned specular reflection mechanism.

The progressive decline of the frequency range occupied by the echo of the records shown in Figure 5.2 may be attributed to propagation effects arising from the afternoon decay of the ionosphere. For illustration, it may be assumed that this decay consists of a proportional decline in ionization density occurring uniformly at all heights, so that the form of the layer is unchanged and radio wave propagation is governed chiefly by the ratio of the radio frequency to the ionospheric critical frequency. The rayplot sequence in Figure 5.4 indicates that the defocusing at the target at a given radar frequency lessens as the critical frequency falls. Consequently, the intensity of the low-frequency portion of the echo signature increases and crosses the system response threshold at successively lower frequencies. Meanwhile, the

upper cutoff frequency falls as the lessening refractive effect fails to maintain the ray orientation required to generate a specular echo at the higher frequencies.

5.4 Raytracing Simulation of the Echo Signatures

5.4.1 Purpose

The objective of the echo simulation undertaking was to reconstruct the sweep-frequency HF backscatter ionogram signatures of a field-aligned echo from the Platteville disturbance, as recorded by the central California sounder, taking realistic account of the ionospheric propagation conditions which existed at the time the actual signatures were observed. It was proposed to reproduce the actual signatures using this model, and thus to demonstrate that scattering from field-aligned structures was the predominant reflection mechanism operating in the Platteville irregularity. It was also desired to ascertain how the effects of ionospheric refraction interacted with this reflection mechanism to produce the observed echo. This latter point is of special interest in the radar probing of natural field-aligned irregularities, as such measurements in the HF band are strongly influenced by ionospheric refractive effects.

5.4.2 How this effort relates to previous studies

Attempts to understand the effects of ionospheric refraction upon the HF radar echoes obtained from natural field-aligned columns began shortly after the field-aligned nature of echoes from the auroral regions and associated spread-F disturbances was realized. A pioneering effort was that of Leadabrand and Peterson [1958], who applied approximate raytracing techniques in parabolic ionospheric models in an attempt to locate the normal-aspect reflection points of fixed-frequency HF auroral echoes observed at apparent ranges of 1400-4700 km north of Stanford, California. Other approximate methods of dealing with refractive effects in this context have been presented by Bates [1959], Vershinin [1962], Unwin [1966], and Bates and Albee [1969, 1970]. A detailed analysis was published by Dearden [1962], who plotted the spatial loci of normal aspect occurrence with respect to a dipole geomagnetic field for selected radar frequencies in the southern

hemisphere. Dearden pointed out that the refractive effects would cause field-aligned echoes to originate from two distinct altitudes at a given apparent range, for certain combinations of frequency and azimuth. Approximate raytracing techniques were employed to model schematically the sweep-frequency signatures of spread-F returns by Renau [1960], Calvert and Cohen [1961], and of aspect-sensitive auroral echoes by Bates [1965], in order to demonstrate how their respective observed signatures might have arisen through reflections from field-aligned structures embedded in a refracting ionosphere.

Other authors have employed full raytracing procedures on digital computers to conduct more refined studies of refractive effects. Dearden [1969a,b] considered ionospheric tilts and showed how the ground-detached propagation modes launched by them could enable strong normal-aspect field aligned echoes to originate at ranges of several thousands of kilometers from the radar site. These phenomena were treated in more detail by Hower and Makhijani [1969] and Au and Hower [1970], who undertook to locate the normal-aspect reflection points for HF fixed-frequency field-aligned auroral echoes observed from the U.S. and Australia. Using ionospheric models whose parameters were estimated, as far as possible, from vertical-incidence ionogram data, they confirmed the role of tilt-launched ground-detached propagation modes in the mechanism of long-range HF auroral echoes and also indicated how this mode, combined with the temporal and spatial variatons in the ionospheric parameters, could explain much of the observed diurnal behavior of their subject echoes. In a related investigation, Basu et al. [1974] employed a three-dimensional raytracing technique in a two-layer parabolic ionosphere model to locate the probable origin points of 19 MHz normal-aspect auroral echoes observed at Plum Island, Massachusetts. The parameters of their model ionosphere were derived from the standard ITS predictions. In a more generalized study, Millman [1974] plotted the spatial loci of origin of hypothetical normal-aspect field-aligned echoes which might be observed from Boston at representative frequencies in the HF through UHF bands. He based his ionosphere models upon vertical-incidence ionograms and included tropospheric refraction effects. Millman concluded that tropospheric effects were swamped b

ionospheric refraction at HF, and that the reverse was true at UHF, where ionospheric effects were nearly undetectable. Like Dearden [1962] and Basu et al. [1974], he noted that HF field aligned echoes often originated at multiple altitudes.

This work is an extension and partial synthesis of the efforts cited above. Since the foregoing studies have dealt with natural field-aligned column targets situated in remote geographic areas, their scope has been limited by incomplete knowledge of the target location and the state of the ionosphere along the propagation path. In contrast, because the location of the Platteville irregularity was known beforehand, and since the propagation routes lay near regularly-operating ionosonde stations, the present experiment afforded a unique opportunity to examine the influences of ionospheric refraction under relatively known conditions. This knowledge, in turn, permitted a very detailed echo modeling effort to reconstruct the sweep-frequency echo signature, using actual ionospheric data, and including the effects of tilts and focusing. In particular, with the high quality SFCW backscatter ionograms available for direct comparison, and with the sharply-defined traces resulting from the apparently compact target, it was possible to explore the natures and relative importance of the multiple echo components predicted by Dearden [1962] and others. An additional extension in this study was the treatment of a bistatic sounding geometry.

This undertaking differs fundamentally from the others in that it involves a man-made target. The scientific interest and motivations arising from this aspect have already been mentioned. It is also believed that this simulation is unique; the author is unaware of any other simulation studies of HF sweep-frequency echoes from the Platteville irregularity.

5.4.3 Methods and procedures

The simulation process consisted of three major phases: 1) To ascertain the effects of ionospheric refraction by tracing the Lost Hills-Platteville and Los Banos-Platteville raypaths through suitable model ionospheres, 2) To find the LH-PL and LB-PL raypath pairs

corresponding to specular echoes from field-aligned columns over Platteville (echo detection), and 3) to construct and interpret the synthetic frequency-time echo signatures. The first two topics will be discussed in outline below; the third is best illustrated by example, and will therefore be treated in the course of the actual simulation operations presented later in this chapter.

The raytracing task was to find the raypaths linking the ionospheric perturbation with the radar terminals at representative frequencies in the 9-27 MHz band, and to determine the aspect angle relative to the geomagnetic field for each ray which entered the scattering region. Magnetoionic and collisional effects were neglected in performing the raytracing computations, and the refractive index of the medium was therefore given by the simplified Appleton-Hartree formula (2.7). This simplification is justified in Appendix B.

To find the raypaths linking the geographic points LH and LB with the sizable region occupied by the disturbance, rays were traced outward from the radar terminals toward Platteville. The reciprocity principle [Budden, 1966, p. 502] was then applied, so that the LB raypaths, with their wavenormals reversed, defined uniquely the streamlines of the receivable portion of the hypothetical scattered radiation field. A stock of candidate raypaths was thus assembled from which could be selected those members representing specular reflections from field-aligned ionized columns above Platteville.

The raytracing techniques and the ionosphere models were designed to provide and use as realistic data as possible. Two different computer raytracing programs were employed. The first was a very general program developed at ESSA (now NOAA) by Jones [1966, 1968], and adapted to the Stanford IBM 360 computer by the author. This program integrates the Haselgrove equations [Haselgrove, 1955] to trace raypaths through an arbitrary refracting medium. It allows spatial variations of the refractive index in three dimensions and permits the effects of the geomagnetic field and electron-neutral collisions to be included in a complete fashion. However, the Jones program was expensive to operate, and a simpler program, based upon the "Mark 3" method of Croft [1969], was therefore written for use with certain simulation operations which required large amounts of data, but which did not require the complete three-dimensional raytrace effort.

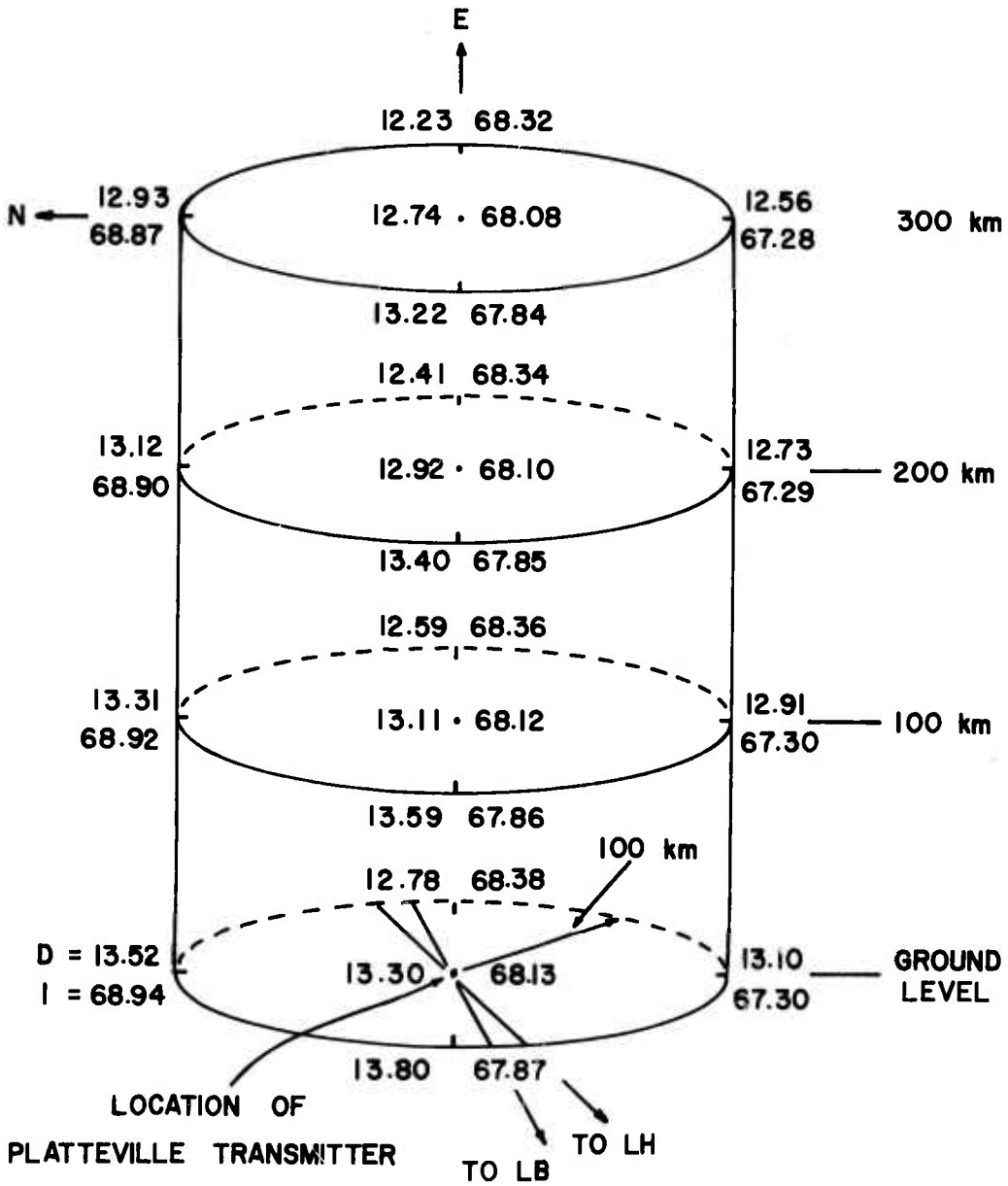

Fig. 5.5 Geomagnetic dip I and declination D in the vicinity of PL, as computed using the Jensen and Cain model of the geomagnetic field for epoch 1960.0.

all LH-LB raypath pairs which intersected within the model disturbance, and noting an echo event if the associated aspect angles of the rays met the specularity requirement at the intersection point. Two echo-detection methods were used in this study.

The most general echo-location method is the aspect-position diagram, which is constructed by plotting the aspect angle as a function of position for all rays traversing the scattering region. The intersections of the resulting LH and LB loci of a given frequency signify that the associated raypaths arrived at a common point at equal aspect angles, and thus establish unequivocally both the existence and the points of origin of field-aligned echoes at that frequency. Conversely, if the loci do not intersect, an echo may be confidently discounted.

However, this diagram in its complete form is a four-dimensional graph involving the aspect angle and the three positional coordinates, and is probably impossible to construct in a compact, useful form. Therefore, it was employed in an abbreviated format in this work; the aspect angle was plotted against the altitude coordinate only, measured along a vertical line passing through the center of the disturbance. This compromise retained the universality of the aspect-position technique, and thus permitted the assessment of the importance of cross-mode echoes and the verification of the twin-path echo phenomenon. Having settled these matters, the echo-contour chart method was then employed to examine the effects of the size and shape of the target.

An echo-contour chart is a map of the spatial loci from which field-aligned echoes may originate in a given radar configuration (see Figure 5.17 for an example). It is constructed by tracing a suitable number of raypaths from one of the sounder terminals (usually the transmitter) to the vicinity of the scattering region and noting the points at which the critical aspect is achieved. This presentation offers echo location data over a large physical area in a readily interpreted format, and such maps have been widely used in the analysis of field-aligned echoes [e.g., Chapman, 1952; Dearden, 1961; Millman, 1971; Basu et al., 1974].

However, the echo-contour method is a secondary technique, as it presumes the existence of a predetermined echo aspect angle, and hence it requires that the twin-path conditions be satisfied. Consequently, it has hitherto been applied only in monostatic radar geometries. An additional shortcoming of the echo-contour technique is its inability to incorporate readily cross-mode echoes, which generally do not occur at a predeterminable aspect. This potentially important echo mechanism is therefore disregarded when the echo-contour chart is employed as the primary echo-detection process. On the other hand, having established by the aspect-position diagram technique that the twin-path echo mechanism is predominant, the synoptic presentation of the echo-contour chart is very useful.

5.5 Simulation of the 1845 MST, 6 January 1972 Echo

5.5.1 Preliminaries

Because of its well defined band-limited character, the echo recorded at 1845 MST, 6 January 1972 (shown in Figure 5.3) was selected for the first simulation attempt. This signature commences at 13 MHz and extinguishes at 17 MHz; its propagation time span of 0.4 msec suggests a horizontal dimension of 60 km for the perturbed region. At this time, the Platteville transmitter was operating in the X polarization mode, and geomagnetic activity was quiet (Ap = 2).

The ST, BL, and WS $f_N(h)$ ionospheric profiles employed in this simulation are shown in Figure 5.6. Because all ionogram traces were obliterated at frequencies below 1.6 MHz by AM broadcast band interference, only the profile segments representing plasma frequencies greater than 1.6 MHz were derived from actual ionogram data. The remainder of each profile, including the E layer and the valley, was constructed using estimated parameters. This E region-valley structure was modeled upon the findings of Wakai [1967], who noted the presence of a distinct E layer and E-F valley in the winter evening ionosphere over Boulder during a geomagnetically quiet interval. Therefore, the bottomside E layer of each profile in Figure 5.6 was represented by a Chapman layer of 10 km scale height. Adopting the result of an E layer true-height analysis performed upon the ST ionogram recorded at 1715 MST,

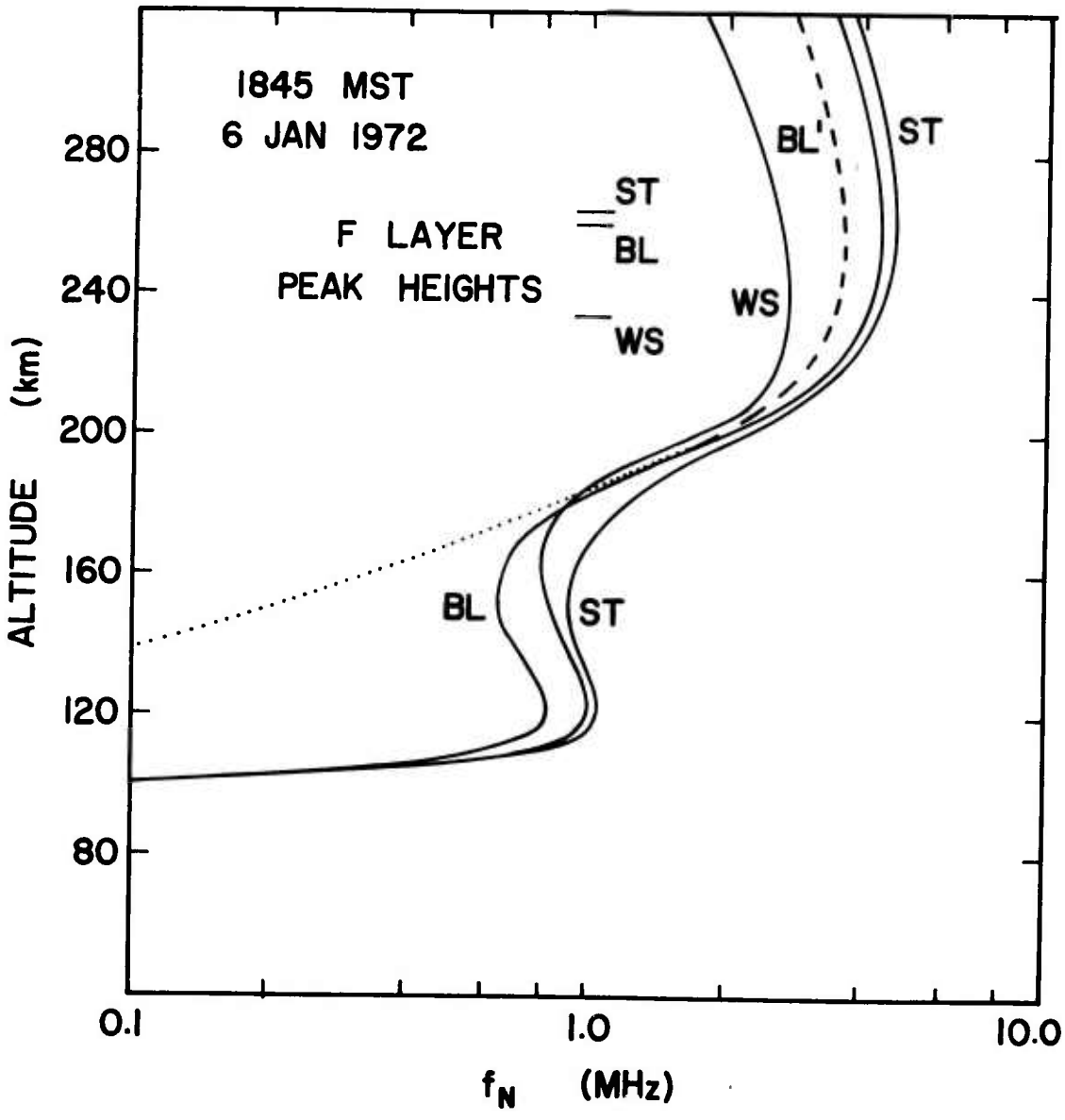

Fig. 5.6 The $f_N(h)$ profiles at 1845 MST, 6 January 1972.

5 January 1972, an E layer peak height of 120 km was assigned to each profile. The critical frequencies were derived from estimates employed by WDC-A in the true-height analysis of the F region (see Wright [1967]) and finally the valley profiles were fitted in the manner described in Appendix A.

Since the parameters of this lower portion of the ionosphere were derived from estimates, the refractive properties of this model ionosphere may not accurately represent the actual medium, and the resulting

errors must be estimated and corrected for. This is done in Appendix E where it is shown that even gross alterations in the E layer-valley structure have a negligible effect upon the characteristics of the simulated echo.

5.5.2 The first simulation

The first step in this simulation was to generate the data needed to construct the aspect-altitude diagram. Using the Jones program, rays were traced from the LH and LB sounder terminals to a vertical line extending upward from the Platteville transmitter. To cover the frequency band occupied by the observed echo, the ray data were computed at 2.5 MHz increments from 10.0 MHz to 20.0 MHz. A pilot series of rays was first traced at each frequency in 0.5° initial elevation steps from 0.0° through 10.0°, and additional raypaths were subsequently computed as needed. Tropospheric refraction was neglected.

The model target described above neglects the magnetoionic deviation of the heater signal, which should position the actual perturbed region about 10 km north or south of the transmitter zenith for O and X heating modes, respectively (see Utlaut and Cohen, [1971]). However, raytracing experiments involving such displaced targets established that the consequent errors in the results were negligible. To simplify the aspect angle computations, the altitude variation of the geomagnetic direction was neglected, and a constant orientation of $I = 68.09°$, $D = 12.83°$ was employed. This orientation corresponds to the 250 km approximate altitude of the F layer peak, where the disturbance was expected to be the most pronounced. Figure 5.5 indicates a variation of 0.02° in I and 0.18° in D in the 200-300 km altitude interval which, as will be seen, contains the simulated field-aligned echoes. It is shown in Appendix E that the effects of disregarding this variation are insignificant.

Figure 5.7 shows the resultant aspect-altitude diagram. Each curve on this plot represents the possible combinations of aspect and position of the rays arriving at the target at the indicated frequency. The set of curves labeled "LH rays" represents the illuminating radiation field, and were plotted using the aspect data directly from the raytrace program. Those designated "LB rays" define the characteristics of the

receivable radiation field; to effect the required wavenormal reversal, they were plotted using the supplement of the computed aspect angle. The open circles denote those rays whose initial elevation angle was an integral number of degrees, thus indicating the data density required to construct the diagram. No such circles appear on the rightmost 10.0 MHz loci; the raypaths defining these curves were propagated via a very defocused mode, and the entire segments shown correspond to rays with initial elevation angles between 22.1° and 22.2°. Because of this very low data density, these curves were drawn as broken lines.

As pointed out in the preceding section, the conditions for a field-aligned echo are met at the intersections of the loci of the same frequency. Each curve pair on Figure 5.7 has two such intersections, which are typically separated in altitude by several tens of kilometers. All of these echo points occur at the constant value $\theta = 88.8°$, independently of frequency or altitude, thus fulfilling the expectation of an invariant echo aspect. This $\theta = 88.8°$ locus is denoted the "line of echoes." It will be also noted that the LH and LB loci are symmetric about this line. These circumstances indicate that the respective LH and LB raypaths were effectively identical to one another and, in particular, that the echo intersections were comprised of essentially twin raypaths.

As the radio frequency increases, the echo points move toward each other along the line of echoes. Although their actual convergence is not shown, it is apparent that this must occur at the frequency at which the LH and LB loci form an osculating curve pair, with each curve being tangent to the other and to the line of echoes. No echo intersections exist above this frequency of osculation for, as the frequency increases above this value, the LH-LB loci pairs progressively withdraw from one another and approach asymptotically the limiting curves labeled "$f = \infty$", which were computed for straight-line raypaths and do not intersect. (The higher-frequency curves illustrating this trend were omitted from Figure 5.7 for clarity; they are shown in Figure 5.10.) The upper extinction frequency of the synthetic field-aligned echo is therefore equal to the osculation frequency. In this instance, this frequency lies between 17.5 and 20.0 MHz. Its actual value may be determined by

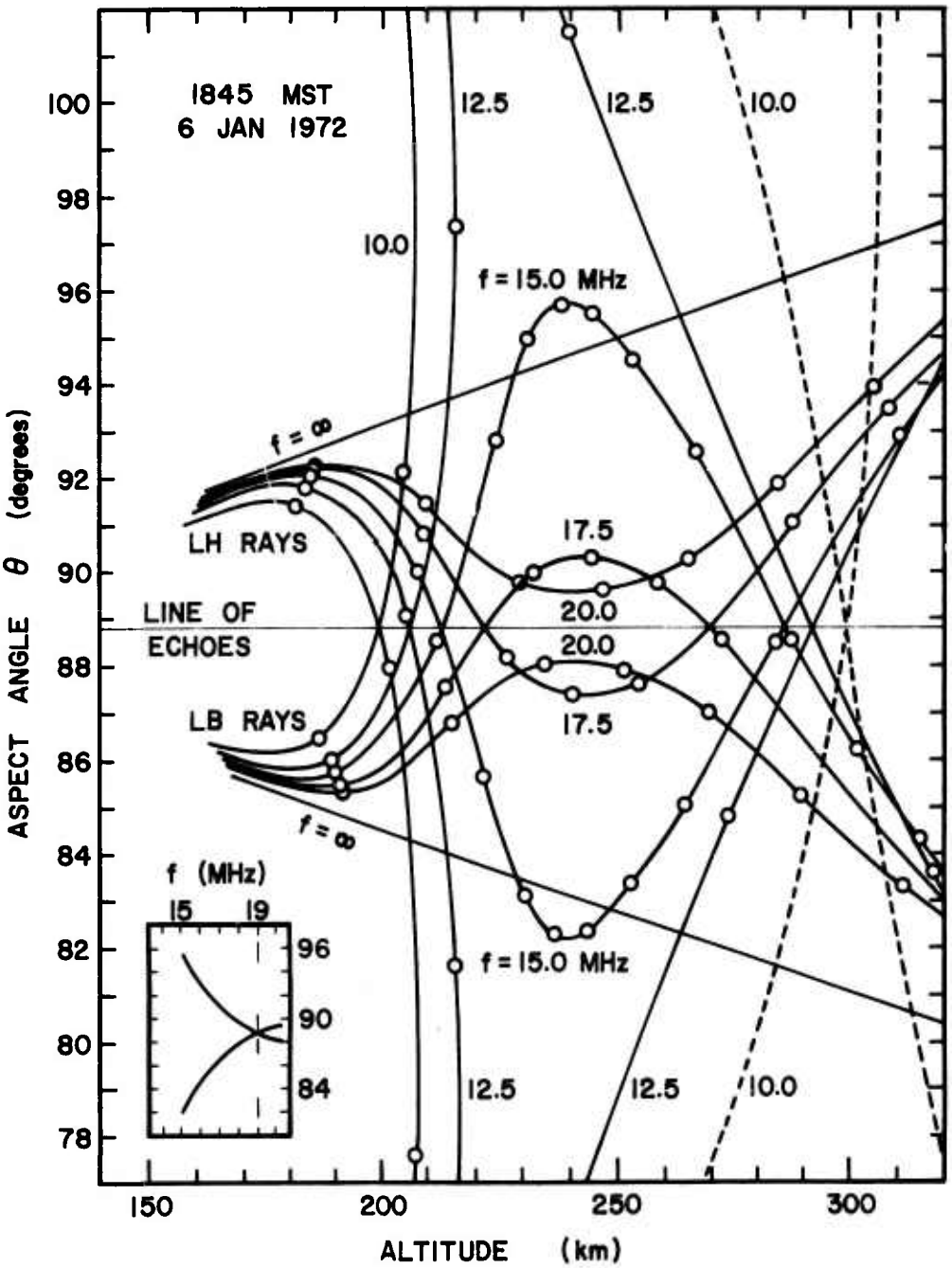

Fig. 5.7 The aspect-altitude diagram for the first simulation of the echo of 1845 MST, 6 January 1972.

interpolating to find the frequency at which the horizontal tangents to a curve pair coincide. This interpolation is performed graphically in the inset of Figure 5.7, where the aspect corresponding to the dip (or peak) in each curve is plotted against frequency. An echo upper extinction frequency of 19 MHz is found at the intersection of these loci.

The synthetic sweep-frequency echo trace derived from this data is shown in Figure 5.8a, together with a schematic reproduction of the observed echo signature. To construct this trace, the round-trip echo signal travel time was determined by summing the group propagation delays computed for the raypath pairs forming the echo intersections on Figure 5.7. The results were then plotted against the radio frequency, and a smooth curve was drawn through the points.

The synthetic echo trace consists of an upper and a lower branch, separated in propagation time. These branches originate respectively from the upper and lower altitude echo points on the aspect-altitude diagram of Figure 5.7, and thus comprise the multiple-altitude echoes whose existence had been indicated by Dearden [1961] and Millman [1974]. It is instructive to examine the relative degrees of refractive defocusing of these branches and, in so doing, to attempt to determine why the actual echo signature shows no corresponding bifurcation. For example, it was pointed out earlier that the upper 10 MHz echo intersection on Figure 5.7 is formed by a very defocused propagation mode, which indicates that the intensity at the lower frequencies of the associated upper echo branch may be quite low.* To assess this effect more precisely, the focusing computations described below were undertaken.

To calculate the degree of refractive focusing, it is in general necessary to compute the degree of convergence or divergence of the flux tubes formed by closely spaced raypaths along both the illuminating and returning echo signal paths. However, since LH and LB raypaths comprising the echo are virtually identical, it suffices to compute the

* A caveat is in order here. As will be shown in Section 5.6.4, it is not possible in general to identify the upper and lower echo branches respectively with the upper-ray and lower-ray propagation modes. Consequently, the well-known relative focusing properties of these modes cannot necessarily be invoked to judge the relative intensities of the echo branches.

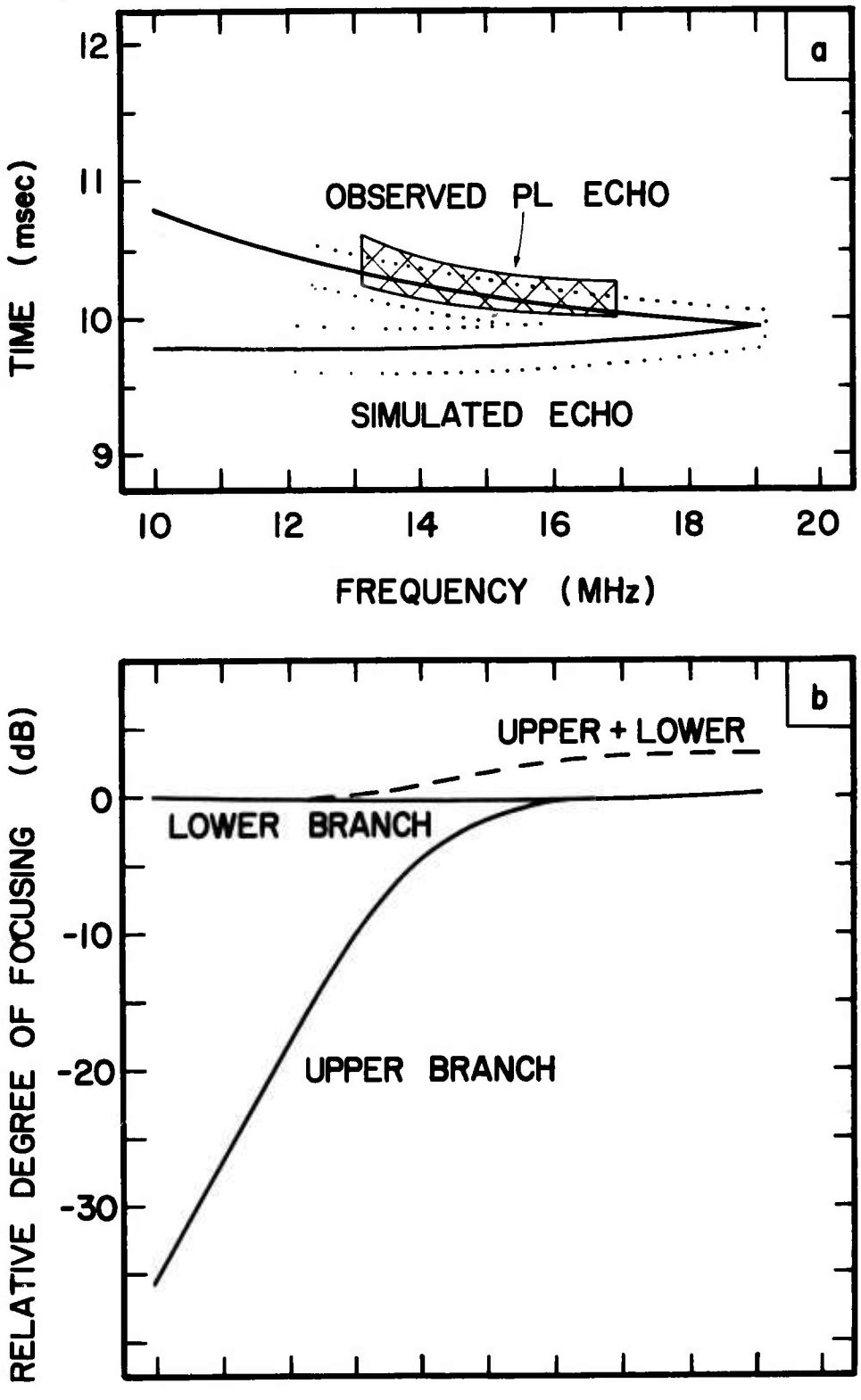

Fig. 5.8 (a) Comparison of the actual 1845 MST, 6 January 1972 echo signature with the simulated trace derived from the aspect-position data of Figure 5.7. (b) The relative intensities of the synthetic echo components due to refractive defocusing in the ionosphere.

degree of focusing of only the LH rays illuminating the target; the total round trip of focusing is the square of this quantity. A suitable metric of illumination focusing, derived in Appendix C, is given by

$$F \propto (dh/d\beta_0)^{-1} \tag{5.1}$$

where h is the height at which the ray launched from LH at the initial elevation β_0 crosses the target.

Figure 5.8b shows the quantity 10 log F^2 plotted as a function of frequency for both branches. To obtain this curve, the derivative in (5.1) was approximated by differentiating a cubic natural spline interpolating function fitted to the raytrace data, and the results were then normalized to the value of F computed for the lower echo branch at 10 MHz. The resultant plot represents the relative strength due to focusing effects, in dB, of the sweep-frequency echo components.*

The two echo branches exhibit markedly different frequency dependencies. While the lower branch intensity is nearly invariant over frequency, the upper branch evolves from a highly defocused state at 10 MHz to exceed slightly the intensity of the lower branch at frequencies greater than 17 MHz. Since the dynamic range of the receiver video display is approximately 15 dB, the saturation of the observed echo near 17 MHz indicates that its visibility was at least this great. Consequently, a relative defocusing of more than about 15 dB should render the affected portion of the echo trace invisible. Figure 5.8b indicates such defocusing occurs on the upper branch mode at frequencies less than 12.3 MHz.

The commencement frequency of the lower echo branch may be determined by considering the altitude extent of the scattering disturbance. Figure 5.7 shows that the height at which the lower-branch echo originates rises as the radar frequency increases. If the lower boundary of the scattering region lies within this altitude range, the lower-branch echo should therefore commence at the frequency whose echo point

---

* For simplicity, variations in the elevation-plane radiation patterns of the LH and LB antennas have been neglected. These patterns have not actually been measured but, owing to the vertical array elements employed, pronounced variations are not anticipated over the range of elevations considered here ($\beta_0 \geq 4°$).

on Figure 5.7 lies upon this boundary. This boundary altitude was estimated using the BL vertical ionogram shown in Figure 5.3, which has spread-F traces at all reflected frequencies above an ill-defined lower limit. The scattering region presumably began at the altitude from which this lower limit frequency was reflected. Therefore, following the ordinary trace leftward from the F layer cusp, its ragged aspect becomes significantly less pronounced at 2.6 MHz, and the first vistiges of tatters identifiable with the primary spreading appear at 2.2 MHz. Transferring these values to the solid-line Boulder profile of Figure 5.6 yields the corresponding vertical-incidence reflection altitudes of 209 and 205 km, respectively. Figure 5.7 shows that lower echoes in the interval 12.1-13.6 MHz originate within this range.

The foregoing results indicate that the synthetic echo must include contributions from both branches, and therefore its total strength is the sum of the intensities of these constituents. The quantity is represented by the broken line on Figure 5.8b. Hence, using the high-frequency tip of this curve as the maximum intensity reference level, a new -15 dB upper-branch commencement frequency of 12.7 MHz is estimated, which provides a slightly better match to the 13 MHz experimental value than the previous single-branch 12.3 MHz figure. The lower-branch commencement estimate is unchanged.

As the final step in this simulation, the horizontal size of the disturbance was accounted for by widening the synthetic traces to the 0.4 msec width of the observed signature. The outlines of the modified trace, taking into account the foregoing commencement estimates, are shown by the dotted lines on Figure 5.8a. It will be shown in Section 5.6.4 that no significant correction of the upper extinction frequency is required. This elementary modification is adequate for the present purpose; a full exploration of the echo signature characteristics arising from the shape and size of the target will be carried out with the echo of 1715 MST, 6 January 1972, whose greater range extent and structural details provide a better specimen for the echo-contour chart technique.

5.5.3 The second simulation

A noteworthy discrepancy in the simulation results is the fact that the 19 MHz extinction frequency of the synthetic echo exceeds the actual echo cutoff by 2 MHz. While this mismatch is not necessarily serious, it is instructive to explore its origin as, in doing so, some insight can be gained into the factors controlling the accuracy and reliability of the simulation.

Two possible error sources may be immediately dismissed. The first of these, a relaxation of the strict specularity requirement, can be represented by broadening the line of echoes on Figure 5.7. It is obvious that this raises the simulated extinction frequency, and thus increases the discrepancy. The second possibility, errors in the ray-tracing computations arising from errors in reconstructing the lower $f_N(h)$ profiles, is treated in Appendix E, where it is shown that these effects are too small to bring about the 2 MHz discrepancy.

On the other hand, an error in the structure of the model F region might account for the disparity. If the refractive power of this layer is too great, the rays will suffer excessive downward bending, so that the required orientation for a field-aligned echo will be established at an unduly high radar frequency.

An overestimate of the F region ionization density, leading to an overly refractive medium, might arise in this instance from two causes. The first of these is the ambiguity inherent in scaling the very diffuse traces near the critical frequency on the BL ionogram of Figure 5.3. The virtual-height data used in the foregoing simulation was scaled by the WDC-A staff from the more pronounced outer edge of the O-mode trace. However, it is likely that this feature, along with the tatters above it, is the result of energy scattered from the component irregularities of the disturbance itself. Energy reflected from the ambient background ionization in the usual manner very likely forms the inner edge of the O-mode trace, giving a lower estimate of the f_oF_2. This is the basis of the general rule specifying that the critical frequency be scaled from the inner edge of the spread cusp [Piggott and Rawer, 1961]. However, this rule is not absolute, and a considerable latitude is given to the judgement of the person doing the scaling. Since most of the

refractive bending of the HF sounder signals occurs in the region of the model ionosphere strongly influenced by the BL profile, this scaling ambiguity is the most serious of all conceivable error sources.

The second cause of an overestimate of the F region ionization density is the "spur" in the 6 January 1972 Boulder f_oF_2 trend shown in Figure 5.9. This diagram shows that several such peaks (and also dip[s] in f_oF_2 occurred throughout the day at each ionosonde location (e.g., WS: 1000, 1115, 1630 MST; ST: 1940 MST). As evidenced by their non-simultaneous uncorrelated occurrence, these are local events. However, such small-scale effects cannot be reproduced by the ionospheric model used here. Owing to the linear interpolation scheme, a local ionization enhancement in any of the three $f_N(h)$ profiles is propagated throughout the horizontal dimension of the model ionosphere. In this particular case, such an enhancement in the BL profile would appear along the entire California-Platteville route, producing an unduly large downward refraction of the computed raypaths.

Overestimates of the ionization density along the California-Boulder path arising from either of these causes will result in an overlarge extinction frequency of the synthetic echo. Consequently, it was undertaken to determine if a better agreement with the experimental data could be obtained after appropriately removing this extra ionization.

Since no information was available concerning the precise height distribution of the ionization to be subtracted, it was decided to reduce the electron concentration throughout the Boulder F layer profile by a scheme which removed a progressively larger fraction of the ionization as altitude increased from a base height to the layer peak. After some experimentation, this base height was fixed at 190 km to allow a smooth transition between the new and unaltered profile segments. An ambient f_oF_2 value of 3.6 MHz was scaled from Figure 5.9 by fitting the straight broken line AB to the Boulder f_oF_2 trend, as defined by the inner edge of the spread-F ionogram trace cusp, and new values of electron density were then computed using the expression

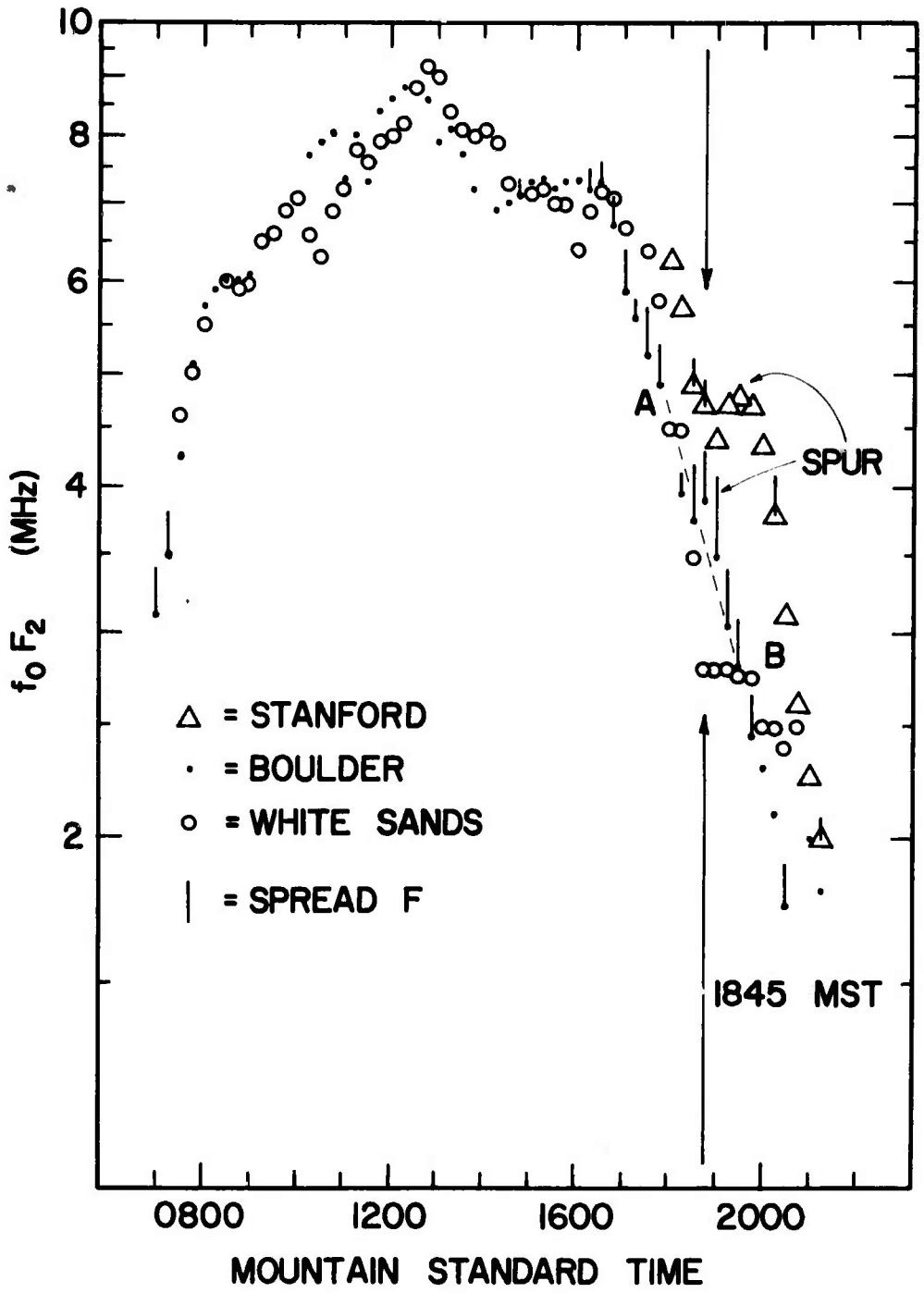

Fig. 5.9 f_0F_2 vs. time on 6 January 1972 at Stanford, Boulder and White Sands.

$$f_N^2(h) = f_{N0}^2(h) \left\{ 1 - A\left[\frac{h - 190}{h_p - 190}\right]^{0.5} \right\} \Bigg|_{h \geq 190} \qquad (5.2)$$

where f_{N0} = the original plasma frequency at height h,

A = the desired fractional decrease of f_N^2 at the layer peak

h_p = the layer peak height.

The exponent 0.5 was chosen after a first computation showed that a unity value caused an undesired lowering of the layer peak. Its precise value is unimportant, since (5.2) was constructed for computational convenience only and does not model a physical process. The new profile is shown as the dashed line labeled BL′ on Figure 5.6.

Figure 5.10 presents the aspect-altitude diagram for LH rays traced through this profile. Since the constancy of the echo aspect at 88.8° has been established, the LB rays need not be traced; field-aligned echoes are indicated where the curves cross the $\theta = 88.8°$ line. Proceeding as before, the upper extinction frequency is determined to be 16.5 MHz, and the new synthetic echo trace is shown in Figure 5.11a.

Figure 5.11b shows the focusing trends computed for this trace. Owing to the diminished refractive power of the modified profile, the relative strength of the upper echo branch is greater than that of the previous simulation. Its -15 dB commencement frequency is consequently lower, 10.5 MHz. With the contributions from both echo branches considered together, the commencement is placed at 11.0 MHz. This is 1.3 MHz lower than the previous simulated value, and 2 MHz less than the observed onset frequency.

As before, the lower branch focusing intensity is practically constant. Using the BL′ profile of Figure 5.8, the lower boundary of the scattering region is placed between 207 and 212 km, and the commencement of the lower branch synthetic trace is thus determined to lie between 11.9 MHz and 13.3 MHz. This is not greatly different from the 12.1-13.6 MHz range found previously, and contains the 13 MHz observed commencement.

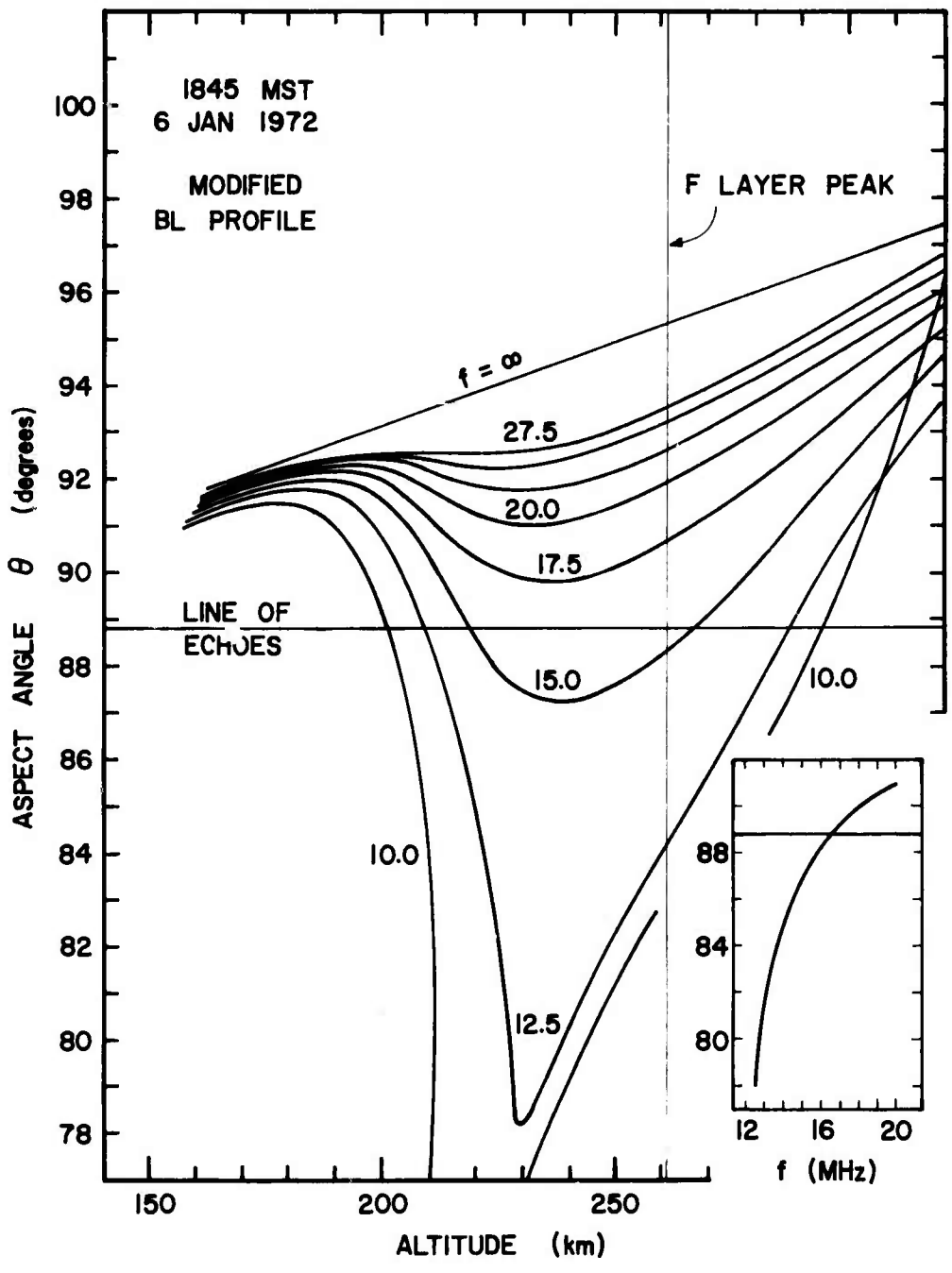

Fig. 5.10 The aspect-altitude diagram for the second simulation of the 1845 MST, 6 January 1972 echo signature.

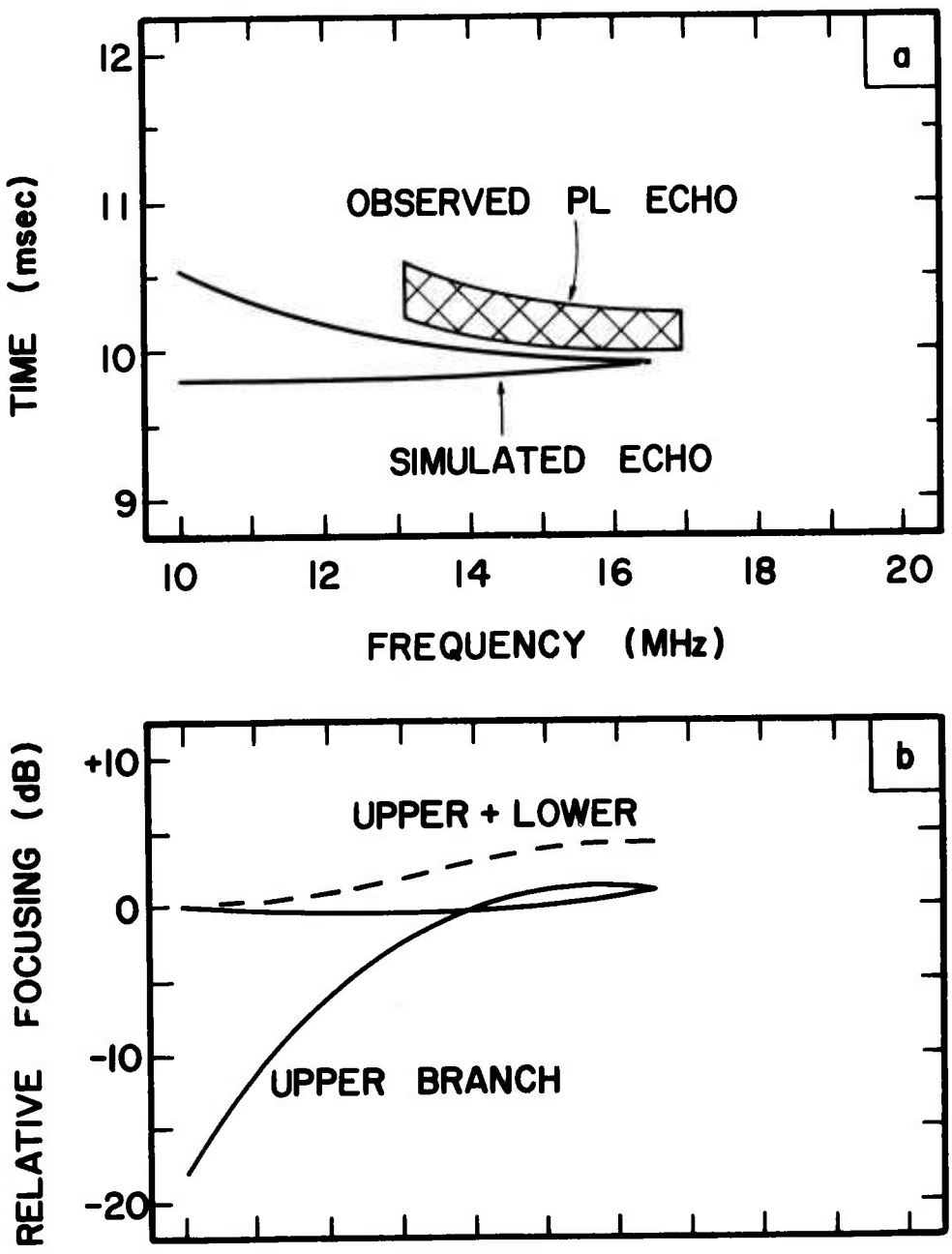

Fig. 5.11 (a) The 1845 MST, 6 January 1972 echo signature simulated using the modified BL $f_N(h)$ profile, with a reproduction of the observed signature for the comparison. (b) The relative intensities of the synthetic echo branches due to refractive defocusing in the ionosphere.

Two values of the upper extinction frequency of this simulated field-aligned Platteville echo have been determined, corresponding to two limiting possibilities of the Boulder F region structure. The simulated extinction should therefore be somewhere within this 16.5-19.0 MHz interval, which also contains the observed extinction frequency.

5.6 Simulation of the 1715 MST, 5 January 1972 Echo

5.6.1 Preliminaries

In order to study the echo signal propagation under different ionospheric condictions, and to examine the effects arising from the size and shape of the scattering region, the simulation of the echo recorded at 1715 MST, 5 January 1972 was undertaken. This signature, shown in Figure 5.2d, begins diffusely at 21 MHz, intensifies to saturate the video display by 25 MHz, after which the maximum range decreases linearly to produce a trace width of 0.5 msec at extinction. In addition, a weak signature extending from 11.0 to 11.5 msec near 11.5 MHz can be identified as an echo from the same disturbance. Geomagnetic activity was again quiet (AP = 6), and the Platteville transmitter was operating in the O magnetoionic mode.

Figure 5.12 shows the ST, BL, and WS $f_N(h)$ profiles for this time. The E layer of the Stanford profile was derived from actual ionogram data; but since the corresponding traces were again obliterated by AM broadcast band interference on the BL and WS ionogram records, the lower portions of these profiles were approximated as described in Section 5.5. It is worth noting that these profiles have greater ionization densities than do their counterparts of 1845 MST, 6 January, primarily because they represent conditions 1.5 hours earlier in the day. The field-aligned echo generation theory predicts that the increased refractivity of this ionospheric medium will allow this echo to be observed at higher radar frequencies than its 6 January counterpart, and this is what is observed.

5.6.2 Simulation of the primary echo

This echo was simulated twice, using both of the raytracing and data display techniques previously discussed. The first simulation employed the full three-dimensional raytracing procedure and

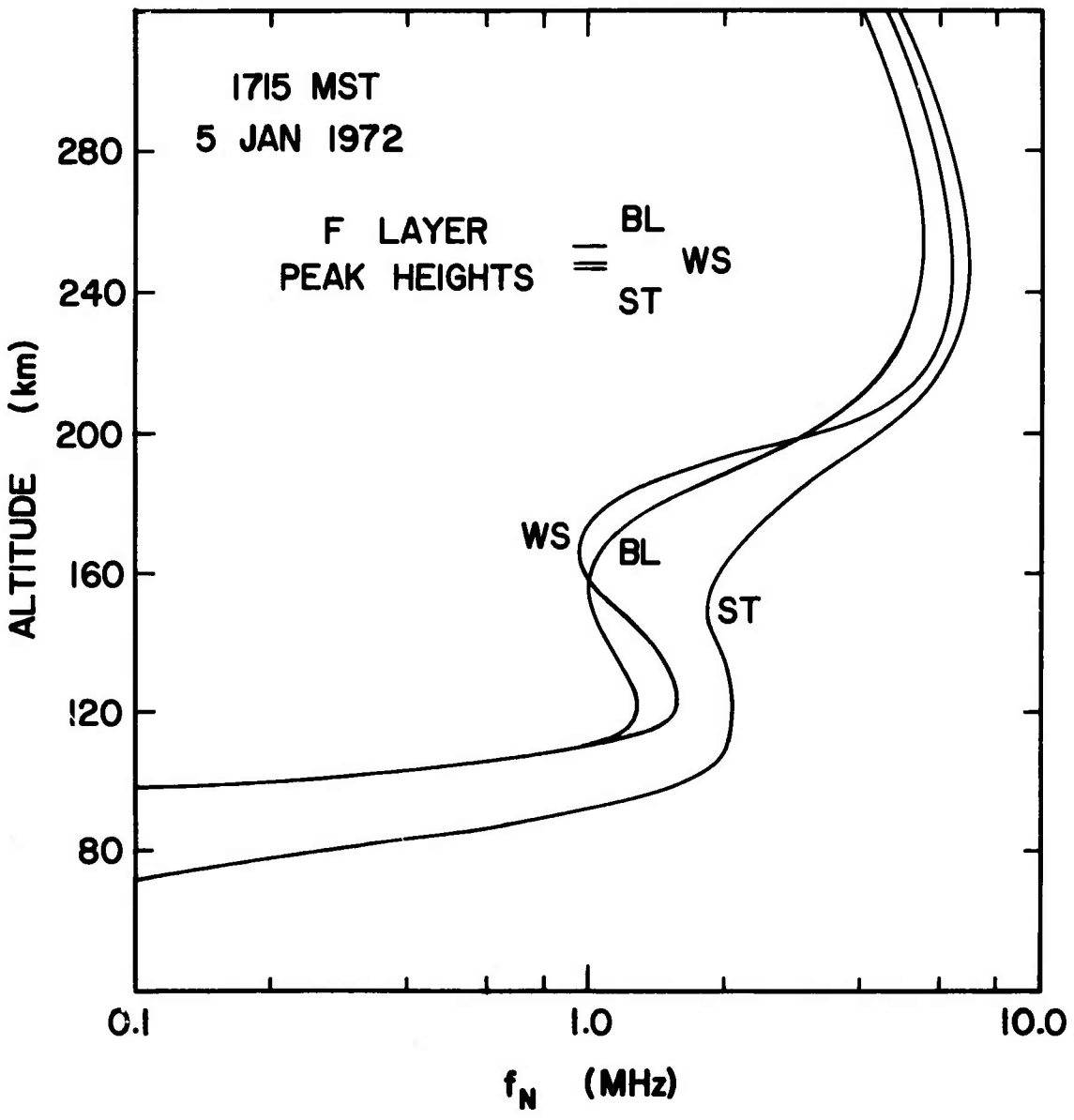

Fig. 5.12 The $f_N(h)$ profiles at 1715 MST, 5 January 1972.

the aspect-altitude diagram, in the manner of the preceding simulation. Complete account was thus taken of ionospheric tilts, and the duplication in method allowed this new synthetic echo to be directly compared with and checked against the simulated echo of 6 January. In the second treatment, a series of echo-contour charts was constructed showing the spatial loci from which field-aligned echoes might originate in the Platteville vicinity. By outlining on these maps the region presumably

occupied by the disturbance, the effects due to its size, form, and location could be examined.

Again assuming the disturbance to be centered directly above the Platteville transmitter, rays were traced from LH as before, and the aspect angles of the rays at the target are plotted in the aspect-altitude diagram of Figure 5.13. Field-aligned specular echoes are indicated wherever the LH curves cross the $\theta = 88.8°$ line of echoes. Owing to an extreme degree of defocusing, the rays comprising the upper echo branch at frequencies below 15 MHz could not be traced with adequate data density to be shown on this diagram.

The resulting echo trace is presented with a reproduction of the observed echo on Figure 5.14a. Its cutoff frequency of 25.3 MHz is acceptably near the 25.5 MHz observed value. While the spread traces on the Boulder vertical ionogram (Figure 5.2d) would allow some adjustment of the F layer profile to reconcile these frequencies, this was not undertaken in this instance. The commencement frequencies of the two echo branches can be determined once again from consideration of focusing and the lower boundary altitude of the disturbance. Figure 5.14b shows the relative focusing strengths of the echo branches, normalized to the lower branch intensity at 10.0 MHz. As observed with 1845 MST echo, the lower branch strength is practically invariant with frequency, while the upper branch is highly defocused at the lower frequencies. Owing to the relatively more dense ionospheric plasma, this defocusing is much more severe than was previously noted; the relative intensity is down 46 dB at 15 MHz and is rapidly declining. Assuming the echo to consist of the upper branch only, the -15 dB value occurs at 18 MHz; considering both branches, this level is reached at 18.4 MHz.

The lower boundary altitude of the scattering region may again be estimated by scaling the onset of trace spreading from the BL vertical ionogram. This record, shown in Figure 5.2d, exhibits frequency spreading of the ordinary trace beginning definitely at 4.4 MHz, and the tattered appearance of this signature persists until its junction with the extraordinary trace at 3.8 MHz. The corresponding BL true-height profile in Figure 5.12 yields the reflection altitudes 214 and 207 km, respectively, to define the probable lower boundary of the scattering

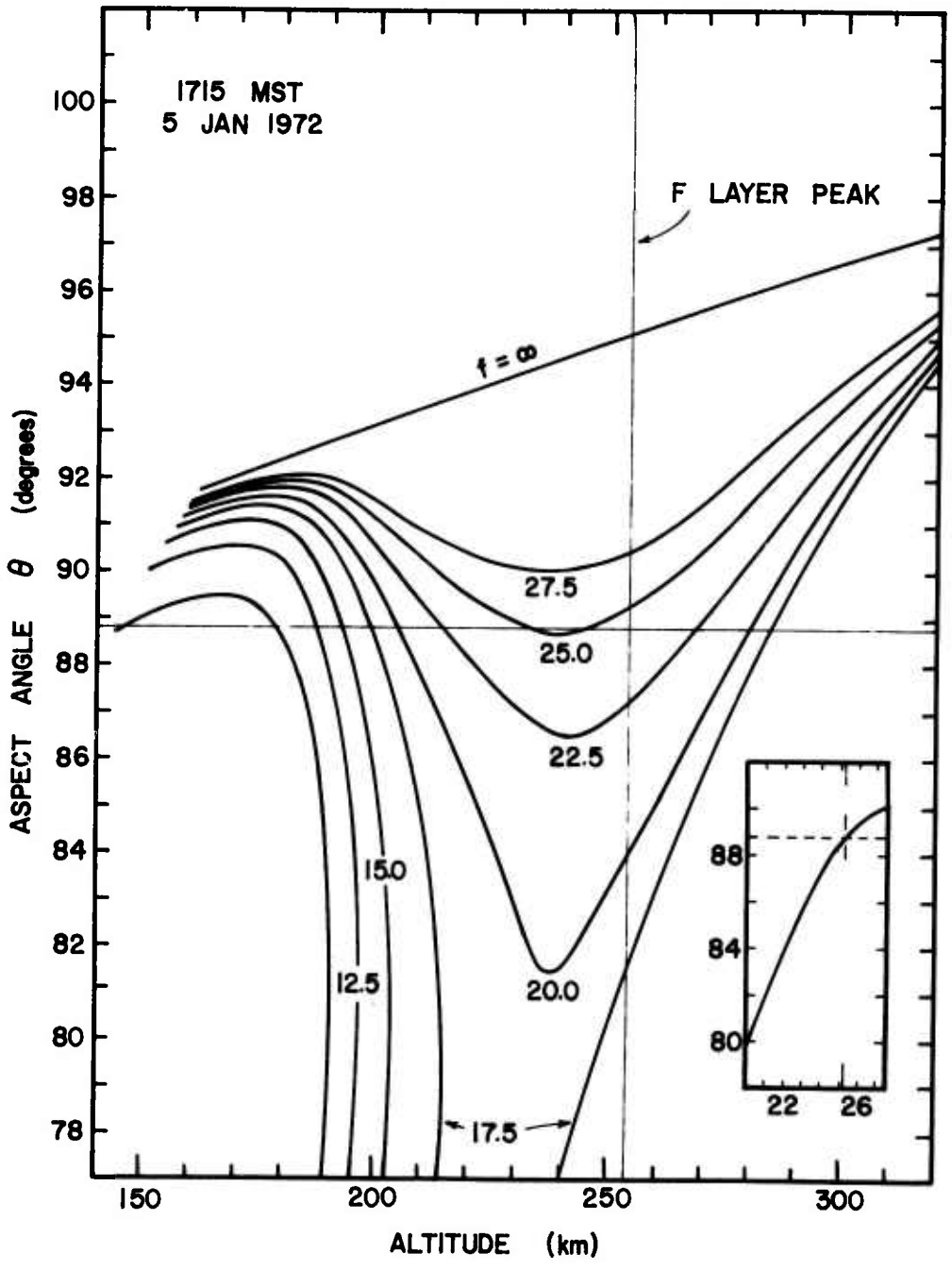

Fig. 5.13 The aspect-altitude diagram for 1715 MST, 5 January 1972

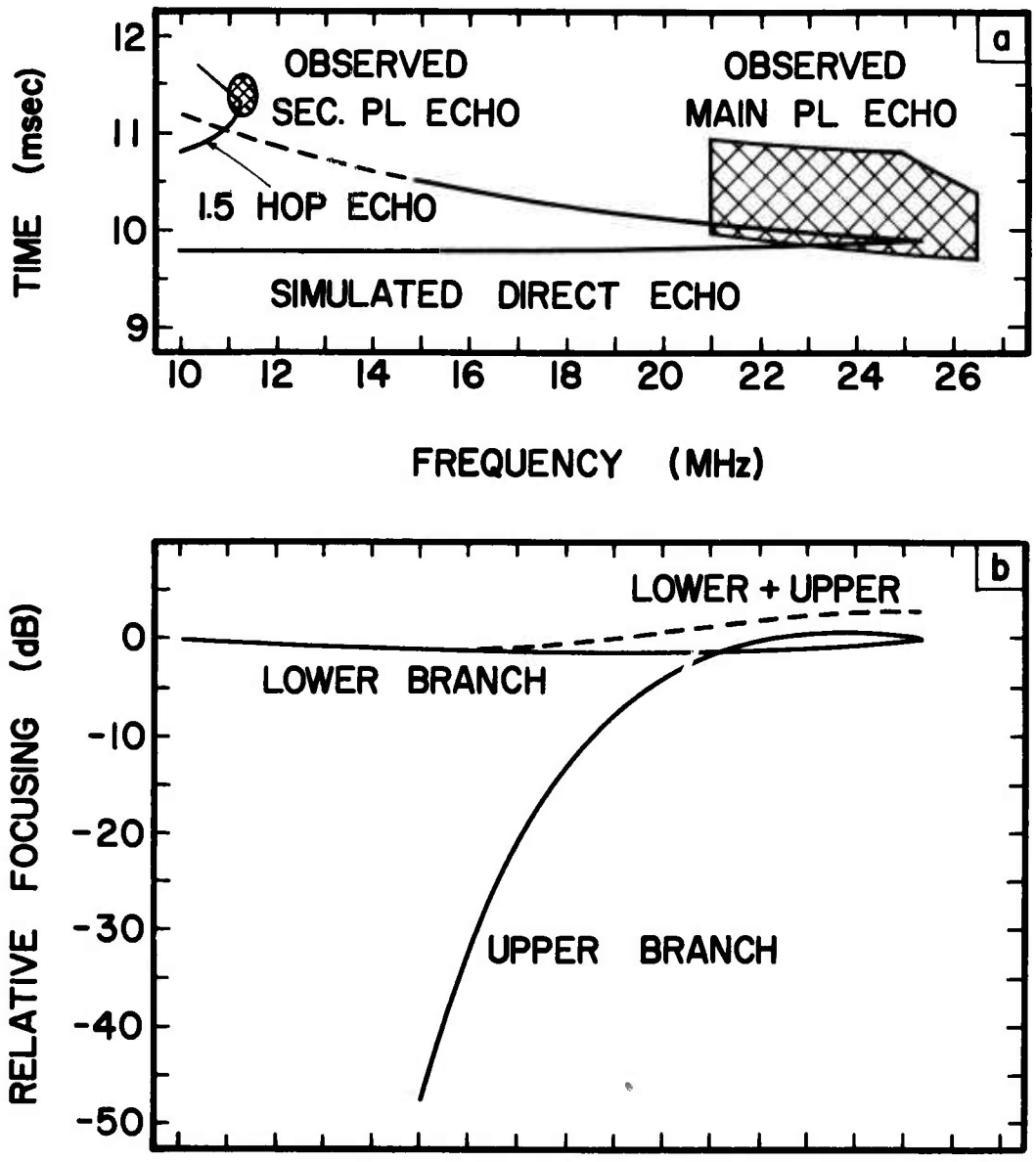

Fig. 5.14 (a) The simulated and observed echo signatures for 1715 MST, 5 January 1972. (b) The relative intensities of the synthetic echo branches due to refractive defocusing.

region, and Figure 5.13 shows that lower-branch echoes of 22.5 and 20.6 MHz originate at these heights. This interval contains the 21 MHz observed commencement frequency.

5.6.3 Simulation of the secondary echo

It was indicated in Section 5.2.2 that, since the presence of the faint signature labeled "sec PL echo" on the experimental record of Figure 5.2d correlates with the on-off state of the Platteville transmitter, it must represent an additional echo from the artificial disturbance. It is the purpose of this section to study this echo.

Although the extrapolated range trend of the upper-branch synthetic echo on Figure 5.14a would match the observed range of this secondary echo very well, the extreme defocusing of this mode (> 50 dB) removes it from consideration. However, re-examination of the position of this echo on the backscatter ionogram, where it lies at a range greater than that of the minimum range of the ground backscatter return, indicates that the responsible propagation mode must have involved a ground reflection along at least one leg of its round-trip journey, perhaps on both. There is thus a possibility of a cross-mode as well as a same-mode echo mechanism, with the echo signal traveling outward by a direct path and returning via a single ground hop, or vice-versa.

Since no specific data concerning the nature of the ground reflection were available, it was assumed to occur specularly from a spherical earth. When both the LH and LB signals undergo this ground hop, it is to be expected that field-aligned twin-path echoes would originate at the 88.8° aspect angle. To define these ground-hop modes, rays were traced from Lost Hills to the vertical line extending upward from Platteville, at 0.5 MHz intervals from 10.0 to 12.0 MHz. The initial elevations were chosen by experiment so that the rays arrived at the target following one ground reflection, and the elevation increment was varied to give adequate data density on the aspect-altitude diagram.

The resultant loci are designated "ground-hop LH rays" in Figure 5.15, and same-mode echoes originate where these curves cross the $\theta = 88.8°$ line. The upper cutoff frequency of these echoes was fixed at 11.2 MHz, and the signature derived from this data is labeled "1.5 "hop same-mode echo" on Figure 5.14. Its extinction

frequency and apparent range (with allowances for the systematic error) match the observed signature very well.

The previously-derived 207-214 km estimate for the lower boundary altitude range of the scattering disturbance leads to an expected 10 MHz commencement frequency for the lower branch. This is 1 MHz below the 11 MHz observed echo onset frequency. The discrepancy might be attributed to defocusing effects; an alternative hypothesis is that the low-frequency portion of the echo trace was obliterated by the reaction of the receiver's automatic gain control (AGC) circuits to strong interfering signals. The experimental record of Figure 5.2d shows evidence of such AGC action. For this reason, it was felt that the quality of the experimental data did not warrant carrying out focusing calculations for this echo.

Cross-mode echoes may originate in this case whenever a specular reflection couples signal energy arriving from the transmitter via the ground-hop mode into a direct mode reaching the receiver, or inversely. To search for such coupling, the aspect-position loci were plotted on Figure 5.15 for the direct-mode raypaths traced from the LB receiver at 10 and 12 MHz (taking, as before, the supplement of the computed aspect angle to effect the necessary wavenormal reversal). The cross-mode echoes are indicated where these curves (labeled "direct LB rays") meet the ground-hop loci. These intersections are marked by diamonds on Figure 5.15, both for the 10 and 12 MHz frequencies explicitly represented, and as estimated for the intervening frequencies whose LB rays were not actually traced.

The cross-mode echoes are seen to originate at a variety of aspect angles whose actual value is a function of frequency, altitude, and the nature of the propagation mode involved. It is apparent from the trends displayed by both sets of loci that these returns must cease between 12.0 and 12.5 MHz, but there is no indication of a lower frequency limit. Since all of the echo intersections lie beneath the 207 km least estimate of the lower disturbance boundary height, the cross-mode mechanism was probably not a significant echo source in this case.

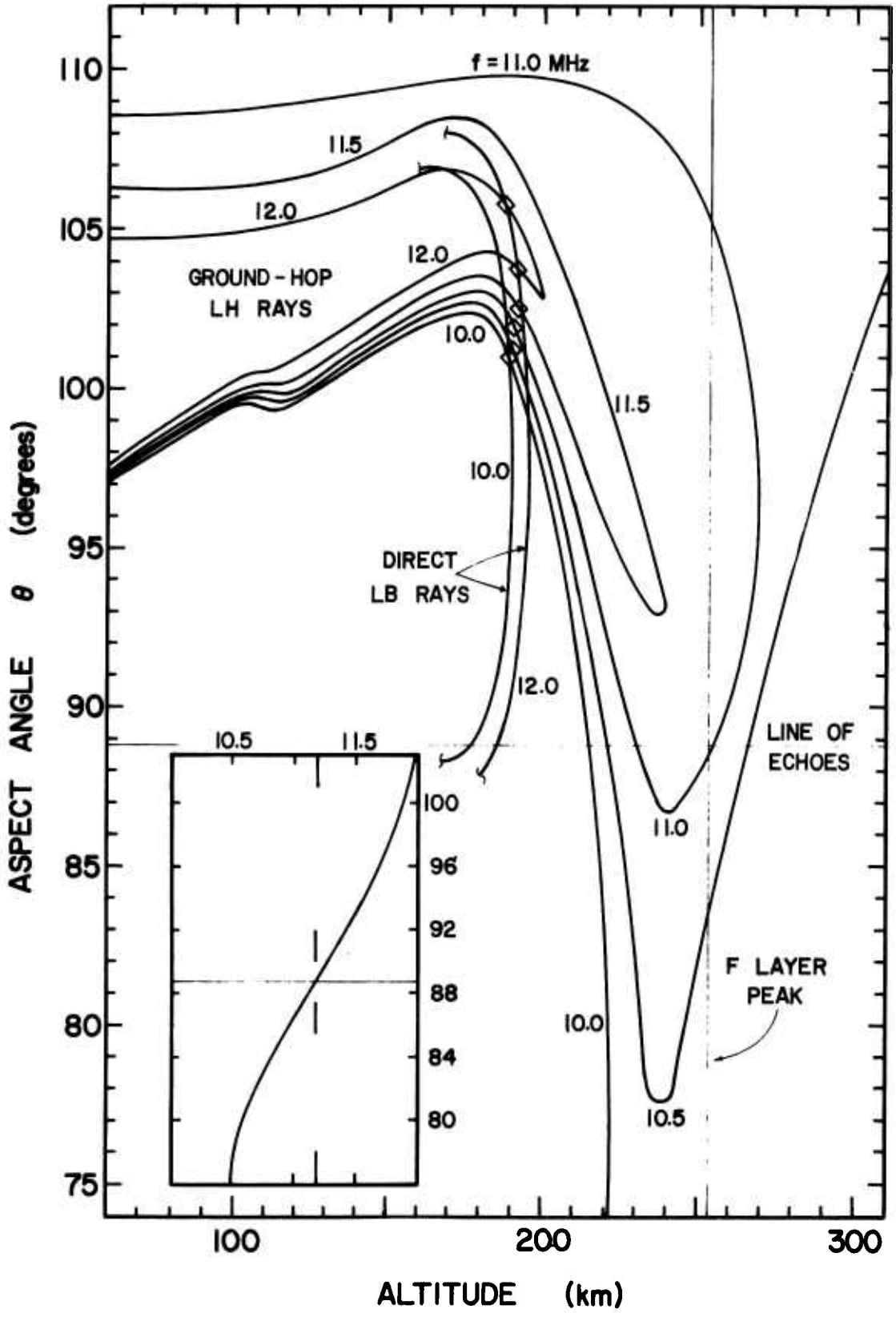

Fig. 5.15 The aspect-altitude diagram for the simulation of the secondary echo trace of 1715 MST, 5 January 1972.

The inverse cross-mode process, which couples energy from the direct mode arriving from LH to the ground-hop path to LB, should operate essentially as above. This follows from the observation of the previous section that, owing to the similarity of the propagation paths, the aspect-position loci for one sounder terminal are essentially the reflection, about the $\theta = 88.8°$ line, of the curves plotted for the other terminal.

5.6.4 Simulation of the primary echo using the echo-contour chart method

The simulation of the primary echo signature using the echo-contour method had a twofold purpose. The first was to study the effects arising from the finite horizontal extent of the disturbance and the probable target shape. The second was to assess the consequences of possible errors in positioning the model scattering volume.

The first attempt to construct the contour plots, using raytrace data generated for the aspect-altitude diagram, indicated that nearly three times the number of rays required by the former technique would have to be traced in order to define adequately the echo contours. Therefore, the more economical "Mark 3" raytrace procedure [Croft, 1969] was used. Because most of the refraction of the low-angle rays forming these echoes occurred in the Platteville vicinity, the Boulder $f_N(h)$ profile was adopted for the geoconcentric ionospheric model. Besides requiring less computer time, the data from this more elementary raytracing procedure allowed the consequences of neglecting ionospheric tilts, and therefore the need for three-dimensional raytracing, to be assessed.

The basic form adopted for the target model was an oblate spheroid, circular in plan view, and centered above Platteville at 1422 km range, 65° bearing from Lost Hills. Its centroid was placed at the 250 km altitude of the f layer peak, and its minor axis was directed vertically and assigned a length of 40 km so that the bottom of the disturbance would lie within the 207-214 km range previously determined. In accord with the 1 msec range extent of the observed echo, the equatorial diameter of the spheroid was fixed at 150 km. To represent the possible

upward expansion of the disturbance along the geomagnetic field lines, a circular field-aligned cylinder 150 km in diameter was fitted about the top of the spheroid. (This particular choice will be justified later.)

Knowing that the echo under consideration occurs at a predictable aspect, it was necessary only to trace the illuminating LH rays, noting if and where each ray achieved the echo aspect. These points then defined the echo contours. In the spherically-symmetric ionosphere modeled here, the raypaths propagate in great-circle planes, and it was therefore convenient to plot the echo contours in altitude-range coordinates in selected great-circle planes radiating from Lost Hills. Since the target spheroid subtends the sector bounded by the 62° and 68° azimuths in Lost Hills, adequate data coverage of the target vicinity was obtained by tracing in the 63°, 65°, and 67° azimuth planes. The echo contours were computed and plotted in the 360 km range interval centered about 1420 km. The geographic relationship of the range-azimuth loci thus defined to the target and the sounder terminals is shown in Figure 5.16.

In computing the echo origin points, full account was taken of the variation of the geomagnetic field orientation with latitude and longitude, using, as before, the Jensen and Cain [1962] model. The variation in altitude was neglected to simplify the echo search process, and the dip and declination values for the 250 km altitude were employed at all heights. Details of the echo contour computations are given in Appendix D.

The results of these computations in the 63°, 65°, and 67° LH azimuth planes are shown in Figure 5.17a,b,c, respectively. The curved horizontal lines and lenticular forms in the upper panel of each figure are the echo contours, as drawn for selected frequencies. The lightweight lines crossing these contours give the apparent echo range in 0.5 msec increments. Indicated by a light solid line is the section, in each plane, through the composite spheroid/cylinder model of the perturbed region. The top surface of the spheroid is depicted by a broken line.

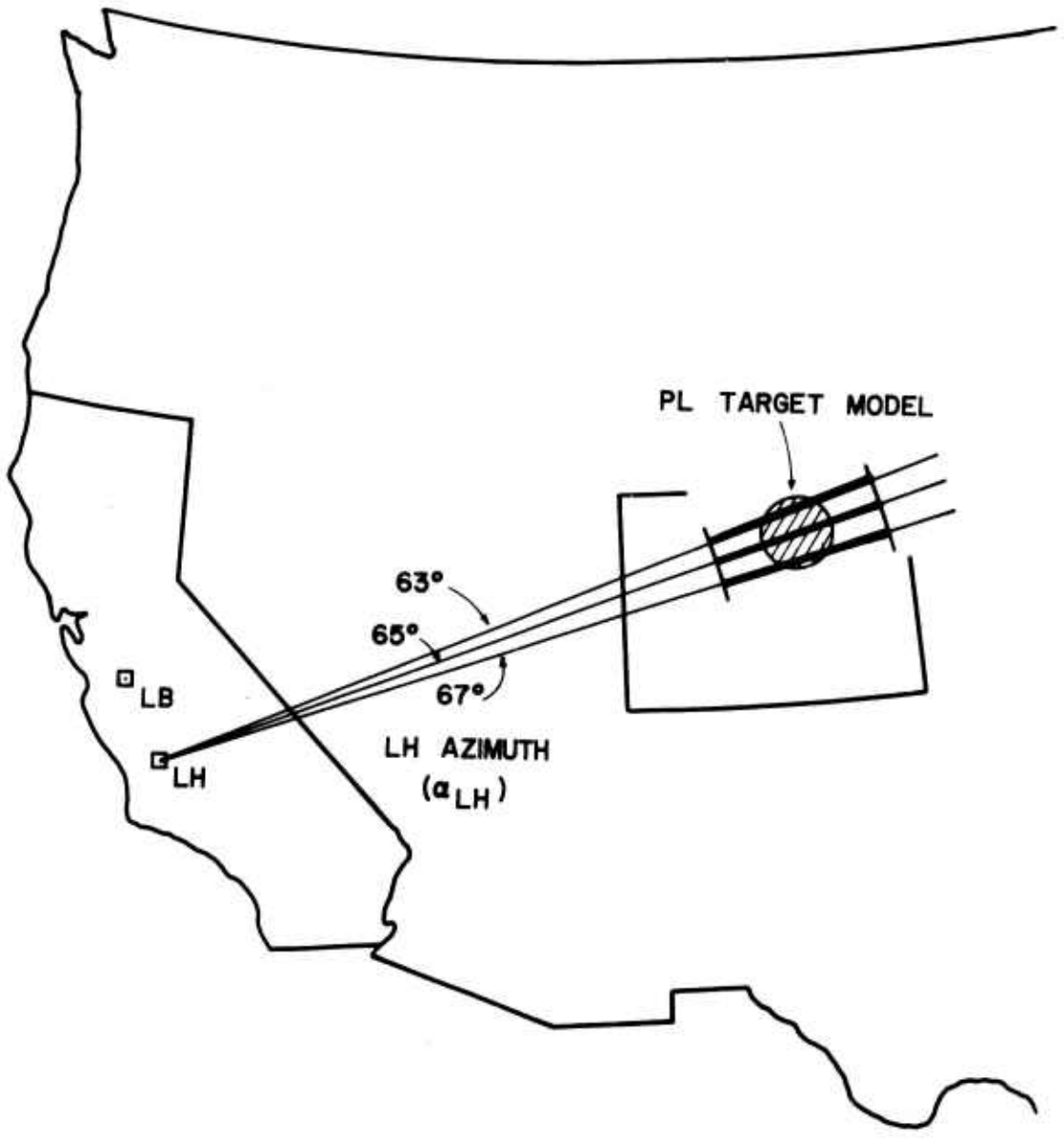

Fig. 5.16 The portions of the great-circle azimuth planes through LH (heavy lines) in which the echo contours of Figure 5.17 are plotted.

In the lower panels, the echo aspect θ_e and the associated LH echo ray elevation β_e are plotted against ground range. The θ_e curves show the near invariance with position of this quantity in the target vicinity; its functional dependence upon the range is nearly linear, with a regression of about -0.11°/100 km. The azimuthal variation is also small: -0.02°/degree azimuth (-0.08°/100 km at 1420 km range). In the absence of significant ionospheric tilts, θ_e and β_e

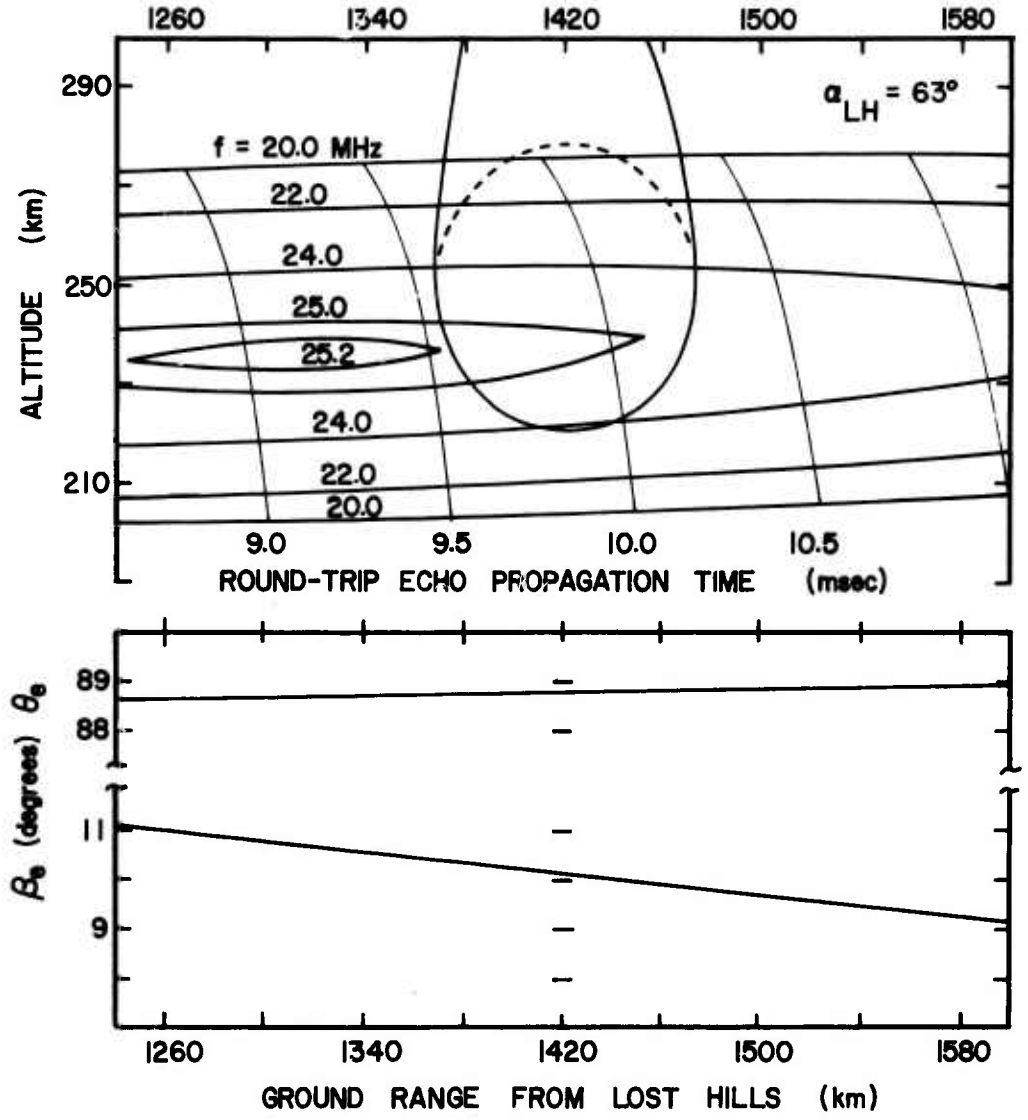

Fig. 5.17a The upper panel shows the echo contours for 1715 MST, 5 January 1972 in the vicinity of PL in the 63° azimuth plane through LH. The teardrop form in the center represents the section through the model target in this plane. The echo ray elevation and echo aspect are plotted as a function of range in the lower panel.

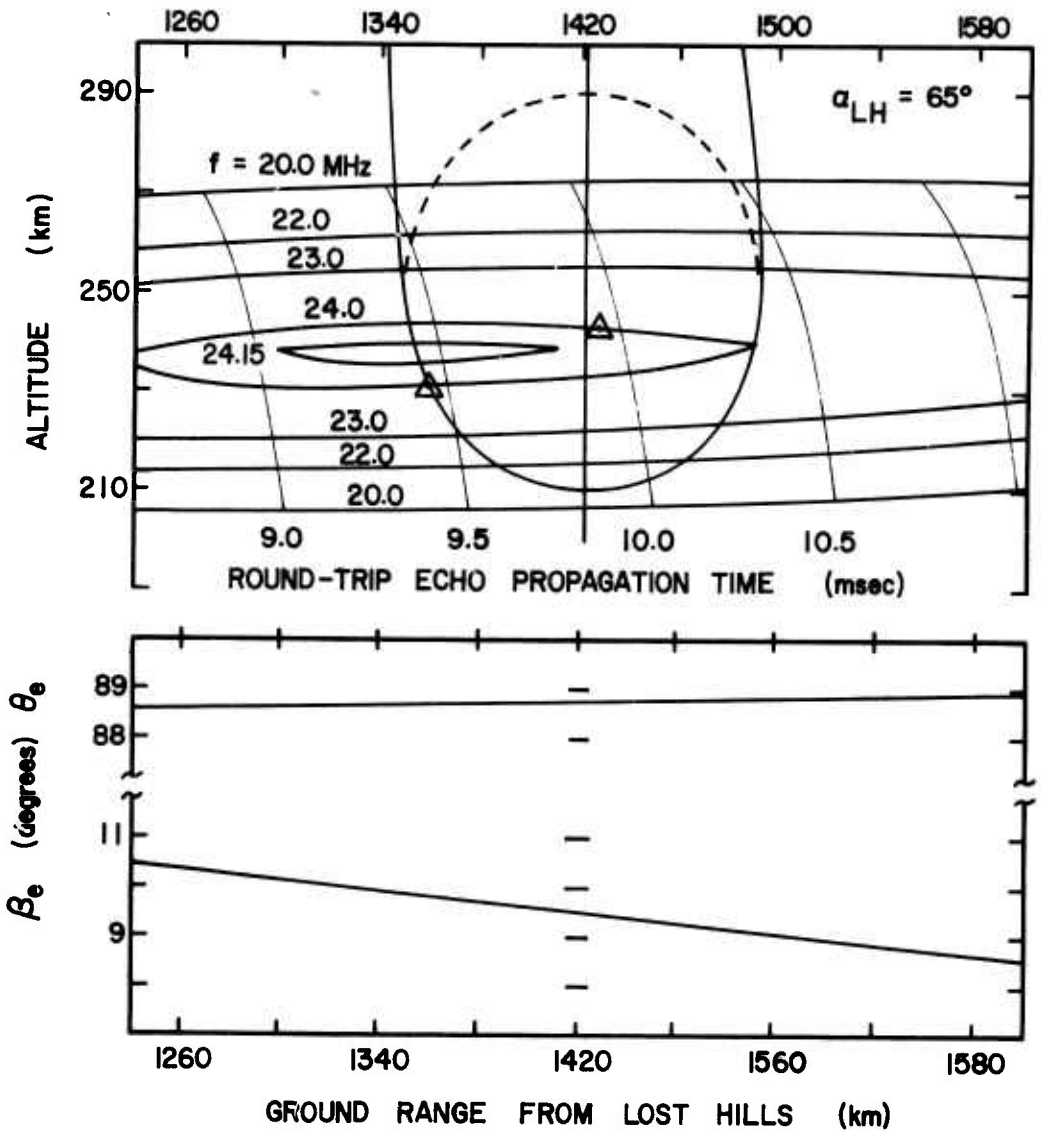

Fig. 5.17b The upper panel shows the echo contours for 1715 MST, 5 January 1972 in the vicinity of PL in the 65° azimuth plane through LH. The teardrop form in the center represents the section through the model target in this plane. The echo ray elevation and echo aspect are plotted as a function of range in the lower panel.

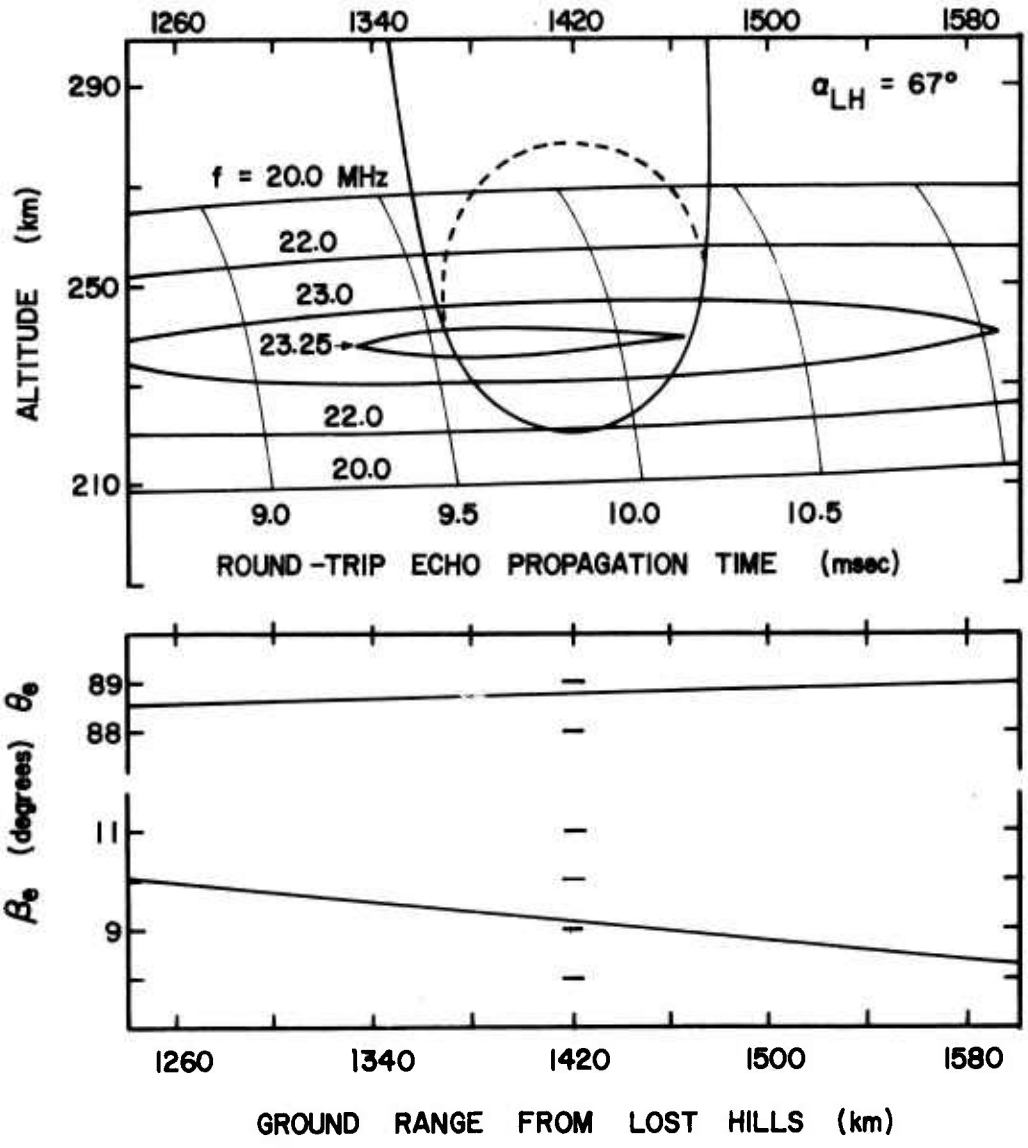

Fig. 5.17c The upper panel shows the echo contours for the 1715 MST, 5 January 1972 in the vicinity of PL in the 67° azimuth plane through LH. The teardrop form in the center represents the section through the model target in this plane. The echo ray elevation and echo aspect are plotted as a function of range in the lower panel.

depend only upon the relative geometry of the geomagnetic field and the radar terminal locations, and therefore need to be computed only once.

Inspection of the echo contour plots shows that, as before, the field-aligned echoes originate from two altitude levels at each frequency. These contour pairs approximate horizontal lines in the displayed range interval at the lower frequencies; but as the frequency rises, the successive pairs converge in altitude and eventually form closed lenticular islands which in turn progressively shrink into a point at an upper frequency limit. No contours exist beyond this limiting frequency, and it is thus seen that the geometrical echo conditions and the ionospheric propagation medium may combine to set an intrinsic upper cutoff frequency for the field-aligned echoes. (This phenomenon is peculiar to this radar geometry, however, and may not occur in other configurations.) This cutoff frequency varies with LH azimuth, increasing as the bearing becomes more northerly.

The open triangles on the 24.0 MHz echo contour of Figure 5.17b denote the upper and lower branch origin points for the LH ray launched at 4° initial elevation. Since a single ray can generate echo returns of both kinds, the upper and lower echo branches therefore cannot be unambiguously identified with the upper-ray and lower-ray ionospheric propagation modes.

It is now appropriate to examine the suitability of the field-aligned cylindrical cap fitted to the basic target spheroid. Since the sections through all capping figures intermediate between the spheroid and the cylinder, i.e., prolate hemi-spheroids of progressively greater major axis, must lie between the sections of these forms on Figure 5.17, the effects of the various choices may be determined by using the basic spheroid and the cylinder as limiting cases. Because the echoes of interest originate within the altitude range containing the spheroid, the actual upper extent of the model target is unimportant. In any event, the precise value to choose for this height, equivalently, for the major axis of the capping spheroid, is unclear. The second principal effect, a change of up to 0.2 msec in the apparent ranges in the 63° and 47° LH azimuth planes, does not significantly alter the end

results of this simulation. Therefore, although it is physically unrealistic, the semi-infinite cylinder cap is nevertheless a simple and a useful model representation for the upward expansion of the disturbance.

The one-dimensional target employed in the aspect-position diagram method is represented by the vertical line at 1422 km in Figure 5.17b. The upper cutoff frequency for this target is 24.1 MHz, as scaled from the contour (not shown) which just touches it. This is 1.2 MHz less than the corresponding value derived from the three-dimensional raytrace results. Since the intrinsic accuracies of the two raytracing programs are comparable, this difference is attributed to ionospheric tilt effects. Although the discrepancy between the tilt and no-tilt raytracing results is not serious in itself, the 24.1 MHz no-tilt cutoff is 2.4 MHz less than the observed extinction frequency, and this is a substantial difference. It is therefore concluded that the principal simulation of the extinction phenomenon should be carried out with the full three-dimensional raytracing approach when substantial ionospheric tilts are present, while the economical no-tilt technique may safely be used to extend these fundamental results.

Aside from widening the echo trace, the principal effect of the finite horizontal size of the disturbance is to increase the extinction frequency derived from the zero-extent case. Considering first the range extent only, Figure 5.17b shows that field-aligned reflections from within the 150 km diameter region occur at frequencies less than 24.2 MHz, which is 0.1 MHz greater than the cutoff determined for the target center. The cutoff frequency variation across the entire volume is 0.2 MHz. Since this result is a difference taken over a relatively small distance, it should not be significantly altered by the effects of ionospheric tilts. Consequently, the expected cutoff frequency error arising from the neglect of the target range extent is not significant.

On the other hand, the azimuthal extent of the disturbance exerts a strong influence upon the echo extinction frequency. Figure 5.17 shows that the cutoff frequency at the 1422 km range decreases from 25.1 MHz at the 62° azimuth to 23.3 MHz at 67°. Therefore, since the

echo is made up of contributions from all these azimuths, a better estimate of the no-tilt extinction frequency is 25 MHz. Including the range extent of the target in the 63° plane adds another 0.2 MHz. Consequently, the net effect of the finite horizontal size of the scattering region is to increase the simulated cutoff frequency from the 24.1 MHz value computed at the target center to 25.5 MHz. Since this represents a difference over a limited distance, it should apply also when moderate tilts are included. Consequently, the 25.3 MHz extinction derived from the three-dimensional raytrace results should be adjusted upward by approximately 1 MHz to allow for the azimuthal variation, and the resultant 26.3 MHz simulated cutoff is in very good agreement with the 26.5 MHz observed value.

The effects of errors in the positioning of the target may be examined in terms of their range and azimuth components. The principal result of a small misplacement in range is a 1 msec echo delay increase for each additional 150 km range increment; the upper extinction frequency is little changed. On Figure 5.17b (65° azimuth) it is seen that centering the target 100 km nearer to the transmitter increases the cutoff by less than 0.1 MHz, while the opposite displacement reduces it by about 0.2 MHz. Similar results are noted in the 63° and 67° planes. However, the effects of errors in the azimuth coordinate are more pronounced. Moving the target 2° southward (49 km at 1422 km range) lowers the extinction frequency by about 1 MHz, and a like northward repositioning causes a 1 MHz rise. The probable error in the estimated target position lies within these limits; therefore the simulated cutoff frequency may be uncertain to ±1 MHz or less.

The relative positions of the echo contours and the target sections shown in Figure 5.17 define a unique echo trace for each plane. Using the data contained in the echo-contour charts, these traces were synthesized and are presented in the upper three panels of Figure 5.18. In the bottom panel is shown the resultant echo signature formed by the superposition of these traces. There, the lightweight lines define the component parts of the individual constituent traces, and the bolder strokes outline the resultant echo signature. The nose of this signature (broken line) was reconstructed by extrapolating the data trend.

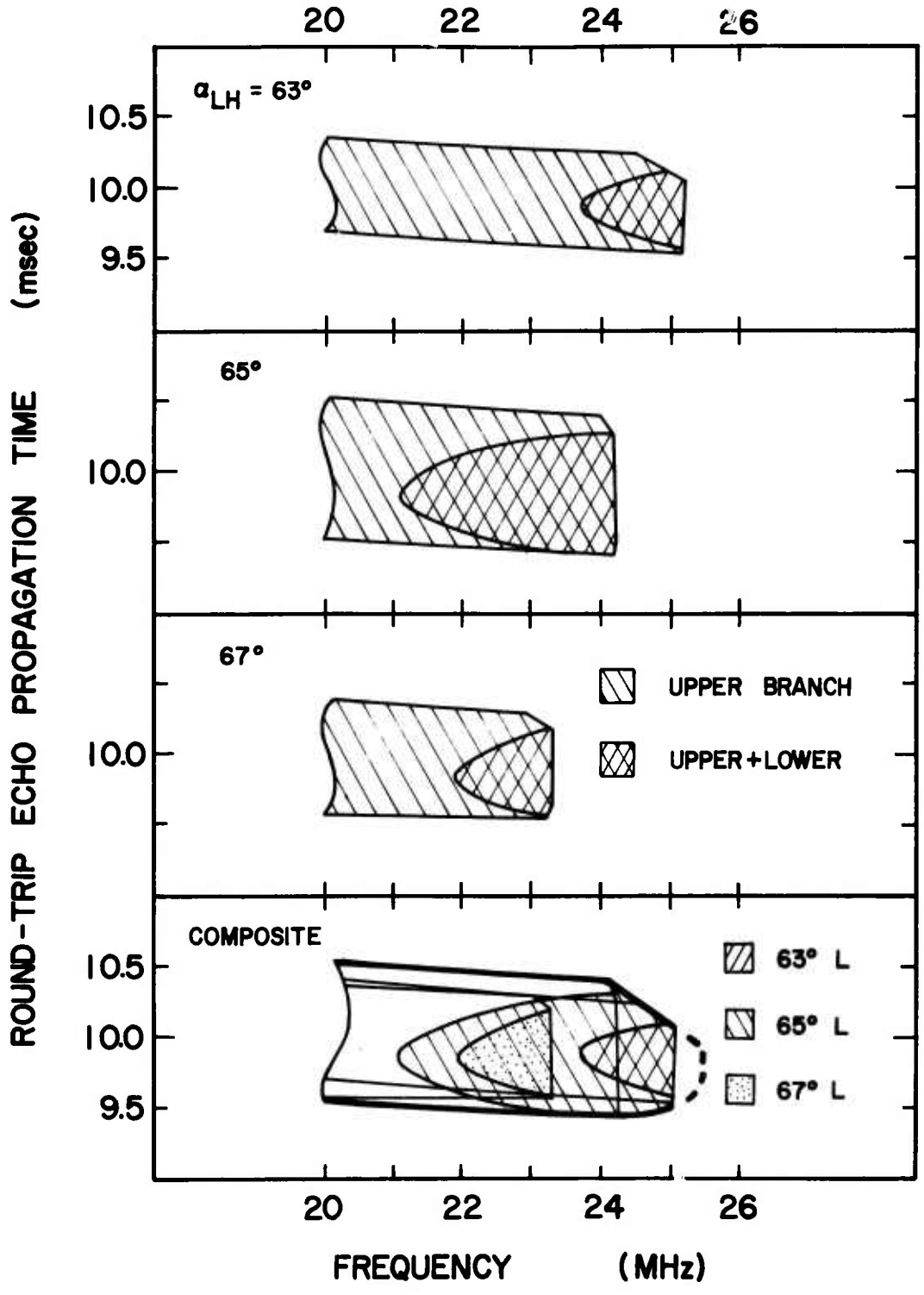

Fig. 5.18 In the top three panels are shown the component echo signatures in the specified LH azimuth planes. The bottom panel shows the composite signature formed by the superposition of these components. The lower-branch contributions are indicated on this composite trace by the hatched or stippled regions. The labels are to be interpreted: 63° L indicates the lower branch contribution from the 63° LH azimuth plane, etc.

The traces labeled "upper branch" and "lower branch" on Figure 5.18 correspond, as before, to the upper and lower (in altitude) echo contours. Considering first the upper branch, and using the trace derived from the 65° azimuth plane as the representative, Figure 5.17b shows that the contours from which this echo originates encounter the target model within its field-aligned cylinder component, and therefore view a scattering region of essentially constant range extent. The trace accordingly has a constant width. (This branch is not shown at frequencies below 20 MHz in Figure 5.18 because, as established previously, this propagation mode defocuses rapidly as frequency drops below this value.) On the other hand, the lower-branch contribution shows clearly the effects of the lower boundary of the spheroid. Following the lower echo contours in Figure 5.17b, it is seen that, after first contact with the target at 21 MHz, the field-aligned echoes occur throughout a progressively more extensive region as the radar frequency increases. These phenomena are qualitatively similar in all the azimuth planes.

The composite signature resembles closely the experimental trace. The total width is constant at 1 msec and, owing to the predominance of the upper-branch traces at the lower frequencies, the new synthetic trace reproduces the decreasing range-with-increasing-frequency trend of the experimental signature. This feature is due also in part to the rounded bottom of the model target, which has the effect of tapering off the otherwise constant-range lower-branch components at the lower frequencies, thus permitting the upper-branch traces to determine the form of the resultant signature.

The arrangement of the lower-branch contributions on the composite signature suggests a sequence of iso-intensity contours, and they may be generally regarded as such. As the frequency rises, the lower-branch signal from the 65° great-circle plane appears first and is subsequently augmented by the 67° contribution, which extinguishes at 23.3 MHz but is replaced by the 63° component. As a result, the strength of the simulated trace is enhanced substantially at its mid and high frequencies, which reproduces a like trend in the actual signature. This behavior of the lower-branch trace results from the combined effects of

the echo contour shifts with azimuth and the varying altitudes at which the sections through the lower surface of the target appear in each great-circle plane.

Finally, the upper right corner of the simulated trace appears to have been snipped off. This characteristic is present in each component signature. It represents a diminution of the maximum echo range near the upper cutoff, which in turn results from the progressive retreat through the scattering region of the rightmost tip of the shrinking lenticular island contours, as shown in Figure 5.17. Individually, these snips cover only a fraction of a megahertz. The extended frequency span of this feature on the composite trace is due to the repetition of the echo-contour retreat phenomenon at progressively higher frequencies in the successively more northerly azimuths. This snipped corner resembles closely a like feature on the experimental signature.

5.7 Summary and Conclusions

During the California-Platteville RTW experiment described in Chapter 1, the direct HF sweep-frequency backscatter returns from the man-made Platteville irregularity were monitored and recorded in an intensity-modulated range-frequency ionogram format. Having discovered that the characteristics of these echo signals were consistent with a model which combined the effects of the refracting ionospheric propagation medium with specular reflections from geomagnetically-aligned columns in the irregularity, a raytracing simulation of representative examples of these signatures was undertaken, both to confirm the field-aligned reflection mechanism, and to analyze the propagation effects accompanying such echoes under relatively controlled conditions.

This simulation was carried out using the echo signatures recorded in the late afternoon on 5 and 6 January 1972 as representative specimens. To take full account of ionospheric refraction, including tilts, the primary simulation was done using the Jones three-dimensional raytrace program in conjunction with a realistic ionosphere model derived from vertical-incidence sounding data. To locate all field-aligned echoes which might have occurred, the aspect-position diagram method was used first. After the basic nature of the echo mechanism was thus

established, a secondary technique, utilizing a simplified raytracing procedure and the echo-contour chart echo-location method, was employed to investigate the effects of the size and form of the target disturbance. The results of and the conclusions derived from this simulation effort are as follows.

It is concluded that the principal scattering mechanism in the Platteville artificial irregularity is specular reflection from columnar ionization density inhomogenieties aligned with the geomagnetic field. This inference derives from the high degree of agreement between the simulated and observed echo signatures and, in particular, from the close match between the simulated and the observed upper extinction frequencies of the echoes. It had been established earlier in the text that this extinction phenomenon is a fundamental property of ionospherically-propagated field-aligned echoes in this sounder-target configuration.

It was shown that the value of this extinction frequency is governed both by the distribution of ionization density in the ionosphere and by the position and horizontal dimension of the scattering region. In this instance, the ionization distribution was the stronger influence. While the echo-contour charts indicated that a displacement of 100 km in any direction about its mean location altered the computed extinction frequency by approximately 2 MHz, a comparison of the synthetic echo traces for the different days shows that a variation in the Boulder f_oF_2 from 4.4 MHz (1845 MST, 6 January 1972), to 5.5 MHz (1715 MST, 5 January 1972) caused a 6.3 MHz difference between the respective 19 MHz and 25.4 MHz extinction frequencies. A secondary echo signature was observed to commence and extinguish at relatively low frequencies (11.0-11.5 MHz). This is due to the rapid variation with frequency of the ray direction, combined with the comparatively steep incidence upon the ionosphere, of the signals propagated in the ground-hop mode which comprise this echo.

The expectation, based upon the generalized twin-path echo mechanism developed in Chapter 4, that field-aligned echoes might originate at a predictable echo aspect in a bistatic radar geometry, was verified under actual operating conditions, for echo signals propagated both

directly and via an intervening earth reflection. Using the aspect-position diagram, and accounting realistically for the late afternoon ionospheric tilts, this aspect was found to be invariant with altitude to within a 0.1° tolerance. The utility of the twin-path concept was demonstrated by using it to enable the construction of a set of echo-contour charts in the Platteville region, for the bistatic sounder. The echo signature derived from these charts, together with a reasonable representation of the form of the perturbed region, reproduced very closely the corresponding actual signature, further verifying the twin-path concept and the field-aligned reflection mechanism.

The simulated echo trace consisted of two distinct branches separated in apparent range. These were identified with field-aligned reflections occurring separately at different altitudes at the same ground distance, with the branch appearing at the greater apparent range (upper branch) originating at the higher altitude. The apparent range of the lower branch was nearly constant over frequency, while that of the upper branch decreased monotonically until the two components joined at the extinction frequency. It was found that the upper and lower echo branches cannot in general be identified respectively with the upper-ray and lower-ray ionospheric propagation modes.

Computations of the intensities of these echo components due to ionospheric focusing showed that the strength of the lower branch was nearly independent of the radar frequency, while the upper branch was rapidly attenuated as frequency declined. Both branches were of nearly equal intensity over the frequency interval beginning 2-4 MHz below the extinction frequency. Adopting the criterion, based upon the dynamic range of the Los Banos video display system, that defocusing attenuation greater than 15 dB renders the affected echo trace invisible, it was noted that the frequency at which this critical defocusing occurred on the simulated upper-branch traces was acceptably near the commencement frequency of the corresponding actual signatures.

The probable commencement frequency of each lower-branch trace was estimated by determining the frequency at which the altitude at which this trace originated coincided with the lower boundary of the disturbance. This onset frequency likewise agreed with the observed commencement.

The weight of the evidence indicates that the observed echo signature is comprised of both component branches near its extinction frequency, while the low-frequency portion of the trace is comprised of the upper echo branch. This view is favored by the declining range with increasing frequency trend of the actual signature, which matches well a like trend in the upper branch of the echo. How the interbranch transition might occur is indicated by the simulated traces derived from the echo contour charts (see Figure 5.17 and 5.18). These data show that, because of the variations in the relative position of the echo contours and the lower target boundary over the azimuthal extent of the disturbance, the contribution from the lower branch of the echo is initially quite small, but becomes progressively more important as the frequency increases. The upper branch, however, is suppressed at its lower end by refractive defocusing effects. Since this critical degree of defocusing occurs at a somewhat lower frequency than that at which the lower branch commences, the upper branch is expected to be the dominant echo component at the lower frequencies. It is therefore concluded that the upper branch comprises a significant part of the observed Platteville echo signature and that, in spite of the considerable refractive defocusing of this component at the lower frequencies, its importance should not be dismissed a priori in the study of field-aligned echoes in general.

(An additional circumstance, hitherto neglected owing to the emphasis placed on ionospheric effects in this study, is a possible null at the lowest elevation angles ($\beta_0 < 5°$) in the vertical-plane radiation patterns of the sounder antennas, due to an imperfect ground plane. This null has little effect on the upper branch of the echo, which originates in all cases from rays launched at elevations greater than 4°; however, it further attenuates the lower echo branch, which arises principally from rays launched with initial elevations less than 3°. This circumstance supports the above conclusion.)

APPENDIX A

THE CONSTRUCTION OF THE IONOSPHERIC MODEL EMPLOYED IN THE RAYTRACING SIMULATION OF THE PLATTEVILLE ECHOES

The fundamental data for the three-dimensional ionospheric model consisted of vertical-incidence ionograms recorded at Stanford (ST), Boulder (BL), and White Sands (WS) at the same time the echoes to be simulated were observed. These ionograms were first analyzed to obtain the vertical profile of the ionization density above each of the three ionosonde stations. An interpolation scheme was then employed to represent the ionization density and its gradients at points removed from these stations.

A.1 Derivation of the Vertical Profiles

The reduction of the ionograms to altitude profiles of the electron density was carried out by the staff of WDC-A, using a true height analysis technique invented by A. K. Paul [Paul and Wright, 1963; Paul, 1967; Howe and Mc Kinnis, 1967]. This method affords two prime advantages in this application. First, the resultant $N_e(h)$ profile has a continuous first derivative $dN_e(h)/dh$ within each ionospheric layer. This facilitates the numerical integration of the Haselgrove equations in the Jones raytrace program, reducing the number of integration steps required to maintain a given single-step error bound, thereby saving time and reducing the accumulated round-off error. Second, the procedure incorporates an effective means of estimating the true height at which the lowest ordinary mode frequency returned from a given layer was reflected. This furnishes a starting point for the main analysis and also provides a useful solution to the valley problem often encountered when the presence of two or more ionospheric layers is indicated.

This valley problem is illustrated by Figure A.1, in which the bold line represents the simple deep valley model profile of Herbert [1967]. The corresponding vertical ionogram trace appears in the inset. A characteristic of this profile is the plasma frequency depression, or valley, between the E and F layers. The presence of this valley is

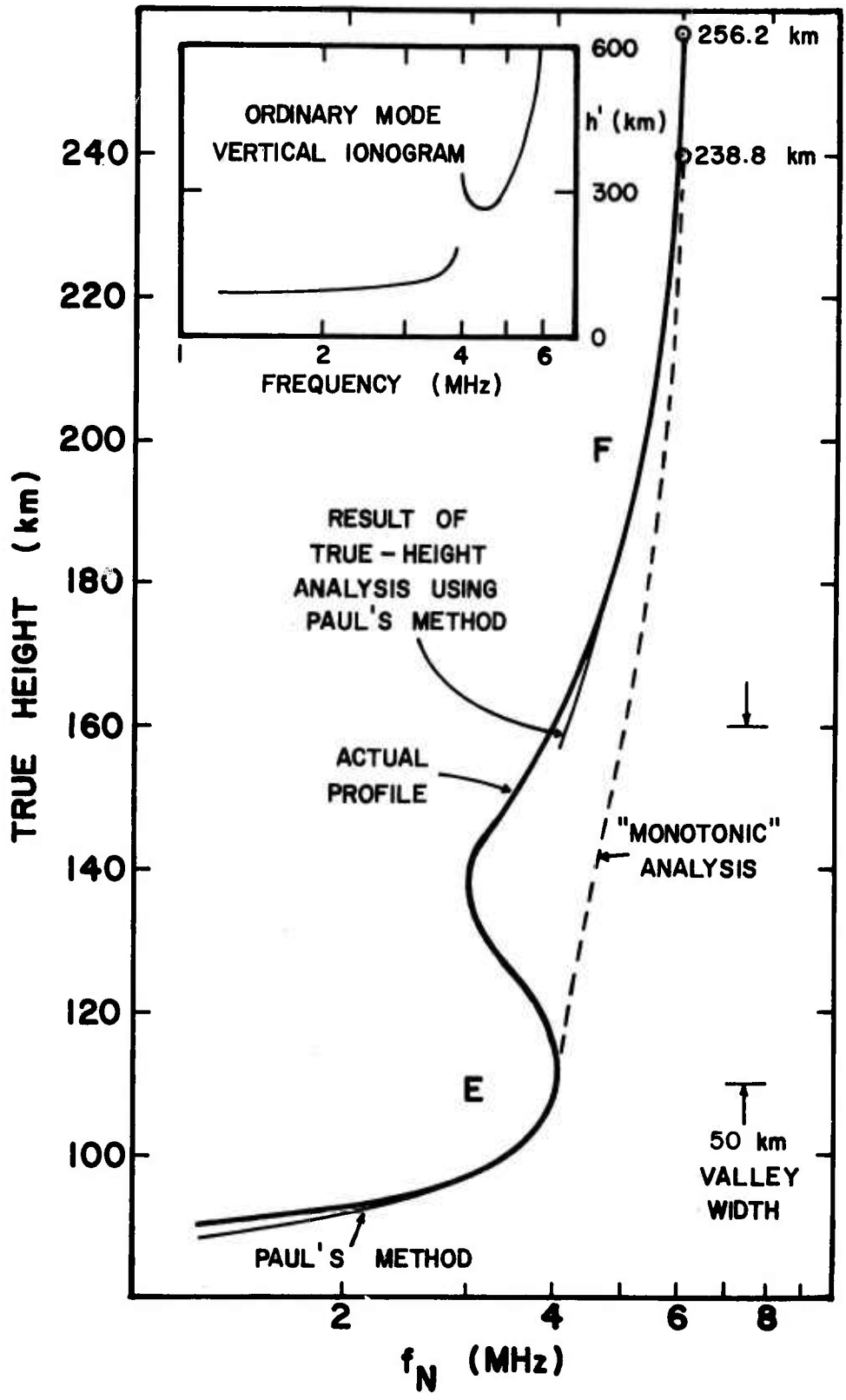

Fig. A.1 A two-layer model $f_N(h)$ profile and the results obtained from the true-height analysis of the corresponding vertical-incidence ionogram (inset) by two methods.

reflected in the discontinuity of the vertical ionogram trace at 4 MHz; such discontuities are also found on many actual ionograms (e.g., Figure 5.2).

To show the effects of this valley discontuity upon the true height analysis results, the synthetic ionogram of Figure A.1 was analyzed using both Paul's method and a "monotonic" analysis technique developed by Titheridge [1961]. Note that, while the E layer is accurately reconstructed by both methods, the F layer height given by the monotonic analysis is too small by the 50 km valley width at frequencies immediately above the E layer critical frequency. This error diminishes only to 16 km at the F layer critical frequency. Since rays traced through such a lowered profile will suffer an excessive downward deflection, the results obtained from monotonic analysis procedures are of doubtful utility in this simulation.

On the other hand, Paul's method allows the analysis process to be restarted whenever a new layer is indicated on the ionogram, so that an estimated minimum height is computed for each layer individually. Details of this restart procedure are given by Howe and McKinnis [1967]. The results of this method are indicated by the lightweight solid lines in Figure A.1, where a great improvement in accuracy is evident; the maximum error in the F layer analysis is less than 7 km.

The output data from the true-height analysis consisted of the true height values corresponding to selected values of f_N. To prepare this data for the raytracing ionospheric model routine, values of $N_e(h)$ were interpolated at consecutive integer kilometer values of h within the altitude ranges covered by the data, using second-degree interpolating polynomials identical to those employed in the true-height analysis algorithm.

There were two altitude intervals in which the $N_e(h)$ distribution could not be determined from the ionogram data. The first of these, the gap left at altitudes below the lowest true height derived from each ionogram, was resolved by fitting a model D region of the form given by Jones [1966, p. 89]. The parameters of this model were chosen to ensure continuity of $N_e(h)$ and $dN_e(h)/dh$ across the point where it was joined to the main profile. Values of $N_e(h)$ were tabulated at 1 km

altitude intervals down to the level at which $N_e < 10^{-4} cm^{-3}$, where the associated refractive index became indistinguishable from unity in the 7 figure arithmetic of the IBM 360 computer.

The second gap was in the altitude range from the peak of the E layer to the bottom of the F layer. This was a result of the valley problem discussed earlier; since no virtual height data could be obtained from within this valley region, it was impossible to reconstruct directly this segment of the profile. It was therefore necessary to develop a reasonable estimate of the intra-valley ionization distribution on the basis of the available data. This data consisted of the estimated column electron content of the valley and the values of N_e and $dN_e(h)/dh$ at the upper and lower valley boundaries, as derived in the true-height analysis, together with the virtual heights of the ordinary and extraordinary modes reflected immediately above the valley. Since these latter represent energy propagating throughout the valley region at frequencies nearest the plasma frequency of the valley ionization, they are the most strongly influenced by this ionization and therefore contain most of the available information regarding its distribution.

The problem of recovering this information and reconstructing the valley profile has been considered by Davies and Saha [1962], Saha [1964], and Wakai [1967]. The most effective available method (Wakai's) is to assemble a library of candidate valley profiles satisfying the electron content and boundary conditions and to determine, by ray-tracing, which of these most satisfactorily reproduces the original ionogram traces. However, as Saha points out, this trial and error procedure is laborious, expensive, and does not lead to a unique solution. This technique can indicate the overall character of the valley profile, but it cannot resolve its actual form.

Fortunately, it was not necessary here to reproduce the valley profile exactly; the results of Appendix E show that the raytracing final results at the frequencies of interest are little affected by gross changes in the E layer-valley profile. It was therefore decided to represent the intravalley $N_e(h)$ distribution by means of suitably

fitted polynomials, which are both economical and can use directly the available data.

The initial approach to this task utilized the five constraints obtained from the true-height analysis process: $N_e(h_L)$, $dN_e(h)/dh\big|_{h_L}$, $N_e(h_U)$, $dN_e(h)/dh\big|_{h_U}$, and $\int_{h_L}^{h_U} N_e(h)dh$, where h_L and h_U are the lower and upper altitude limits of the valley gap, to determine the coefficients of the quartic profile model

$$N_e(h) = ah^4 + bh^3 + ch^2 + dh + e \qquad (A.1)$$

While this procedure sometimes worked very well, it often failed to give an acceptable valley profile. The imposed constraints, particularly the integrated column density, frequently caused the quartic in (A.1) to assume the form of a large bulge in ionization density, with the maximum N_e in the bulge exceeding the E layer peak density. When this happened, the column density constraint, judged the least necessary, was abandoned; and an intra-valley profile preserving the continuity of $N_e(h)$ and $dN_e(h)/dh$ was estimated as described below.

In this process, the profile segments flanking the valley were first plotted on a semi-logarithmic scale of h versus $\log N_e(h)$, and these segments were then joined by fairing a curve through the valley by hand. Estimates of N_e and h at the valley minimum were then scaled from this curve, and a cubic polynomial segment was fitted from this point to the known E and F profiles to define, respectively, the upper E and the lower F profile segments. The polynomial coefficients were evaluated by requiring that $N_e(h)$ and $dN_e(h)/dh$ be continuous across the segment boundaries, and that $dN_e(h)/dh = 0$ at the valley minimum. The resultant $N_e(h)$ valley profile was tabulated at 1 km height intervals.

Another profile gap existed in the region above the F layer peak, which cannot be probed by ground-based radio ionosondes. However, a preliminary raytracing indicated that the field-aligned reflections of interest would occur predominantly in the bottomside F region; therefore, although some topside profile data was available from satellite-borne

ionosondes, notably Alouette I [e.g., Chan et al., 1966], it was not attempted to use this complete data. Rather, it was noted that the tables of $N_e(h)$ published by Chan et al. showed a gradual decrease in electron concentration immediately above the F layer peak, where the preliminary raytracing indicated that the topside field-aligned reflections would originate. This feature is reproduced well by a Chapman model profile, and the topside ionosphere was therefore modeled by a Chapman layer joined to the F layer peak, using an estimated scale height value derived in the true-height analysis process.

A.2 The Interpolation Scheme

The Jones raytrace program may require the ionization density to be computed at any point within the model propagation medium, so that the ionospheric model must furnish a continuous representation of N_e in latitude, longitude, and height. It is also desirable that the interpolation scheme fit the given data as smoothly as possible and, for economy, it should be simple.

The input data to the interpolation routine consisted of about 200 electron density values tabulated at 1 km height intervals at the three ionosonde locations, so that it was necessary to interpolate both in altitude and in geographic position.

Interpolation in altitude will be considered first. Owing to the great number of altitude coordinate points tabulated, the classical Langrangian interpolating polynomial was unsuitable. Instead, the profiles were represented by piecewise-continuous functions suitably fitted between adjacent pairs of data points. As supplied by ESSA, the Jones raytrace program included a subroutine which employed a piecewise cubic polynomial of the form

$$N_e(h) = \alpha h^3 + \beta h^2 + \gamma h + \delta \qquad (A.2)$$

to interpolate tabular ionospheric data in each altitude interval between adjacent data points. The coefficients were computed by requiring that $N_e(h)$ and $dN_e(h)/dh$ given by each polynomial segment match the respective tabular values at the endpoints of the appropriate interval. While this method generally worked well, the author had

traced certain errors which arose in a previous raytracing study to shortcomings in this scheme.

It was found that accuracy was greatly improved by using the cubic natural spline (CNS) interpolating function, which fits piecewise cubic polynomials of the form

$$N_e(h) = \alpha t^3 + \beta t^2 + \gamma t + \delta \qquad (A.3)$$

where $t = t(h)$ is the difference between the altitude at which the interpolated value is required and the next lower tabular altitude. The coefficients are evaluated by requiring that the interpolated and tabulated values match at the interval endpoints, and that the first and second derivatives be continuous from one tabular interval to the next. The cubic natural spline is the smoothest of the piecewise cubic interpolating functions [Hamming, 1973].

A linear interpolating scheme was employed in the horizontal dimension. Using CNS interpolation, a value of N_e was specified at any altitude h at each of the three ionosonde stations. These data uniquely determine, at that altitude, a two-dimensional interpolating function of the form

$$N_e(h, \lambda, \Lambda) = a\lambda + b\Lambda + c \qquad (A.4)$$

where λ and Λ are, respectively, the colatitude and longitude coordinates. In a modification of this concept, expressions of the form (A.4) were employed to interpolate the coefficients α, β, γ, δ of the cubic natural spline functions fitted to the three $N_e(h)$ profiles. It was first required that these profiles be tabulated at a common set of heights h_i, $i = 1, \cdots, n$. Within each altitude interval bordered by h_k and h_ℓ, the coefficients $a_{\alpha,k}$, $b_{\alpha,k}$, $c_{\alpha,k}$, $a_{\beta,k}$ $\cdots$ were then computed by solving the systems of equations.

$$\begin{bmatrix} \lambda_{ST} & \Lambda_{ST} & 1 \\ \lambda_{BL} & \Lambda_{BL} & 1 \\ \lambda_{WS} & \Lambda_{WS} & 1 \end{bmatrix} \times \begin{bmatrix} a_{\psi,k} \\ b_{\psi,k} \\ c_{\psi,k} \end{bmatrix} = \begin{bmatrix} \psi_{ST,K} \\ \psi_{BL,k} \\ \psi_{WS,k} \end{bmatrix} \qquad (A.5)$$

where λ_{ST} and Λ_{ST} are the colatitude and longitude of the ST ionosonde; and ψ represents, in the successive applications of (A.5), α, β, γ, and δ.

These coefficients were computed once and for all for each ionospheric model. They were then used in the raytrace program to reconstitute the cubic natural spline vertical interpolating function at any point (λ,Λ) by means of the expressions

$$\begin{bmatrix} \alpha_k \\ \beta_k \\ \gamma_k \\ \delta_k \end{bmatrix} = \begin{bmatrix} a_{\alpha,k} & b_{\alpha,k} & c_{\alpha,k} \\ a_{\beta,k} & b_{\beta,k} & c_{\beta,k} \\ a_{\gamma,k} & b_{\gamma,k} & c_{\gamma,k} \\ a_{\delta},k & b_{\delta,k} & c_{\delta,k} \end{bmatrix} \times \begin{bmatrix} \lambda \\ \Lambda \\ 1 \end{bmatrix} \qquad (A.6)$$

and N_e was finally evaluated from the spline

$$N_e\ (h,\ \lambda,\ \Lambda) \ = \ \alpha_k t^3 + \beta_k t^2 + \gamma_k t + \delta_k \qquad (A.7)$$

where $t = h - h_k$.

It is shown in section A.3 that the $N_e(h,\ \lambda,\ \Lambda)$ distribution thus defined is continuous and possesses continuous first and second derivatives.

The linear interpolation scheme is formulated in a cartesian coordinate system, and some distortion results when this method is transferred directly to the surface of the spherical earth. While orthogonal conformity is maintained by specifying λ and Λ in angular measure, some deformation occurs because geocentric cones corresponding to parallels of latitude are substituted for the planes represented by constant values of λ in (A.6). This distortion becomes progressively more severe as the poles of the spherical coordinate system are approached, and the scheme is useless at the pole itself. However, since the structure of the actual ionóspheric F region tends to be organized along the parallels of the geomagnetic coordinate system [Davies, 1965], this deformation may actually be exploited to improve the representation of this layer by defining the interpolation in terms of geomagnetic coordinates. Thus a compromise was adopted.

The amount of the distortion was minimized by defining a new spherical coordinate system whose equator passed through the White Sands ionosonde, and a degree of geomagnetic symmetry was imposed by requiring that the meridian of this new system which passed through Platteville must coincide with the geomagnetic meridian there. Accordingly, the north pole of this new system was placed at 55.6° north geographic latitude, 51.1° east longitude.

A.3 The Continuity of the Interpolated Electron Density

It is the purpose of this section to show that the $N_e(h, \lambda, \Lambda)$, dN_e/dh, and d^2N_e/dh^2 computed via the interpolated spline coefficients method are continuous function of space throughout the ionospheric model.

Reviewing the developments of the preceding section, let the three $N_e(h)$ base profiles be tabulated at the common altitudes h_i, $i = 1,2,\ldots,n$. The geographic colatitude, longitude positions of these profiles are $(\lambda_{ST}, \Lambda_{ST})$, $(\lambda_{BL}, \Lambda_{BL})$, and $(\lambda_{WS}, \Lambda_{WS})$. At a given height h within the altitude interval between h_k and h_ℓ, where k and ℓ are arbitrary, N_e is given by (A.6) and (A.7).

Now consider the k-th and ℓ-th altitude intervals beginning at h_k and h_ℓ, respectively. At a given point (λ, Λ) the expressions for $N_e(t)$ in each interval are, from (A.7)

$$N_{ek} = \alpha_k t_k^3 + \beta_k t_k^2 + \gamma_k t_k + \delta_k \qquad \text{(A.8a)}$$

$$N_{e\ell} = \alpha_\ell t_\ell^3 + \beta_\ell t_\ell^2 + \gamma_\ell t_\ell + \delta_\ell \qquad \text{(A.8b)}$$

Since α_k through δ_k differ from α_ℓ through δ_ℓ, the expected location for a discontinuity in $N_e(h)$ is at the interval boundary, where $h = h_\ell$, $t_k = t$, $t_\ell = 0$. Substituting these into (A.8) gives

$$N_{ek} = \alpha_k t^3 + \beta_k t^2 + \gamma_k t + \delta \qquad \text{(A.9a)}$$

$$N_{e\ell} = \delta_\ell \qquad \text{(A.9b)}$$

Since the expression (A.9) implicitly contain expressions of the form (A.5), they may be written in the form

$$N_{ek} = \zeta_k \lambda + \eta_k \Lambda + \theta_k \tag{A.10a}$$

$$N_{e\ell} = \zeta_\ell \lambda + \eta_\ell \Lambda + \theta_\ell \tag{A.10b}$$

and

$$N_{e\ell} - N_{ek} = \zeta' \lambda + \eta' \Lambda + \theta' \tag{A.10c}$$

where

$$\zeta' = \zeta_\ell - \zeta_k, \quad \eta' = \eta_\ell - \eta_k, \quad \theta' = \theta_\ell - \theta_k \tag{A.10d}$$

and

$$\zeta_k = a_{\alpha,k}\, t_k^3 + a_{\beta,k}\, t_k^2 + a_{\gamma,k}\, t_k + a_{\delta,k}$$

$$\eta_k = b_{\alpha,k}\, t_k^3 + a_{\beta,k}\, t_k^2 + a_{\gamma,k}\, t_k + a_{\delta,k} \tag{A.10e}$$

etc.

At the profile tabulation points we have $N_{ek} = N_{e\ell} = N'_{e\ell}$, where $N'_{e\ell}$ is the tabulated value of N_e at $h = h_\ell$. This continuity is a fundamental constraint imposed in calculated the interpolating function coefficients. Consequently,

$$\zeta' \lambda_{ST} + \eta' \Lambda_{ST} + \theta' = 0 \tag{A.11a}$$

$$\zeta' \lambda_{BL} + \eta' \Lambda_{BL} + \theta' = 0 \tag{A.11b}$$

$$\zeta' \lambda_{WS} + \eta' \Lambda_{WS} + \theta' = 0 \tag{A.11c}$$

Since no member of λ_{ST}, λ_{BL}, λ_{WS} or Λ_{ST}, Λ_{BL}, Λ_{WS} is zero, these expressions require that $\zeta' = \eta' = \theta' = 0$. Therefore, from (A.10c)

$$N_{e\ell} - N_{ek} = 0 \tag{A.12}$$

and the interpolated N_e is continuous over altitude.

Its continuity over λ and Λ is assured by the continuous linear interpolation in these variables; and continuity within any altitude

interval not containing a tabular altitude is ensured by the null result of (A.10c) when $k = \ell$.

Since $dN_e/dh = 3\,\alpha t^2 + 2\,\beta t + \delta$, and given that dN_e/dh is required to be continuous across the profile tabular points by the definition of the cubic natural spline function, the continuity of the derivative follows immediately from the above development. It is likewise guaranteed that $d^2N_e/d_H{}^2 = 6\,\alpha t + 2\beta$ is also continuous.

APPENDIX B

JUSTIFICATION FOR THE NEGLECT OF COLLISIONAL AND MAGNETOIONIC EFFECTS IN THE RAYTRACING COMPUTATIONS

Because the radar frequencies considered in this investigation are very much greater than the electron-neutral collision frequency in the ionosphere, these collisions have an insignificant influence upon the ray trajectories, but act mainly to dissipate a portion of the signal energy. This non-deviative absorption is most efficiently treated using empirical formulas (e.g., Croft [1967b]).* Using the formula given by Croft, the magnitude of this absorption was computed for the horizon rays on the California-Platteville path for the times when the echoes to be simulated were recorded. The results, which define the upper limits of absorption for a single traversal of the D region, are listed at representative radar frequencies in Table B.1. Clearly, the absorptive effects are small, and a complete neglect of collisional effects is justified.

TABLE B.1 Absorption in dB of the Horizon Ray during a Single D Region Traversal at the Dates and Times Indicated.

			Radio Frequency (MHz)				
Time	χ	S	10	15	20	25	30
1715 MST 5 Jan.	90°	54	1.87	0.90	0.53	0.35	0.24
1845 MST 6 Jan.	100°	55	0.21	0.10	0.06	0.04	0.03

The magnetoionic propagation effects arise from the presence of the geomagnetic field. They are more difficult to assess without raytracing. With their inclusion, the ionosphere becomes an anisotropic, birefringent

---

* The formula is

$$\text{Absorption (dB)} = \frac{310\ (1 + 0.0037S)\ (\csc \zeta)\ (\cos 0.88\chi)^{1.3}}{(f + f_H)^2}$$

where ζ is the elevation angle of the ray at the 100 km altitude, S is the running-average sunspot number, χ is the solar zenith angle, and f and f_H are respectively the radar and electron gyrofrequencies in MHz.

medium with two characteristic refractive indices which are functions of the wavenormal direction as well as of ray position. As a result, an incident wave is resolved into the characteristic ordinary (O) and extraordinary (X) modes, which propagate independently with different polarizations and group and phase velocities. The net electromagnetic field at any point is the resultant of the O and X contributions, and extensive raytracing of the two modes, each requiring separately the execution of a complicated raytracing algorithm and the concurrent evaluation of an involved refractive index expression, is necessary to determine this field. Such raytracing tasks have been undertaken to study phenomena specifically imputed to magnetoionic effects, [e.g., Barnum, 1973]; however, it is desirable to avoid the additional labor and expense of a full magnetoionic raytrace effort if at all possible.

Of prime interest in this simulation are the ray trajectories and the resulting wavenormal orientations at the target. Fortunately, the variances in these parameters, as computed for the O and X components of a given transmitted ray and for the same ray neglecting the geomagnetic field, diminish as the radio frequency becomes very much greater than the gyrofrequency. Since the quantity f/f_H varies from about 7 to nearly 20 over the 9-27 MHz frequency band of interest, it is reasonable to expect that the errors arising from the neglect of magnetoionic effects will be comparable to those due to the inherent imprecision of the ionospheric model. Therefore, an empirical approach was adopted. If the simulation results obtained using the no-field formulation were found to reproduce the observations acceptably well, this formulation was to be accepted. If, however, otherwise inexplicable inconsistencies were noted, a more complete study of the magnetoionic effects was to be conducted. This latter course fortunately proved unnecessary.

APPENDIX C

THE DERIVATION OF THE FOCUSING INDEX FOR THE ILLUMINATING RAYS

Consider a set of raypaths originating from a ground-based transmitter and uniformly spaced in elevation angle β_0, as shown in Figure C.1. It is desired to find a metric index of the relative power flux density due to this radiation field as a function of altitude at a given ground range from the transmitter.

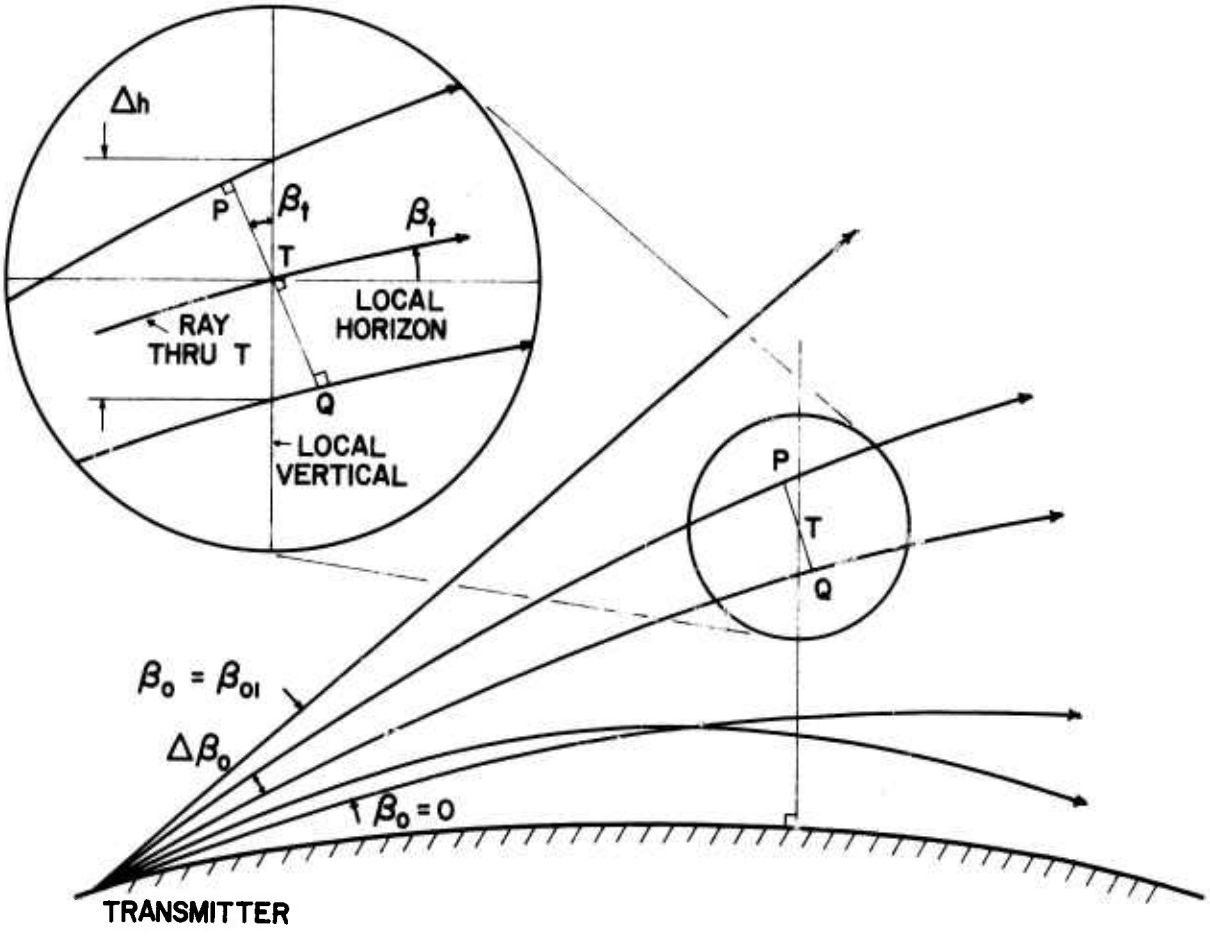

Fig. C.1 The raypath geometry and the parameters used in computing the degree of refractive focusing of the field-aligned echo signals.

Therefore, let T be a representative target point located at this range, and let PTQ be a segment of the section through an eikonal surface corresponding to this family of ray trajectories. Each adjacent pair of these raypaths, together with a pair of azimuthal sector boundary planes, defines a flux tube which is considered to channel a power flux of time-average strength $W(\beta_0)$. For simplicity, let the width of this azimuthal sector be chosen so that the eikonal surface subtended at T is of unit dimension normal to the plane of Figure C.1. Therefore, since PTQ is bounded by the flux tube containing T, the power flux crossing T is $W(\beta_{0T})$, and an appropriate index F of the average flux density in the neighborhood of T is

$$F = W(\beta_{0T})/S \tag{C.1}$$

where S is the length of the arc PTQ.

For convenience, assume that a total power W is radiated uniformly between elevations $\beta_0 = 0$ and $\beta_0 = \beta_{01}$, which interval contains all raypaths of interest. Hence, any given flux tube carries a power flux $W(\beta_0) = W(\beta_{0T}) = W \cdot \frac{\Delta\beta_0}{\beta_{01}}$, and

$$F = \frac{W}{\beta_{01}} \cdot \frac{\Delta\beta_0}{S} \tag{C.2}$$

Allowing $\Delta\beta_0$ to become arbitrarily small and referring to the inset of Figure C.1, we note that $S \approx \Delta h/\cos\beta_T$. Thus

$$F \approx \frac{W \cos\beta_T}{\beta_{01}} \cdot \frac{\Delta\beta_0}{\Delta h} \tag{C.3}$$

Finally, passing to the differential, we have

$$F = \frac{W \cos\beta_T}{\beta_{01}} \left(\frac{dh}{d\beta_0}\right)^{-1} \tag{C.4}$$

In this particular case, F will be computed only for the echo-producing raypaths. Since this occurs at a constant β_T, $\cos\beta_T$ is a constant. In addition, both W and β_{01} may be assigned constant

values, and thus all terms outside the parentheses in (C.4) may be removed by the normalization $F = F/F'$, where F' is an arbitrarily chosen value of F. Here, F' will be defined to be the F corresponding to the lower ray echo at 10 MHz in the particular model ionosphere, and the focusing index is

$$F = \left(\frac{dh}{d\beta_0}\right)^{-1} \Bigg/ \left(\frac{dh}{d\beta_0}\right)^{-1}_{10L} \tag{C.5}$$

APPENDIX D

THE CONSTRUCTION OF THE ECHO CONTOURS

Since the field-aligned echoes considered here have been shown to occur via the twin-path mechanism studied in Section 4.2, all such echoes must originate at an echo aspect angle θ_e given by

$$\cos \theta_e = \cos I \cos \beta_e \cos \gamma_t - \sin I \sin \beta_e \qquad (D.1)$$

where I is the geomagnetic dip, γ_t is the geomagnetic bearing at the target of the ray arriving from the transmitter, and β_e is the echo ray elevation. The magnitude of β_e is given by

$$\tan \beta_e = \frac{1}{2} (\cos \gamma_t + \cos \gamma_r) \operatorname{ctn} I \qquad (D.2)$$

where γ_r is the geomagnetic bearing at the target of the ray arriving from the receiver site.

Since, in the spherically-symmetric ionosphere model used in conjunction with the "Mark 3" raytrace program, the rays follow great-circle paths, it is possible to compute in advance the true geographic bearings of the rays from LH and LB at any given point. Thus, neglecting the variation with altitude of I and D, the quantities γ_t, γ_r, and β_e may also be computed once and for all at any point prior to the actual raytracing.

As a result, the echo-detection process becomes a search for a given ray elevation. It is not necessary to find the actual value of θ_e, although it may be computed as an auxiliary quantity. Since the value of β_e is the same for both the transmitter and the receiver rays comprising the echo, it is not required to trace both sets of raypaths. Because it seems more natural to deal with the illuminating rays when hunting echo reflection points, the rays from LH were selected for raytracing.

The echo contours were therefore plotted in selected great-circle planes radiating from Lost Hills, and β_e was accordingly specified as a function of the ground range ρ from LH in each of these planes.

The relevant expressions for this sounding configuration are, in addition to (D.2)

$$\gamma_t = \mathrm{Tan}^{-1}\left[\frac{\sin\alpha \sin\delta \sin\lambda_t}{\cos\delta \cos\lambda_E - \cos\lambda_t}\right] - D \qquad (D.3)$$

$$\gamma_r = \mathrm{Tan}^{-1}\left[\frac{\sin\lambda_r \sin\lambda_E \sin(\Lambda+\Lambda_E)}{\cos\delta_r \cos\lambda_E - \cos\lambda_r}\right] - D \qquad (D.4)$$

where λ_t and λ_r are respectively the colatitudes of LH and LB; α is the azimuth, measured clockwise from true north at LH, defining the great-circle plane in which the echoes are being sought; $\delta = \rho/R_E$, where R_E is the radius of the earth, and D is the geomagnetic declination at range ρ, bearing α from LH. The remaining quantities are defined as follows.

$$\Lambda = |\text{longitude of LH} - \text{longitude of LB}| \qquad (D.5)$$

$$\Lambda_E = \mathrm{Tan}^{-1}\left[\frac{\sin\alpha \sin\delta \sin\lambda_t}{\cos\delta - \cos\lambda_t \cos\lambda_E}\right] \qquad (D.6)$$

$$\cos\delta_r = \cos\lambda_r \cos\lambda_E + \sin\lambda_r \sin\lambda_E \cos(\Lambda+\Lambda_E) \qquad (D.7)$$

$$\cos\lambda_E = \cos\lambda_t \cos\delta + \sin\lambda_t \sin\delta \cos\lambda \qquad (D.8)$$

In practice, the repeated evaluation of these formulas was avoided by precomputing β_c in each azimuth at 50 km steps within the 1150 to 1750 km range interval where the echo points were sought. A cubic natural spline interpolating function was then fitted to these data to represent $\beta_c(\rho)$. Since the actual variation of β_c with range is nearly linear (see lower panels of Figure 5.17), this approximation was considered adequate.

With the $\beta_c(\rho)$ function thus determined, another function, $\beta(\rho)$, may be defined as ray elevation along each raypath traced, and the process of echo detection is then mathematically equivalent to solving $\beta(\rho) = \beta_c(\rho)$. Since the raytrace algorithm develops the raypath as a sequence of steps, giving ρ and β at each increment, the search for

the event $\beta = \beta_e$ may be readily incorporated into the raytrace program. Letting $\{\beta_1, \rho_1, \beta_{e1}\}$ and $\{\beta_2, \rho_2, \beta_{e2}\}$ represent the values of the respective quantities at the start and finish of a raytracing step, the product $(\beta_1-\beta_{e1}) \times (\beta_2-\beta_{e2})$ will be negative if $\beta = \beta_e$ anywhere within the interval and positive otherwise. In the latter event, the raytrace proceeds with its next step; in the former, the ground range at which the echo occurred is determined by linear interpolation. Two subsequent linear interpolations, using ρ at the independent variable, are then performed to obtain the echo altitude and the apparent radar range, and raytrace is resumed. This process is repeated through the range interval of interest, and is terminated when the ray goes either beyond 1750 km range, or above the 500 km altitude. The resultant $\{\rho_E, h_E\}$ echo points corresponding to each radio frequency were then plotted and joined by smooth curves to define the echo contours of Figure 5.17.

APPENDIX E

AN ERROR ANALYSIS OF THE ECHO SIMULATION OPERATIONS

Sources of error in the echo simulation fall into three categories: a) inaccurate reconstruction of the $N_e(h)$ profiles, b) incorrect specification of the geomagnetic field orientation, and c) errors in the raytrace process. These will be treated in order below.

E.1 Profile Inaccuracies

This error source is potentially the most serious, since it directly determines the ray altitude and therefore strongly influences the aspect angle. Particular care must be taken in reconstructing the F region, where the majority of refractive bending takes place at HF. However, owing to the severe spread-F condition on the Boulder vertical ionogram, a basic ambiguity exists in this layer. The effects upon the simulated echo arising from this ambiguity have been considered in Section 5.5.3, in conjunction with the echo of 1845 MST, 6 January 1972. It was determined that a marked change in the echo characteristics, notably the extinction frequency and the degree of defocusing, resulted when the raytracing was performed in F layer profiles corresponding to the extreme possibilities allowed by the frequency-spread BL ionogram traces, together with a correction for a suspected local ionization enhancement at Boulder. Errors of a similar character might arise from ambiguities in the specification of the sub-F ionospheric profile. As explained in the text, this section of the profiles often had to be reconstructed using estimated parameters and analytic model layers, since the relevant $h'(f)$ data had been obscured on the vertical ionograms by broadcast band interference. A related uncertainty originates from the essential ambiguity in the E-F valley profile, which is necessarily based upon estimated data. These two causes were studied in tandem, as explained below.

The intent of this investigation was to establish upper bounds for the errors in aspect and echo-point position arising from misspecification of the sub-F ionospheric region. Since this portion of the 1845 MST, 6 January ionosphere was constructed entirely from

estimated data, and because the ratio of f_oF to f_oE was low at this time (reducing the relative influence of the F layer), this profile was chosen as the subject for this study. Because only indicative results were sought, the necessary raytracing was done using the economical "Mark 3" program, using the unmodified Boulder profile.

A standard set of raypaths was first traced through this ionosphere along the same LH path and to the same target as employed with the aspect-position computations of Section 5.5. The ray altitude and aspect were recorded as before. To investigate the consequences of a marked alteration of the lower profile structure, the E layer and valley were eliminated completely and replaced by a monotonic D layer model (shown as the dotted line in Figure 5.6), which was fitted to the F layer by requiring continuity of $N_e(h)$ and dN_e/dh across the junction. A test series of LH raypaths was then traced through this new profile, using the same initial conditions and recording the same data as for the standard ray computations.

The echo simulation results are governed by the form of the aspect-altitude loci described by these ray data, but are not sensitive to the actual position of a given ray on a given curve. Therefore, the vital quantity is the net departure of the loci formed by the test rays from the corresponding loci described by the standard rays, and not the aspect-position discrepancy between any two counterpart members of the two ray sets. For these purposes, the separation of the corresponding loci may be characterized by their difference in aspect angle θ at representative altitudes, and by the difference in the heights at which the critical value $\theta = 88.76°$ occurs. Therefore, the aspect deviation was calculated at the altitudes at which the standard rays reached the target, using cubic natural spline (CNS) functions fitted to the test data to define these aspect-position loci; and the latitudes at which the lower-branch echoes occurred were computed using CNS interpolating functions fitted to both sets of data. These results are presented in Table E.1.

A useful criterion for interpreting these data is that the width of the lines representing the loci in Figure 5.7 is about 0.03° in θ,

and 0.3 km in h. Consequently, differences less than these shift the loci imperceptibly and thus are completely negligible. The somewhat larger discrepancies in θ (or $\Delta\theta$) variously recorded may be assessed by examining the curves of Figure 5.7 to determine whether the indicated vertical shift of the corresponding LH locus (downward for positive $\Delta\theta$, and inversely) materially alters the reconstructed echo. Since the loci are themselves nearly vertical over much of their length, the vertical displacements are generally of negligible consequence. An exception occurs at the extinction frequency, where the loci are horizontal was scaled from the inset of Figure 5.7. Multiplying this by the 0.03° maximum $\Delta\theta$ at the dip in the 17.5 and 20.0 MHz curves, the extinction frequency is raised by 0.04 MHz, a clearly negligible amount.

The altitudes of the echo points are likewise insignificantly changed. These changes (Δh) are explicitly listed for the lower-branch echoes in Table E.1; the upper-branch discrepancies were not computed but must be even less, since the component rays have a greater initial elevation and therefore suffer less refraction in the lower ionosphere.

Similar results, not presented, were obtained with test rays traced through the modified BL ionosphere, with its lower structure altered as above. Therefore, since the synthetic echo is not significantly altered by the gross restructuring of the lower ionosphere, the effects of the smaller errors anticipated in the process of reconstructing the E layer-valley profile segments are entirely negligible.

E.2 Incorrect Orientation of the Geomagnetically-Aligned Reflectors

Here again, the alterations of the simulated echo characteristics are of prime interest. Hence, invoking the reasoning of Section E.1, a suitable measure of the effects of reflector orientation changes is the displacement from echo aspect of the rays comprising the synthetic echo, and it was therefore undertaken to study the displacements from echo aspect of the rays comprising the synthetic echo, and it was therefore undertaken to study the displacements accompanying likely variations in I and D. Since the effects of profile

TABLE E.1 The height and aspect at which the standard rays encountered the target. The last column in each panel lists the difference $\Delta\theta = \theta_S - \theta_T$ for the test rays arriving at the given altitude. Δh is the difference in the heights at which the lower-branch echo occurs for the two ray sets.

f = 12.5 MHz			
β_o	h	θ	$\Delta\theta$
0°	159.3 km	91.04°	-0.28
1	184.1	91.60	0.06
2	206.0	88.65	0.09
3	216.5	81.42	0.31
Δh = 0.25 km			

f = 15.0 MHz			
β_o	h	θ	$\Delta\theta$
0°	160.1 km	91.18°	-0.18
1	185.2	91.81	0.04
2	208.1	89.77	0.06
3	223.0	85.40	0.03
4	231.7	83.06	0.05
5	238.7	82.46	0.09
6	247.0	82.89	0.07
7	258.2	84.00	0.07
8	273.3	86.62	0.04
9	295.5	90.61	0.03
Δh = 0.14 km			

f = 17.5 MHz			
β_o	h	θ	$\Delta\theta$
0°	160.6 km	91.28°	-0.13
1	186.0	91.96	0.03
2	209.5	90.55	0.05
3	227.2	87.90	0.03
4	241.5	87.26	0.03
5	255.7	87.71	0.02
6	271.3	89.00	0.03
7	290.2	91.30	0.02
8	313.1	93.93	0.03
Δh = 0.02 km			

f = 20.0 MHz			
β_o	h	θ	$\Delta\theta$
0°	161.0 km	91.31°	-0.10
1	186.4	92.06	0.03
2	210.5	91.12	0.02
3	230.2	89.49	0.01
4	248.0	89.53	0.01
5	265.5	90.30	0.01
6	285.1	91.99	0.01
7	307.4	94.06	0.01
Δh not defined			

and raytracing inaccuracies are treated elsewhere, the positions and attitudes of the rays at the target may be taken as the given quantities in this investigation.

A discrepancy of 0.1° between the measured ground-level declination and the Jensen and Cain [1962] model value was noted in the text. This may be considered a representative error for the model but, for illustration, an uncertainty range of ± 0.3° was assumed for both the dip and declination. The standard values of I and D were taken to be 68.09° and 12.83°, respectively, which correspond to the reflector orientations employed in the text. The range of the aspect angle θ was then computed for both the LH and the LB rays arriving at the target in their respective great-circle planes, at the common echo ray elevation of 9.53°.

The results of these computations are presented in Figure E.1, where θ is plotted as a function of I, parametric at 0.1° increments in D. Following the usual procedure, the aspect plotted for the LB rays is the supplement of the value computed for the rays arriving from this station. Each scale is labeled twice: first in absolute units, and then according to the deviation from the standard values θ = 88.76°, I = 68.09°, D = 12.83°. The variances of the parameter D are re-labeled as deviations in α, the geomagnetic azimuth of the ray. Since $\gamma = \alpha - D$, where γ is the geographic ray azimuth, those curves then also indicate the effects of azimuth errors in the ray direction.

A deviation from the standard I and D values occurs because of the variation of I and D with altitude. The aspect-altitude diagrams show that the specular echoes and near-echoes occur between h = 150 and 300 km, and Figure 5.5 indicates that I and D vary between 68.11° and 68.08°, and 12.71° and 13.01°, respectively, within this interval. This deviation is indicated by the parallelogram boxes near the center of Figure E.1, with the solid outline belonging to the LH curve group, and the broken line to the LB set. The actual altitude trend of I and D is shown by the dotted line within each box (with the dots marking off 10 km height intervals), and spans a variation at 0.095° in θ. Invoking the arguments of the previous section concerning

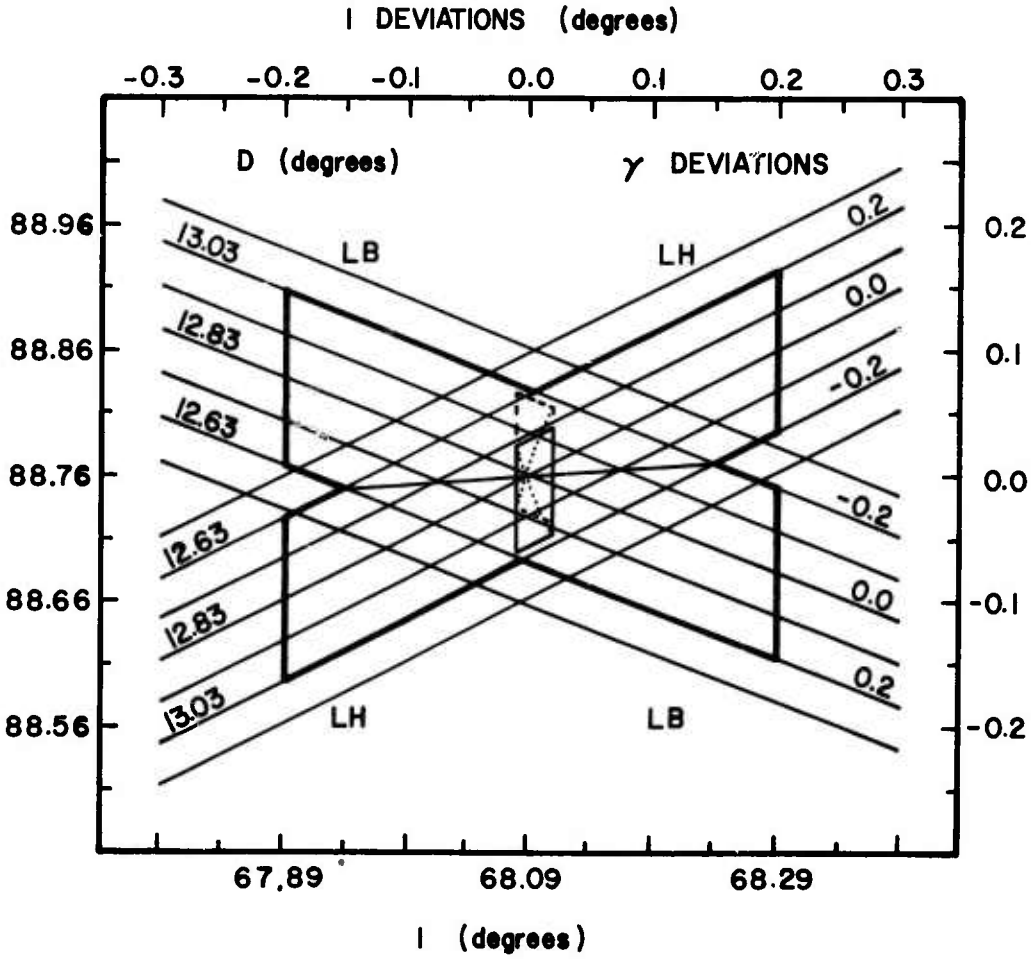

Fig. E.1 The deviations in the aspect angle θ due to variations in I, D, and γ, in the neighborhood of $\theta = \theta_e = 88.76°$.

the resultant vertical displacement of the aspect-altitude loci, this discrepancy is negligible at the lower frequencies, where the loci pass steeply through critical aspect. Its effect almost completely vanishes at the extinction frequency, since this occurs in all cases only 10 km below the h = 250 km level at which the standard I and D were computed. Consequently, the neglect of this altitude variation, done to simplify the echo-detection process, is justified.

There remains the possibility that the Jensen and Cain model may not accurately represent the actual geomagnetic field orientation at the 250 km altitude. The 0.1° discrepancy in ground-level declination

has been cited, and it is reasonable to set a working upper error bound of twice this amount. The region defined by deviations of ± 0.2° in I and D has therefore been demarcated by heavy lines in Figure E.1. A maximum variation of 0.15° (absolute value) in θ occurs in the extreme corners of this region, for both the LH and LB rays. This discrepancy is not serious; the lower-frequency echo crossings on the aspect-altitude diagrams are essentially unaffected by this vertical shift of the loci, while the extinction frequencies are changed by at most 0.2 MHz. This latter shift, although noticeable, is not great enough to alter the conclusions drawn from the simulation results.

It is interesting to note that certain combinations of I and D variances result in no aspect error at all. Such self-cancelling deviations occur along the (not shown) horizontal line representing $\theta_e = 88.76°$. It is likewise useful to point out that echoes originate from the rays of 9.53° elevation at a nearly invariant echo aspect. This aspect is depicted by the approximately horizontal line passing through the center of the diagram; it varies only 0.02° within the demarcated zone.

Results similar to the foregoing were obtained at other geographic locations bracketing the model disturbance used with the echo-contour charts of Figure 5.17. It may thus be concluded that the effects of the probable errors in specifying the reflector column orientation, and of the neglect of the altitude variation of this parameter, are inconsequential in this simulation.

E.3 Inaccuracies in the Raytracing Computations

The accuracy of a raytracing procedure may be checked by tracing a set of raypaths through standard ionospheric models for which exact analytic raypath solutions exist, and comparing the raytrace results with the exact data. Such tests of the Jones program have been conducted by Lemanski [1968] and by the author; its performance was found to be excellent in both cases. Likewise, the simpler "Mark 3" raytrace program used to generate the echo contours and the raytrace data for Section E.1 has been determined to be quite accurate [Croft, 1969].

On the other hand, the standard profiles are well-behaved mathematical functions with moderate, slowly-varying gradients, while the profiles used in this simulation, being derived from actual data, were not so well-mannered. The more rapid and pronounced variations in refractive index and its gradient thus encountered may degrade the accuracy of the raytracing process; consequently, while the aforementioned tests rule out systematic errors within the raytrace algorithms, they probably cannot guarantee the accuracy of individual raypath computations in the general case.

Such an accuracy impairment is manifest chiefly as a random component in the output, which arises from an accumulation of the roundoff errors incurred in the smaller and more numerous integration steps necessitated by a rapidly changing refracting medium. A useful test is therefore to examine the raypath data for self-consistency and for a smooth variation accompanying a regular change in the input data. In this particular case, this requires that the aspect-position loci and the echo contours derived from the raytrace data should consist of smooth curves free of unaccountable corners or undulations, and all of the data points should lie spaced at uniform or progressively changing intervals along the curves.

This is, in fact, what is observed. All of the plots based upon the raytrace data fit these criteria. Moreover, the focusing curves presented in Figures 5.8, 5.11, and 5.14, which were derived through a numerical differentiation of the raytrace data, are themselves very regular. Therefore, any errors are beyond the resolution of the methods employed to analyze the data, and a high degree of confidence in the raytrace results is justified.

REFERENCES

Albrecht, H. J., Analysis of ionospheric paths in long-range propagation, Ind. J. Meteor. Geophys., 11, 57, 1960.

Au, W. W. L., and G. L. Hower, Multi-station observations of long-range backscatter from field-aligned irregularities in the F-layer, J. Atmosph. Terr. Phys., 32, 1577, 1970.

Bailey, D. K., The effect of echo on the operation of high-frequency communication circuits, IRE Trans. Ant. Prop., AP-6, 325, 1958.

Banks, P. M., Measurements of antipodal high-frequency radio signals, J. Geophys. Res., 70, 625, 1965.

Barker, J. I., and M. D. Grossi, Design of a satellite-to-satellite communication experiment to explore HF/VHF guided propagation in the lower ionosphere, Radio Sci., 1, (New Series), 1229, 1966.

Barker, J. I., and M. D. Grossi, Results of the OV4-1 dual satellite experiment on guided ionospheric propagation, Radio Sci., 5, 983, 1970.

Barnum, J. R., Skywave polarization rotation in swept-frequency sea backscatter, Radio Sci., 8, 411, 1973.

Basu, S., R. L. Vesprini, and J. Aarons, F-layer irregularities as determined by backscatter studies at 19 MHz over half of a solar cycle, Radio Sci., 9, 355, 1974.

Bates, H. F., The height of F-layer irregularities in the Arctic ionosphere, J. Geophys. Res., 64, 1257, 1959.

Bates, H. F., Direct HF backscatter from the F region, J. Geophys. Res., 65, 1993, 1960.

Bates, H. F., The slant E_s echo--A high-frequency auroral echo, J. Geophys. Res., 66, 447, 1961.

Bates, H. F., Some effects of dense E_s clouds on high-latitude HF backscatter observations, J. Geophys. Res., 70, 5895, 1965.

Bates, H. F., The aspect sensitivity of spread-F irregularities, J. Atmosph. Terr. Phys., 33, 111, 1971.

Bates, H. F. and P. R. Albee, Aspect sensitivity of HF auroral echoes, J. Geophys. Res., 74, 1164, 1969.

Bates, H. F. and P. R. Albee, Aspect sensitivity of F-layer HF backscatter echoes, J. Geophys. Res., 75, 165, 1970.

Booker, H. G., A theory of scattering by nonisotropic irregularities with application to radar reflections from the aurora, J. Atmosph. Terr. Phys., 8, 204, 1956.

Booker, H. G., C. W. Gartlein, and B. Nichols, Interpretations of radio reflections from the aurora, J. Geophys. Res., 60, 1, 1955.

Born, M., and E. Wolf, Principles of Optics, Pergamon, New York, 1970.

Bremmer, H., Terrestrial Radio Waves, Elsevier, New York, 1949.

Bubenik, D. M., Some results of one year of continuous round-the-world HF soundings over a transpolar path, paper presented at the fall meeting of URSI, Los Angeles, September 1971.

Bubenik, D. M., A. C. Fraser-Smith, L. E. Sweeney, Jr., and O. G. Villard, Jr., Observations of fine structure in high-frequency radio signals propagated around the world, J. Geophys. Res., 76, 1088, 1971.

Budden, K. G., Radio Waves in the Ionosphere, Cambridge University Press, London, 1966.

Budden, K. G., and H. G. Martin, The ionosphere as a whispering gallery, Proc. Royal Society, A265, 554, 1962.

Calvert, W., and R. Cohen, The interpretation and synthesis of certain spread-F configurations appearing on equatorial ionograms, J. Geophys. Res., 66, 3125, 1961.

Carrara, N., M. T. de Giorgio, and P. F. Pellegrini, Guided propagation of HF radio waves in the ionosphere, Space Sci. Rev., 11, 555, 1970.

Chan, K. L., L. Colin, and J. O. Thomas, Electron densities and scale heights in the topside ionosphere: Alouette I observations over the American continents, Vol. 1, NASA SP 3027; Vol. 2, NASA SP 3032; Vol. 3, NASA SP 3033, 1966.

Chang, H. T., The waveguide mode theory of whispering-gallery propagation in the F region of the ionosphere, Radio Sci., 6, 475, 1971a.

Chang, H. T., Whispering-gallery propagation in the E region of the ionosphere at HF and VHF, Radio Sci., 6, 465, 1971b.

Chapman, S., The geometry of radio echoes from aurorae, J. Atmosph. Terr. Phys., 3, 1, 1952.

Collins, C., and P. A. Forsyth, A bistatic radio investigation of auroral ionization, J. Atmosph. Terr. Phys., 13, 315, 1959.

Croft, T. A., Interpreting the structure of oblique ionograms, Rept. SU-SEL-66-010, Stanford Electronics Laboratories, Stanford, Calif., 1966.

Croft, T. A., HF radio focusing caused by the electron distribution between ionospheric layers, J. Geophys. Res., 72, 2343, 1967a.

Croft, T. A., Computation of HF ground backscatter amplitude, Radio Sci., 2 (New Series), 739, 1967b.

Croft, T. A., Methods and applications of computer raytracing, Rept. SU-SEL-69-007, Stanford Electronics Laboratories, Stanford, Calif., 1969.

Danilin, V. A., Ionospheric waveguide ducts for long-range radio communications below the maximum of the F_2 layer, Kosmicheskiye Issledovania, 5, 231, 1967 (English Translation: AFSC-FTD document FTD-HT-23-483-68, (AD 683 125), July 1968).

Davies, K., Ionospheric Radio Propagation, NBS Monograph 80, U.S. Government Printing Office, Washington, D.C., 1965.

Davies, K., Ionospheric Radio Waves, Blaisdell, Waltham, Mass., 1969.

Davies, K., and A. K. Saha, Study of the valley problem with a ray tracing program, in Electron Density Profiles, edited by B. Maehlum, p. 162, Pergamon, New York, 1962.

Dearden, E. W., The geometry of radio reflections from field-aligned ionization irregularities in the ionosphere, J. Atmosph. Terr. Phys., 24, 375, 1962.

Dearden, E. W., Long range backscatter from F-region irregularities, J. Atmosph. Terr. Phys., 31, 959, 1969a.

Dearden, E. W., Propagation ducts due to horizontal gradients leading to echoes from magnetic field-aligned F-region irregularities, J. Atmosph. Terr. Phys., 31, 1147, 1969b.

Dyce, R. B., Auroral echoes observed north of the auroral zone on 51.9 Mc/sec., J. Geophys. Res., 60, 317, 1955.

Eckersley, T. L., Short-wave wireless telegraphy, J. IEE (London), 65, 600, 1927.

Farley, D. T., B. B. Balsley, R. F. Woodman, and J. P. McClure, Equatorial spread F: implications of VHF radar observations, J. Geophys. Res., 75, 7199, 1970.

Farley, D. T., Irregularities in the equatorial ionosphere: The Berkner Symposium, Rev. Geophys. Space Phys., 12, 285, 1974.

Fenwick, R. B., and O. G. Villard, Jr., A test of the importance of ionosphere-ionosphere reflections in long distance and around-the-world high-frequency propagation, J. Geophys. Res., 68, 5659, 1963.

Fricker, S. J., R. P. Ingalls, M. L. Stone, and S. C. Wang, UHF radar observations of aurora, J. Geophys. Res., 62, 527, 1957.

Gerson, N. C., Very long distance propagation, J. Atmos. Terr. Phys., 25, 451, 1963.

Grossi, M. D., Guided propagation of radio waves in the ionosphere, AGARD Lecture Series 41, Application of Propagation Data to VHF Satellite Communication and Navigation Systems, Lecture 11, Section 4, 1970.

Grossi, M. D., and B. M. Langworthy, Geometric optics investigation of HF and VHF guided propagation in the ionospheric whispering gallery, Radio Sci., 1 (New Series), 877, 1966.

Gurevich, A. V., Effect of nonlinearity on the generation of circum-terrestrial signals, Geomag. Aeron., 11, 810 (English Transl.), 1971.

Gurevich, A. V., and Ye. Ye. Tsedilina, Contribution to the theory of ultralong propagation of short radio waves, Geomag. Aeron., 13, 242 (English Transl.), 1973.

Hamming, R. W., Numerical Methods for Scientists and Engineers, McGraw-Hill, New York, 1973.

Haselgrove, J., Ray theory and a new method for ray tracing, London Phys. Soc., Proc. Conf. on the Physics of the Ionosphere, London, 355, 1954.

Herbert, Th., Tables of virtual heights for models of monotonic and nonmonotonic ionospheric layers, Radio Sci., 2 (New Series), 1269, 1967.

Herman, J. R., Spread F and ionospheric F-region irregularities, Rev. Geophys., 4, 255, 1966.

Hess, H. A., Investigations of high-frequency echoes, Proc. IRE, 36, 981, 1948.

Hess, H. A., Part II--investigations of high-frequency echoes, Proc. IRE, 37, 986, 1949.

Hess, H. A., Part III--investigations of high-frequency echoes, Proc. IRE, 40, 1065, 1952.

Howe, H. H., and D. E. McKinnis, Ionospheric electron-density profiles with continuous gradients and underlying ionization corrections. II. Formulation for a digital computer, Radio Sci., 2 (New Series) 1135, 1967.

Hower, G. L., and A. B. Makhijani, Further comparison of spread-F and backscatter sounder measurements, J. Geophys. Res., 74, 3723, 1969.

Humby, A. M., C. M. Minnis, and R. J. Hitchcock, Performance characteristics of high-frequency radiotelegraph circuits, Proc. IEE, 102B, 513, 1955.

Isted, G. A., Round-the-world echoes, Marconi Rev., 21, 173, 1958.

Jensen, D. C., and J. C. Cain, An interim geomagnetic field, J. Geophys. Res., 67, 3568, 1962.

Jones, R. M., A three-dimensional ray tracing computes program, ESSA Tech Rept. IER 17-ITSA 17, 1966.

Jones, R. M., Modifications to the three-dimensional ray tracing program described in IER 17-ITSA 17, ESSA Tech. Memorandum ERLTM-ITS 134, 1968.

Kelso, J. M., Ray modes in a spherically stratified ionosphere, Code 418, Office of Naval Research, Washington, D.C., 1963.

Kelso, J. M., Radio Ray Propagation in the Ionosphere, McGraw-Hill, New York, 1964.

Kelso, J. M., Ray tracing in the ionosphere, Radio Sci., 3 (New Series), 1, 1968.

King, G. A. M., Spread-F on ionograms, J. Atmosph. Terr. Phys., 32, 209, 1970.

Kraus, J. D., Antennas, McGraw-Hill, New York, 1950.

Leadabrand, R. L., and A. M. Peterson, Radio echoes from auroral ionization detected at relatively low geomagnetic latitudes, IRE Trans. Ant. Prop., AP-6, 65, 1958.

Leadabrand, R. L., and I. Yabroff, The geometry of auroral communications, IRE Trans. Antennas Prop., AP-6, 80, 1958.

Lipa, B. J., and T. A. Croft, Refractive attenuation formulas for an unstable critical ray in a circularly symmetric medium, Radio Sci., 10, 633, 1975.

Meltz, G., and F. W. Perkins, Ionospheric modification theory: past, present, and future, Radio Sci., 9, 885, 1974.

Millman, G. H., The geometry of the earth's magnetic field at ionospheric heights, J. Geophys. Res., 64, 717, 1959.

Millman, G. H., Field-aligned ionization scatter geometry, J. Geophys. Res., 74, 900, 1969.

Millman, G. H., Refraction effects on magnetic field geometry and HF propagation, J. Atmosph. Terr. Phys., 37, 751, 1975.

Mullen, J. P., R. S. Allen, and J. Aarons, Long range propagation observed on the ORBIS experiment, Planet. Space Sci., 14, 155, 1966.

Paul, A. K., Ionospheric electron density profiles with continuous gradients and underlying ionization corrections. I. The mathematical-physical problem of real-height determination from ionograms, Radio Sci., 2, (New Series), 1127, 1967.

Paul, A. K., and J. W. Wright, Some results of a new method for obtaining ionospheric N(h) profiles and their bearing on the structure of the lower F region, J. Geophys. Res., 68, 5413, 1963.

Perkins, F. W., Ionospheric irregularities, Rev. Geophys. Space Phys., 13, 884, 1975.

Peterson, A. M., O. G. Villard, Jr., R. L. Leadabrand, and P. B. Gallagher, Regularly-observable aspect-sensitive radio reflections from ionization aligned with the earth's magnetic field and located within the ionospheric layers at middle latitudes, J. Geophys. Res., 60, 497, 1955.

Piggott, W. R., and K. Rawer, URSI Handbook of Ionogram Interpretation and Reduction, Elsevier, New York, 1961.

Quäck, E., Propagation of short waves around the earth, Proc. IRE, 15, 341, 1927a.

Quäck, E., Further communication on the propagation of short waves, Proc. IRE, 15, 1065, 1927b.

Renau, J., Theory of spread F based on aspect-sensitive backscattered echoes, J. Geophys. Res., 65, 2269, 1960.

Saha, A. K., Validity of ionospheric true height analyses using the combined ordinary and extraordinary ray traces, Indian J. Pure Appl. Phys., 2, 242, 1964.

Sato, T., and K. Maeda, Scattering of electromagnetic waves by field-alined plasma columns, Radio Sci., 3 (New Series), 351, 1968.

Stathacopoulos, A. D., and G. H. Barry, Geometric considerations in the design of communications circuits using field-aligned ionospheric scatter, Radio Sci., 9, 1021, 1974.

Stein, S., The role of ionospheric-layer tilts in long-range high-frequency radio propagation, J. Geophys. Res., 63, 217, 1958.

Titheridge, J. E., A new method for the analysis of h'(f) records, J. Atmosph. Terr. Phys., 21, 1, 1961.

Tushentsova, I. A., D. I. Fischuk, and E. E. Tzedilina, The maps of global distribution of some ionospheric wave channel parameters, USSR Academy of Sciences (ISMIRAN), Preprint No. 5, Moscow, 1974.

Unwin, R. S., The importance of refraction in the troposphere and ionosphere in determining the aspect sensitivity and height of the radio aurora, J. Geophys. Res., 71, 3677, 1966.

USGS, Map: Milton Reservoir Quadrangle--Colorado Weld County, U.S. Geological Survey, Washington, D.C., 1971.

Utlaut, W. F., and E. J. Violette, A summary of vertical incidence radio observations of ionospheric modification, Radio Sci., 9, 895, 1974.

Vershinin, Ye. F., Allowance for refraction in the interpretation of radio reflections from auroras, Geomag. Aeron., 2, 243, (English Transl.), 1962.

Villard, O. G., Jr., S. Stein, and K. C. Yeh, Studies of transequatorial ionospheric propagation by the scatter-sounding method, J. Geophys. Res., 62, 399, 1957.

Wait, J. R., Electromagnetic Radiation from Cylindrical Structures, Pergamon, New York, 1958.

Von Schmidt, O., Neue erkaerung des kurzwellenumlaufes um die erde, Zeit. fur Tech. Phys., 17, 443, 1936.

Wait, J. R., Excitation of modes at very low frequency in the earth-ionosphere wave guide, J. Geophys. Res., 67, 3823, 1962.

Wait, J. R., The whispering gallery nature of the earth-ionosphere wave guide at VLF, IEEE Trans. Ant. Prop., AP-15, 580, 1967.

Wakai, N., Quiet and disturbed structure and variations of the nighttime E region, J. Geophys. Res., 72, 4507, 1967.

Washburn, T. W., Discrete echoes in ionospherically-propagated ground backscatter, Ph.D. Thesis, Stanford University, 1971.

Watkins, C. D., Radar measurements of the magnetic dip in the E-region, J. Atmosph. Terr. Phys., 30, 247, 1970.

Weaver, P. F., Backscatter echoes from field-aligned irregularities in the F region, J. Geophys. Res., 70, 5425, 1965.

Wong, M. S., Ray tracing study of HF ducting propagation with satellites, Radio Sci., 1 (New Series), 1214, 1966.

Woyk, E. (E. Chvojkova), The refraction of radio waves by a spherical ionized layer, J. Atmosph. Terr. Phys., 16, 124, 1959.

Wright, J. W., Ionospheric electron-density profiles with continuous gradients and underlying ionization corrections. III. Practical procedures and some instructive examples, Radio Sci., 2 (New Series), 1159, 1967.

Wright, J. W., and G. H. Smith, Review of current methods for obtaining electron density profiles from ionograms, Radio Sci., 2 (New Series), 1159, 1967.

Yeh, K. C., and O. G. Villard, Jr., Fading and attenuation of high-frequency radio waves propagated over long paths crossing the auroral, temperate, and equatorial zones, J. Atmosph. Terr. Phys., 17, 255, 1960.